

**Doctoral Dissertation**

**Quantum sensing and nanoscale imaging  
using scanning magnetometry with  
Nitrogen-Vacancy centers in diamond**

**Myeongwon Lee**

**Department of Physics**

**Graduate School**

**Korea University**

**August 2023**



Quantum sensing and nanoscale imaging  
using scanning magnetometry with  
Nitrogen-Vacancy centers in diamond

by

Myeongwon Lee

**REDACTED**

under the supervision of Professor Donghun Lee

A dissertation submitted in partial fulfillment of  
the requirements for the degree of  
Doctor of Philosophy in Physics

Department of Physics

Graduate School

Korea University

April 2023



The dissertation of Myeongwon Lee has been approved by the dissertation committee in partial fulfillment of the requirements for the degree of  
Doctor of Philosophy in Physics

May 2023

**REDACTED**

Committee Chair : Sanghoon Lee

**REDACTED**

Committee Member: Donghun Lee

**REDACTED**

Committee Member: Se-Jong Kahng

**REDACTED**

Committee Member: Taeyoung Choi

**REDACTED**

Committee Member: Chulki Kim



# **Quantum sensing and nanoscale imaging using scanning magnetometry with Nitrogen-Vacancy centers in diamond**

by Myeongwon Lee

Department of Physics

under the supervision of Professor Donghun Lee

## **Abstract**

Magnetic field measurement and imaging is a crucial technology used in various fields, such as physics, material science, geology, and medicine. However, current methods face limitations, with either poor magnetic field sensitivity or low spatial resolution. For instance, the superconducting quantum interference device (SQUID) method provides excellent magnetic field sensitivity ( $\sim$  pT) but has low spatial resolution ( $<$   $\mu$ m). In contrast, magnetic force microscopy (MFM) has better spatial resolution ( $\sim$  10 nm) but low magnetic field sensitivity ( $<$  mT). These methods also require cryogenic environments or have limited quantitative measurements. To address these limitations, a new approach has been proposed that combines a scanning probe microscope with a measurement method using nitrogen-vacancy (NV) centers. This approach offers the potential for high spatial resolution ( $\sim$  10 nm) and excellent magnetic field sensitivity ( $\sim$  nT).

Here, this dissertation presents an overview of NV centers and describes the measurement principles and results. In addition, the experimental setup, which combines confocal microscopy for single NV center measurement and scanning probe microscopy for imaging the magnetic field using NV, and the measurement techniques are explained. At first, a magnetic field near a nanowire was measured using the confocal microscopy setup. The results of the imaging and characterization of the magnetic field generated around a magnetic nanowire are analyzed with micro magnet simulation. In the second case, scanning imaging techniques were used to visualize the flow of current in graphene without performing transport experiments. The magnetic field map was imaged above the sample and the current distribution

was reconstructed from the magnetic field map and compared with the 2D current simulation. At third, the evolution of magnetic domains in permalloy was examined under external magnetic fields. The magnetic images driven in static and dynamic magnetic fields are imaged by static field and Rabi frequency measurements and compared with static and dynamic magnetic simulation.

The main results have demonstrated imaging magnetic fields on devices with current flow and on magnetic materials using a scanning NV magnetometer. The distribution of current flow in devices and the response of magnetic domains to external magnetic fields have been determined using non-destructive magnetic field imaging. This research on magnetic field measurement and imaging may serve the potential for spintronic device applications in addition to fundamental condensed matter physics research.

**Keywords:** Nitrogen-Vacancy centers, Quantum sensing, Magnetic imaging, and Scanning magnetometer

# 다이아몬드 질소-빈자리 결함을 이용한 양자 센싱 및 주사탐침현미경 활용

이명원

물리학과

지도교수: 이동헌

## 국문초록

높은 공간 분해능과 높은 자기장 민감도를 가지는 자기장 측정 및 이미징 방법은 물리학, 재료 과학, 지질학 및 의학 등 다양한 분야에서 중요하다. 그러나 현재 방법은 자기장 감도가 낮거나 공간 해상도가 낮은 한계를 가지고 있다. 예를 들어 초전도 양자 간섭장치(SQUID) 방법은 자기장 감도가 높지만 공간 해상도가 낮은 ( $< \mu\text{m}$ ) 반면, 자기력 현미경(MFM)은 공간 해상도가 높지만 자기장 감도가 낮다 ( $< \text{mT}$ ). 또한, 이 방법들은 극저온 환경이 필요하거나 정량적인 측정이 제한적이다. 이러한 한계를 극복하기 위해, 주사탐침현미경과 다이아몬드 질소-빈자리 결함 중심(Diamond NV center, NV 센터)을 이용한 자기장 측정 방법을 결합한 새로운 이미징 방식이 제안되었다. 이 방법은 높은 공간 분해능( $\sim 10 \text{ nm}$ )과 높은 자기장 민감도( $\sim \text{nT}$ )를 제공할 수 있는 잠재력을 가지고 있다.

이 논문에서 저자는 NV 센터의 기본적인 구조를 소개하고, 이 양자 상태를 이용한 측정 원리와 결과를 설명한다. 또한, 단일 NV 센터 측정을 위한 공초점 현미경과 자기장 이미징을 위한 주사탐침현미경 방법이 결합된 장비의 구성과 측정 기술이 설명된다. 먼저, 강자성 나노와이어 근처의 자기장이 공초점 현미경을 이용해 측정되었다. 나노 와이어 주변에서 생성되는 자기장의 이미지와 특성은 마이크로 자성 전산모사와 비교되어 분석되었다. 그 다음으로, 수송 실험을 수행하지 않고도 그래핀 내 전류의 흐름을 시각화하기 위해 기존 NV 센터 측정과 주사탐침현미경이 결합해 측정되었다. 샘플 표면 위에서 자기장 지도가 이미지 되고, 이 이미지가 매핑되어 전류 분포가 재구성되었다. 이 전류 분포는 2D 전류 전산모사와 비교되었다. 마지막으로, 외부 자기장에서 변화하는 퍼멀로이 필름의 자기구역이 측정되었다. 정적 및 동적 자기장의 영향을 받는 상황에서 자기구역은 변화한다. 자기구역의 변화가 만들어 낸 자기장 이미지를 정적 및 동적 라비 진동 측정을 통해 확인하고, 자기장 상황에서의 전산모사와 비교 분석되었다.

본 연구에서는 주사탐침현미경과 결합한 NV 자력계를 사용하여 전류 흐름이 있는 소자와 자성 물질에서 자기장을 이미징한 결과를 보였다. 비침습적인 자기장 이미징을 통해 소자 내부 전류 흐름 및 자기구역의 외부 자기장에 대한 변화가 확인되었다. 이러한 자기장 측정 및 이미징 방법은 기초 응집 물질 물리학 연구뿐만 아니라 자성 소재, 스핀트로닉스 소자 응용 분야에 활용될 수 있다.

**핵심어:** 질소-빈자리 결함, 양자 센싱, 자기장 이미징, 주사탐침자력계

# Preface

This dissertation is submitted for the degree of Doctor of Philosophy in Physics at Korea University. All of the works were performed at Korea University under the supervision of professor Donghun Lee. Parts of this dissertation were published in journals and presented at conferences.

The magnetic skyrmions sample was provided by Wondong Kim and the magnetic thin film sample was provided by Byong-Guk Park as shown in Section 3.3.1. The contents of Chapter 4 were published in [Myeongwon Lee, Bumjin Jang, Jungbae Yoon, Mohan C. Mathpal, Yuhan Lee, Chulki Kim, Salvador Pane, Bradley J. Nelson and Donghun Lee, “Magnetic imaging of a single ferromagnetic nanowire using diamond atomic sensors,” *Nanotechnology* **29** 405502 (2018)]. I was responsible for the research methods, data, simulation, and manuscript. Bumjin Jang, Salvador Pane, and Bradley Nelson provided the magnetic nanowires. The contents in Chapter 5 were published in [Myeongwon Lee, Seong Jang, Woochan Jung, Yuhan Lee, Takashi Taniguchi, Kenji Watanabe, Ha-Reem Kim, Hong-Gyu Park, Gil-Ho Lee, and Donghun Lee, “Mapping current profiles of point-contacted graphene devices using single-spin scanning magnetometer,” *Applied Physics Letters* **118** 033101 (2021)]. I was in charge of the research methods, data, simulation, and manuscript. Seong Jang and Gil-Ho Lee offered the graphene point contacted devices. The content in Chapter 6 were presented in [Myeongwon Lee, Yuhan Lee, Taekhyeon Lee, Alec Jenkins, Min-Wook Han, Soogil Lee, Ha-Reem Kim, Hong-Gyu Park, Byong-Guk Park, Ania C. Bleszynski Jayich, Kab-Jin Kim, and Donghun Lee, “Imaging spin dynamics in ferromagnets using a single spin scanning magnetometer” in *APS March Meeting* (2022) Q39–013]. I was subject to the research methodology, data, simulation, and manuscript. Taekhyeon Lee, Min-Wook Han, Soogil Lee, Byong-Guk Park, and Kab-Jin Kim provided the magnetic permalloy films, and Alec Jenkins and Ania Jayich provided the diamond scanning probes.

This page intentionally left blank.

## 감사의 글

저 혼자 힘으로는 학위과정을 마무리할 수 없었을 것입니다. 그동안 도움 주신 모든 분께 작은 감사 인사를 표시하려고 합니다.

먼저, 이동현 지도교수님께 감사의 말씀을 드립니다. 박사과정 동안 저를 연구자로 성장할 수 있게 많은 도움을 주셨습니다. 연구와 실험에 대해 아는 게 없던 저에게 연구자로서 성장할 수 있게 많은 기회를 주시고, 제게 많은 인내와 신뢰를 보여주셨습니다. 다시 한번 감사드립니다.

아울러 바쁘신 와중에도 학위 심사에 참여해 주시고 많은 조언과 지도를 아끼지 않으신 심사위원님들께 감사드립니다. 이상훈 교수님의 고체물리 수업을 통해 자성 물질과 소자 분야에 관심을 갖게 되었습니다. 그리고, 디펜스 발표에 도움 주셔서 감사드립니다. 강세종 교수님께서 학위논문을 꼼꼼히 검토해 주셔서 감사드리고, 조언 덕분에 조금 더 완성도 있는 논문이 되었습니다. 최태영 교수님 항상 다이아몬드 분야에 관심을 가져 주시고 디펜스 과정 동안 격려해 주셔서 감사드립니다. 김철기 박사님 학위과정 동안 조언과 도움 주셔서 감사드립니다. 그리고, 학부 시절 교수학습개발원 자기주도창의설계 프로그램(CCP)을 통해 지도해 주시며 양자정보 분야에 흥미를 느끼게 해주신 최만수 교수님께도 감사드립니다.

실험실에서 더 좋은 연구를 위해 같이 토론해 준 연구실 멤버들에게도 감사드립니다. 광학테이블만 있던 실험실에 들어와 같이 연구한 동기 정배에게 고마움을 전합니다. 학부 연구생부터 참여해서 함께 스캐닝 NV 실험과 연구를 같이 한 유한이에게 고마웠습니다. 잠깐이지만 다이아몬드 디바이스 실험을 함께한 찬후에게도 고마웠습니다. 동권, 기환, 주경, 석민, 이수, 우경 누나에게도 감사를 포함합니다. Also, especially thanks to Alec Jenkins for sharing his know-how of scanning experiments. 그리고, 산타 바바라에서의 생활을 많이 도와주신 유창윤 박사님께도 감사함을 전합니다. 연구실 동료들과 야구를 보며 맥주 마시는 시간을 책임져 주시고, 항상 푸근한 미소로 맞아주신 영철버거 영철 아저씨께도 감사드립니다. 야구 경기 즐기는 법을 배운 소중한 시간이었습니다.

학부 생활을 함께한 이학 2반 11학번 동기들에게도 고마움을 전합니다. 학교나 학회에서 마주칠 때마다 큰 힘이 되었습니다. 학부 과정에서 CCP 프로그램을 통해 재미있게 양자역학 공부했던 수호, 하음에게 고마움을, 양자정보 경진대회에 같이 참가한 하음과 승교에게 고마움을, 그리고 IonQ 양자컴퓨팅 챌린지를 같이해서 즐거웠고 좋은 결과를 함께한 하음에게 다시 한번 고마움을 전합니다. 그리고, 양자정보 저널 클럽을 강력한 리더십으로 이끈 박승 선배에게도 감사의 인사를 남깁니다.

다이아몬드 격자 ( $3.57 \text{ \AA} \approx 10^{-10} \text{ m}$ ) 안에 갇힌 전자 스핀 단 하나에서 나오는 빛알을 실험실에서 ( $\sim 10 \text{ m}$ ) 측정할 때, 고등학교 동아리 흰구름 사이언스부터 시작해서 그보다 더 큰 태양계뿐만 ( $\sim 10 \text{ au} \approx 10^{12} \text{ m}$ ) 아니라 더 멀리 있는 은하계를 ( $\geq 10^4 \text{ ly} \approx 10^{20} \text{ m}$ ) 망원경으로 같이 탐험한 영민, 현준, 연선, 이곤에게도 고마움을 전합니다. 그리고 다 적지 못한 소중한 친구들에게도 감사함을 표합니다.

마지막으로, 가정에서 항상 무한한 사랑으로 응원해 주시고, 격려해 주시고, 기도해 주신 이재력, 배영희 부모님께 감사드립니다. 많이 표현하지는 못한 죄송한 아들이지만, 두 분의 따뜻한 응원이 없었다면 제가 지금까지 있을 수 없었을 것입니다. 감사합니다. 사랑합니다. 앞으로도 이 은혜 잊지 않겠습니다.

학부 과정 그리고 대학원 과정 동안 강의를 듣고, 연구자로서 출항하고, 다양한 실험 주제 위를 항해했던 아산이학관에 많은 추억이 남아 있습니다. 2010년 11월 28일 일요일 입학시험을 보러 학교에 처음 왔습니다. 그때 아산이학관 1층에서 처음 읽은 문구로 감사의 글을 마무리하려 합니다.



“시련은 있어도 실패는 없다.”

아산 정주영

2023년 5월 22일

안암골에서

이명원

# Contents

<b>Abstract</b>	<b>i</b>
국문초록	iii
<b>Preface</b>	<b>v</b>
<b>Contents</b>	<b>ix</b>
<b>List of Figures</b>	<b>xiii</b>
<b>List of Tables</b>	<b>xxiii</b>
<b>List of Abbreviations and Symbols</b>	<b>xxv</b>
<b>1 Introduction</b>	<b>1</b>
<b>2 Quantum Sensing with Single Spin in Diamond</b>	<b>7</b>
2.1 The Nitrogen-Vacancy center in diamond . . . . .	7
2.1.1 Electronic structures . . . . .	9
2.1.2 Optical transitions . . . . .	10
2.2 Magnetic field sensing . . . . .	19
2.2.1 Electron spin resonance with Zeeman split . . . . .	19
2.2.2 Rabi oscillation . . . . .	23
2.2.3 Ramsey measurement . . . . .	26
2.2.4 Echo measurement . . . . .	31
2.2.5 Spin-lattice relaxation measurement . . . . .	33

<b>3</b>	<b>Nanoscale Imaging Experiment Setup</b>	<b>35</b>
3.1	Confocal optics . . . . .	35
3.2	Microwave and electronics setups . . . . .	45
3.3	Scanning probe microscope . . . . .	50
3.3.1	Imaging method example for various magnetic samples . . . . .	61
3.4	Experiment in cryostat . . . . .	65
<b>4</b>	<b>Magnetic Nanowire</b>	<b>71</b>
4.1	Ferromagnetic nanowires and diamond NV centers . . . . .	74
4.2	Experimental setup and ODMR measurement . . . . .	74
4.3	Magnetic field simulation . . . . .	75
4.4	Magnetic field imaging in confocal optics . . . . .	76
4.5	Ramsey measurement applications . . . . .	79
4.6	Conclusions . . . . .	82
<b>5</b>	<b>Point-Contacted Graphene Devices</b>	<b>83</b>
5.1	Point contacted graphene . . . . .	84
5.2	Magnetic imaging using scanning NV microscope . . . . .	87
5.3	Current profile reconstruction . . . . .	90
5.4	Conclusions . . . . .	96
<b>6</b>	<b>Dynamics in Permalloy</b>	<b>97</b>
6.1	Experimental details . . . . .	98
6.2	Static magnetic field imaging . . . . .	100
6.3	Domain driven by external field . . . . .	102
6.4	Rabi frequency calculation . . . . .	105
6.5	Driven imaging in external static field . . . . .	107
6.6	Conclusions . . . . .	108
<b>7</b>	<b>Conclusions</b>	<b>109</b>
	<b>Bibliography</b>	<b>111</b>

<b>Appendix A Spin Operator Calculation</b>	<b>129</b>
A.1 Spin operator definitions . . . . .	129
A.2 Rotating frame calculation . . . . .	130
<b>Appendix B Magnetic Field Decomposition and Current Reconstruction</b>	<b>133</b>
B.1 Magnetic field decomposition . . . . .	133
B.2 Current reconstruction . . . . .	135
<b>Index</b>	<b>137</b>
<b>Curriculum Vitae</b>	<b>139</b>

This page intentionally left blank.

# List of Figures

- 1.1 (a) The Hope diamond. Photo taken at Smithsonian National Museum of Natural History, July 2022. (b) Natural colored diamonds. Photo taken at Natural History Museum of Los Angeles County, August 2017. (c) Diamonds under a daylight lamp. (d) Diamonds under an UV light. Photo taken at American Museum of Natural History, August 2022. (e) Cut coloured diamonds (f) Natural colored diamonds. Photo take at Royal Ontario Museum, August 2022. (g)  $2 \times 2 \times 0.5 \text{ mm}^3$ (= 7.04 mg = 0.0352 carat) CVD diamonds on a 2'' wafer. (h)  $2 \times 2 \times 0.5 \text{ mm}^3$  diamond after NV center treatment glowing red shined by green laser. . . . . 2
  
- 1.2 This word frequency and word cloud show which words are used a lot in this dissertation. . . . . 6
  
- 2.1 NV center structures. (a) NV center oriented along [111] crystal direction in a diamond unit cell which size is  $3.57 \text{ \AA}$ . Carbon atoms are represented by black spheres, a nitrogen atom is represented by an orange sphere, and a vacancy is represented by a dashed lined circle. In a diamond unit cell, 18 carbons are positioned. So total 8 carbons are in the unit cell. The diamond shown in Figure 1.1(g) made by  $\approx 3.52 \times 10^{20}$  carbon atoms. (b) NV center in a different view. A symmetry axis  $z$  in NV center frame is indicated in a vertical red arrow. Optical dipoles are allowed in two perpendicular directions to the symmetry axis. . . . . 8
  
- 2.2 (a) Electronics energy level in the band gap of a diamond. There are energy states of several charge states of NV centers and ionized nitrogen. (b) Charge state readout via 594 nm yellow laser. . . . . 9

2.3	NV center energy level focused its photonic state. (a) Optical transition levels. In spin triplet, Green arrows refer excitation light such as 532 nm laser, and red arrows refer emitted photons in phonon side bands. A black arrow refer the zero phonon line, and dashed black arrows refer phonon decay. Intersystem crossing (ISC) between spin triplet and singlet state are referred in dashed dark red arrows. In spin singlet, Solid dark red arrow refer 1042 nm transition in infra-red (IR) wavelength. (b) $g^{(2)}(\tau)$ correlation measurement for single photon and fitted decay rate 5.2(32) ns. (c) Photoluminescence spectrum on wavelength. . . . .	11
2.4	Spin readout time analysis. (a) After state preparation, Green laser was used for optical pumping and synchronized readout time window with vary start time from excitation. Two pulses on readout window show start and end timing of measurement. (b) Photoluminescence unit of counts rate in kilocounts per seconds (kcps). (c) Accumulated signal from two state and its difference. (d) The contrast is calculated signal accumulation difference divided by signal accumulation of $m_s = 0$ . (e, f) Photon statistics with 5000 and 50 000 reps. . . . .	14
2.5	Depopulation time measurement. (a) Pulse sequence for depopulation measurement. “ $\pi$ ” means pi pulse. (b) Result of depopulation time for time. . . .	15
2.6	Laser power and initialization and photon counts. (a) Normalized photoluminescence result from time trace when initialization with different pumping laser powers. (b) Initialization time for different powers. (c) Photoluminescence on different laser powers. . . . .	17
2.7	Optically detected magnetic resonance. (a) CW-ESR measurement pulse scheme. Optical pumping, microwave driving and photon counting are operated in same time when the microwave frequency is varying. (b) Photoluminescence of ESR spectrum as a function of microwave frequency. . . . .	18
2.8	ESR spectrum on varying magnetic field. (a) ESR spectrum on magnetic field. (b) ESR spectrum with varying magnetic field. Darker V-shape shows Zeeman split. (c) Comparison ESR result with different magnetic field. (d) Magnetic field sensing using PL change. . . . .	21
2.9	Contrast and linewidth are depending on laser and microwave power. (a) Contrast vs. Laser power. (b) Contrast vs. Microwave power. (b) Linewidth vs. Microwave power. . . . .	23

2.10	(a) Rabi oscillation pulse scheme. Every pulse is synchronized. The microwave pulse is controlled by a switch, and the measurement is performed by varying the duration of the pulse. As the duration of the pulse varies, so do the relative positions of the laser and photon count triggers. (b) Rabi oscillation measurement result. The spin state is readable via photoluminescence. It begins in $ m_s = 0\rangle$ and changes to $ m_s = 1\rangle$ after $\sim 200$ ns. If we use a $\sim 100$ ns microwave pulse, we can achieve superposition of spin states. . . .	25
2.11	Ground state energy level and hyper fine interaction of NV centers with $^{14}\text{N}$ and $^{15}\text{N}$ . Ground state crystal field split is $D_0 = 2.87$ GHz in room temperature. . . . .	26
2.12	Ramsey measurement. (a) and (b) Hyperfine structure of NV center with $^{14}\text{N}$ and $^{15}\text{N}$ . (c) Ramsey experiment pulse scheme. There are 3 valleys in (b) with $m_I = 0, \pm 1$ transitions, and 2 valleys in (c) with $m_I = \pm \frac{1}{2}$ transitions. (d) Ramsey experiment on in condition (b). . . . .	28
2.13	Qualitative graphical description of decoherence and $T_2^*$ when Ramsey measurement. . . . .	30
2.14	Hahn-Echo measurement. (a) Pulse scheme of Echo measurement. (b) Graphical representation of Echo measurement in the Bloch sphere. (c) Echo measurement example with ESEEM in $^{15}\text{N}$ . . . . .	32
2.15	$T_1$ measurement (a) Pulse scheme of $T_1$ measurement. If the $\pi$ pulse displayed in the dashed round bracket is utilized, it prepares $ 1\rangle$ state, and if it is not, it prepares $ 0\rangle$ state. (b) Result of $T_1$ measurement. There are two results prepared at $ 0\rangle$ and $ 1\rangle$ states. . . . .	33
3.1	A cartoon describing dissertation experiments. In the middle of the figure is a diamond probe with a small red arrow indicating to a single NV center. Above this, an optics that focus a green laser and tuning forks at scanning probe microscope are attached to the diamond probe. On the bottom left of the picture, there is a radio antenna that creates spin resonance. Next to it are magnets that represent spin systems, and then there is a picture of a current with electrons moving through it. On the far right, the orbital magnetic moment is displayed. In the background, a cold iceberg is visible. . . . .	36
3.2	Vibration level on an optical table and a floor. (a) Time trace of vertical velocity. (b) Frequency spectrum of velocity. (c) Time trace of vertical distance. (d) Frequency spectrum of distance. . . . .	37
3.3	Optical components of confocal microscopy. Each components details are written in Table 3.1. . . . .	38

3.4	AOM delay measurement. (a) The pulse sequence for AOM delay measurement. (b) Photoluminescence data vs. time result of AOM delay measurement. . . . .	40
3.5	(a) Schematics of $4 - \mathcal{F}$ scanning microscope. (b) Collection from NV to the end of objective lens. (c) Optical image acquired by confocal optics. Scale bar $1 \mu\text{m}$ . . . . .	43
3.6	Electronic parts. Each components details are written in Table 3.2. . . . .	47
3.7	AOM leakage reduction (a) Tank circuit diagram. (b) The Bode plot of the tank circuit. (c) Double passed AOM optics. . . . .	48
3.8	NV Imaging methods. (a) Scanning magnetic samples using a diamond tip. (b) Magnetic sample on diamond substrate. (c) Nano-diamonds on magnetic samples. (d) Wide-field of view imaging with diamond NV ensemble. . . . .	51
3.9	NV Scanning method. (a) A fabricated diamond probe. (b) Nano-diamond attached at the end of AFM cantilever. (c) Magnetic samples attached at the end of AFM cantilever. (d) Fabricated diamond pillars and magnetic samples attached at the end of AFM cantilever. . . . .	52
3.10	Scanning probe microscope electronics. Each components details in Table 3.3. . . . .	53
3.11	Confocal microscope images of diamond scanning probes. (a,d) UCSB probe images. (b,e) QNami probe images. (c,f) QZabre probe images. Scale bars $20 \mu\text{m}$ for (a-c). Scale bars $5 \mu\text{m}$ for (d-f). . . . .	54
3.12	(a) Whole side view, and (b) Side view, and (c) Top view photo of scanning systems. Scale bars $1 \text{cm}$ for (a-c). (d) Diamond probe, sample, microwave. (e) Diamond probe and nano pilla on QZabre. Scale bars $10 \mu\text{m}$ for (d,e). . . . .	55
3.13	Schematics of tuning forks. (a) Drawing of a structure and electrodes of tuning forks. (b) Equivalent RLC circuit of tuning forks. . . . .	57
3.14	Lock-In signal. (a) Amplitude vs. frequency. (b) Amplitude vs. distance. (c) Phase vs. frequency. (d) Phase vs. distance. (e) Comparison distance . . . . .	58
3.15	PL vs. distance from surface. . . . .	59
3.16	Tuning forks amplitude measurement. (a) Optical images of single NV center at diamond probe. Scale bars $1 \mu\text{m}$ . (b) Line cut of PL image where TF ON. (c) TF Amplitude vs. lock-in input signal. . . . .	60
3.17	The spatial resolution of magnetic field imaging is determined by the distance between the tip and the sample. (a) Magnetic field values along two parallel wires at different heights. (b) Magnetic field values above two electron spins at different heights. . . . .	61

3.18	Example of ESR spectrum and magnetic field measurement scheme. (a) Drawing of ESR spectrum as a function of microwave frequency. (b) The photoluminescence $\mathcal{P}(f_0)$ with regard to variations in the magnetic field when the frequency of the microwave is set at $f_0$ . (c) The difference of PL $\mathcal{P}(f_1) - \mathcal{P}(f_2)$ with regard to variations in the magnetic field when the frequencies of the microwave are set at $f_1$ and $f_2$ . (d) The lock-in PL $\Delta\mathcal{P}(f)$ spectrum as a function of microwave frequency. In the linear central area, The $\Delta\mathcal{P}(f)$ measurements at two frequencies can be used to find the frequency where $\Delta\mathcal{P}(f) = 0$ . . . . .	62
3.19	Examples for contour image of the magnetic skyrmion sample. This sample is made with Ta(1.5)/Pt(2)/Co(0.3-1.5)/Pt(5)/Ta(2) on MgO(001) Substrate. As the external magnetic field increases from (a) to (c), the magnetic image changes from zebra-like stripes to bubbles-like patterns forming the skyrmions. Scale bars 5 $\mu\text{m}$ . . . . .	63
3.20	Various magnetic imaging of ferromagnetic film with IrMn(5). (a) Full ESR measurement image. (b) Dual microwave frequency image. (c-g) Contour image with several microwave frequency for picked magnetic field variations. Scale bars 500 nm. . . . .	64
3.21	(a) A block diagram of an optical cryostat. (b) Schematic of experiments in the cryostat chamber. The radiation shield to prevent radiation is kept at 30 K, which is the temperature of the first stage of the cryocooler, to prevent radiation heating at room temperature. The upper part of the radiation shield has a hole for optical access through which most of the radiation heat is transferred. Electronics pass through the radiation shield, which inhibits heat transfer through conduction. . . . .	68

3.22	Temperature and vacuum data were measured during the 36-hour cooling process. (a) Temperature data. Due to the presence of samples and experimental equipment, the cooling time is several hours longer. Stages 1 and 2 are the temperature of the pulsetube of the cryostat GM cryocooler. The temperature of the radiation shield is equal to the temperature of Stage 1. It is cooled to $\sim 30$ K first and maintained at that temperature. The temperature of the cold plate drops to $\sim 4$ K. The temperature of the sample drops to $\sim 8$ K. The sample is close to the upper window of the chamber and receives a lot of heat transfer $> 10$ mW through radiation from the outside, so its temperature does not drop further. (b) Pressure data. A vacuum of $< 1$ Torr is created using a rotary pump before starting cooling. During the cooling process, a high vacuum is achieved through a decrease in temperature and a cryopump.	69
4.1	(a) Schematics of magnetic field imaging of single nanowire. (b) Bar magnet and iron powders. (c) Bar magnet and compasses. Scale bars 2 cm. . . . .	72
4.2	Magnetic properties of a single Co nanowire. (a) An SEM image of a single Co nanowire. Scalebar, $2 \mu\text{m}$ . The magnetic hysteresis loop obtained from nanowire arrays (inset) confirms the soft ferromagnetic property of the Co nanowire. The saturation magnetization of the arrays, $M_s$ , is $\sim 5 \times 10^5 \text{ A m}^{-1}$ . (b) Confocal microscope image of a single Co nanowire on a diamond plate. The nanowire appears as a dark rod. The bright spots are NV centers. Scalebar, $2 \mu\text{m}$ . (c) An OOMMF simulation of the magnetic field around the wire. A magnetization value of $M = 1.4 \times 10^5 \text{ A/m}$ is used for the simulation. Field strength is indicated by color while field direction is denoted by the arrows. Scale bar, $2 \mu\text{m}$ . . . . .	77
4.3	Magnetic imaging of a single Co nanowire. (a) 92 NV centers of $[\bar{1}\bar{1}\bar{1}]$ crystal orientation are used to image magnetic stray field around the nanowire. Circles denote the NV centers and color represents $B_{\text{NV}}$ . (b) For the purpose of smooth and continuous field display, the data in (a) are reconstructed by a biharmonic spline interpolation method. For clarity, constant field contour lines are added. (c) Simulated magnetic field along the $[\bar{1}\bar{1}\bar{1}]$ direction. The results in Figure 4.2(c) are converted into the field component along the NV axis. Dipole-like patterns at the nanowire's tips are well visible both in (b) and (c). All scale bars, $2 \mu\text{m}$ . . . . .	78

- 4.4 Ramsey sequences for sensitive DC measurement. (a) There are three hyperfine resonances in the ODMR spectrum resulting from the coupling between the NV electron spin and  $^{14}\text{N}$  nuclear spin ( $I = 1$ ). Microwave pulses used in the Ramsey sequence are detuned from the resonances by  $\delta_1$ ,  $\delta_2$ , and  $\delta_3$ . (b) Obtained Ramsey signal displays beating patterns of three oscillations at the detunings. The FFT of the signal shows three peaks at the detuning of  $\delta_1$ ,  $\delta_2$ , and  $\delta_3$  (inset). The locations of these peaks will be shifted in the presence of magnetic field from the nanowire. . . . . 80
- 4.5 Comparison of the Ramsey measurement between two NV centers. (a) The Ramsey data obtained from the NV centers marked in the confocal image (b). For clarity, the plots are offset in  $y$ -axis. Due to detuning that was either too large (for  $\text{NV}_1$ ) or too small (for  $\text{NV}_2$ ), only two oscillations are observable in the measurement (see the text for further information). The fit results are written in the graph. From the fit results of  $\delta_2$ , we extract  $B_{\text{NV}}$  at each NV center:  $B_{\text{NV}} = 40(20) \mu\text{T}$  for  $\text{NV}_1$ , and  $B_{\text{NV}} = 0(30) \mu\text{T}$  for  $\text{NV}_2$ . (b) Confocal image shows locations of the two NV centers. Scale bar,  $5 \mu\text{m}$ . . . . . 81
- 5.1 Graphene point contact devices. (a) Optical image of device #1. A rectangular shape of hBN-encapsulated graphene is patterned to have two narrow channels in the middle (channel width is  $\sim 500 \text{ nm}$  and their separation is  $\sim 2 \mu\text{m}$ ). (b) Optical image of device #2. There are four point contacts at the corners of a rectangular hBN-encapsulated graphene and their relative separations are  $3 \mu\text{m}$ ,  $5 \mu\text{m}$ , and  $5.8 \mu\text{m}$ . The electrodes are electrically connected to the graphene through holes in the top-hBN. The hole diameter is  $\sim 500 \text{ nm}$ . Scale bars  $3 \mu\text{m}$ . (c) Graphene resistance vs back gate voltage. To prevent the device from significant Joule heating, we maintain the resistance below  $5 \text{ k}\Omega$  by applying  $+5 \text{ V}$  gate voltage. (d) Schematic of imaging the current profile between two point contacts. We define  $(x; y; z)$  Cartesian coordinate such that the  $z$  axis is perpendicular to the graphene surface located in the  $(x; y)$  plane and the  $x$  axis is along the direction of two PCs. The dashed lines are equipotential contours and the solid line arrows indicate the direction of current. (e) Cross-section of the device #2. . . . . 85

5.2	<p>Probing magnetic field via ESR. (a) Optically measured ESR spectroscopy of the diamond NV center. The difference in the resonance frequencies corresponds to the amount of Zeeman splitting that is proportional to the magnetic field along the NV axis. (b) ESR data measured by frequency modulated lock-in methods. (c) The resonance frequency is determined from the <math>x</math> intercept of the frequency modulated data. (d) The histogram of the magnetic field measurements shows that the minimum detectable magnetic field for 1 s measurement is <math>\sim 6.8 \mu\text{T}</math>.</p>	88
5.3	<p>Reconstruction of current density in device #1. (a) Simulated current density with the supplied current of <math>100 \mu\text{A}</math>. (b) Simulation of magnetic field along the NV axis, <math>B_{\text{NV}}</math> based on the current density in (a). (c) Measured <math>B_{\text{NV}}</math> with the scanning magnetometer described in Figure 5.1(d). The pixel size of the image is <math>50 \text{ nm}</math> and it takes <math>1 \text{ s}</math> of the measurement for each pixel. (d)–(f) From the data in (c), we obtain the magnetic images of <math>(B_x, B_y, B_z)</math>. (g)–(i) We reconstruct the current density of <math>J_x, J_y</math> and <math>\vec{J}(x, y) = (J_x, J_y)</math> with the help of the reconstruction method described in the main text. Note the color and arrows in (i) indicate the magnitude and direction of <math>\vec{J}</math>. The dotted lines in all images are guidelines of the graphene. Note that the non-zero current density in the shaded areas is an artifact from the reconstruction process. All scale bars <math>500 \text{ nm}</math>.</p>	89
5.4	<p>Flow diagram of the reconstruction process. Using Ampere’s law and Fourier transform, we first convert the real space data of <math>B_{\text{NV}}</math> into Fourier space counterparts of <math>\tilde{B}_{\text{NV}}, \tilde{B}_x, \tilde{B}_y,</math> and <math>\tilde{B}_z</math>. Using inverse Fourier transform, we obtain the real space images of <math>B_x, B_y,</math> and <math>B_z</math>. Or using Biot-Savart’s law and the model Green’s function with Hanning Window, we calculate Fourier space current density, <math>\tilde{J}_x</math> and <math>\tilde{J}_y</math>. With inverse Fourier transform, we convert these into real space values of <math>J_x</math> and <math>J_y</math>. Finally we reconstruct the current density, <math>\vec{J}(x, y) = (J_x, J_y)</math>.</p>	90
5.5	<p>Effect of the Hanning Window in the reconstructed current density profile. The Hanning Window function used in the reconstruction process contains the cut-off wavelength, <math>\lambda</math>. If it is too big (e.g. <math>\lambda = 640 \text{ nm}</math>), fine features of <math>\vec{J}</math> is not shown due to spatially averaged out. If it is too small (e.g. <math>\lambda = 40 \text{ nm}</math>), higher frequency components of wave vector <math>k</math> are not effectively filtered out. For the figures in the main text, we used a value in between i.e. <math>\lambda = 160 \text{ nm}</math>.</p>	91

5.6	Measurement with the opposite directions of current flow. (a) and (b) Measured $B_{\text{NV}}$ around a point contact in device #1 but with the reversed direction of current; from left to right in (a), and the opposite in (b). (c) and (d) Expected $B_{\text{NV}}$ images according to the current direction in (a) and (b). (e) and (f) Reconstructed current density based on the measurement in (a) and (b). The dotted lines in all images are guidelines of the graphene channel. Note that the non-zero current density in the shaded areas is an artifact from the reconstruction process. All scale bars 200 nm. . . . .	92
5.7	Magnetic field measurement on device #2. (a) Scanned image of $B_{\text{NV}}$ . The two top point contacts in the inset are used for the experiment and DC of 200 $\mu\text{A}$ is supplied from the left to the right point contact. Scale bar 500 nm. (b) The line cut profile along the dashed line in (a) shows that the measured magnetic field is inversely proportional to the distance from the point contacts. The shade indicates where the top electrodes [dotted curves in (a)] are located over the point contacts. . . . .	94
5.8	Reconstruction of current density in device #2. (a) Close-up measurement of $B_{\text{NV}}$ around the drain point contact (the right one in Figure 5.7). (b) and (c) Magnetic images of $(B_x, B_y, B_z)$ converted from the data in (a). (e)–(g) Reconstructed images of $J_x, J_y$ and $\vec{J}(x, y) = (J_x, J_y)$ . The dotted lines in all images indicate a graphene edge. Note that the non-zero current density in the shaded areas is an artifact from the reconstruction process. All scale bars 200 nm. . . . .	95
6.1	(a) Experimental Schematics. Diamond probes hosting single NV centers acquire static magnetic field and Rabi oscillation using ODMR on each position of Py. Microwave $\sim 3$ GHz is used to excite magnetic resonance in NV centers. Gold wire is used to generate the microwave. (b) Magneto optical Kerr effect microscopy images. Each color shows direction of magnetization of domains. It shows four magnetic domain around vortex. Scale bar 5 $\mu\text{m}$ . . . . .	98
6.2	(a) Magnetic simulation of permalloy square. (b) Magnetic field simulation on permalloy square. (c) Magnetic field imaging using ESR measurement. All scale bars 2 $\mu\text{m}$ . . . . .	99
6.3	(a) ESR signal is acquired photoluminescence as a function of microwave frequency. Magnetic field is measured by the frequency difference of valleys in ESR. (b) Dual frequency measurement signal is proportional to magnetic field. (c) Magnetic field imaging using dual microwave frequency imaging. All scale bars 2 $\mu\text{m}$ . . . . .	101

6.4	Magnetic domain evolution in different magnetic field. The domain of east side is parallel to external field with $-y$ direction. Size of east side domain by applying external magnetic field. (a,b,c) Domain shows with varying external magnetic field for 0.6 mT, 1.0 mT, and 2.0 mT. The position of vortex moves to right side by external field $-y$ direction. (d,e,f) Magnetic field simulation by dual-iso imaging method. (g,h,i) Scanning images. All scale bars $2 \mu\text{m}$ . . . . .	102
6.5	(a) Map of ESR contrast. (b) Rabi frequency is calculated from ESR contrast. (c) Image of Rabi frequency. (d) Data of Rabi oscillation of each point labeled in 1, 2, and 3. The frequency of oscillation is Rabi frequency. (e) Rabi frequency is calculated from the simulation of magnetization dynamics. All scale bars $2 \mu\text{m}$ . . . . .	103
6.6	(a) The normalized amplitude of oscillating magnetization modulated with frequency $\sim 3 \text{ GHz}$ for $\Delta M_x$ , (b) $\Delta M_y$ and (c) $\Delta M_z$ . (d) The sinusoidal magnetic field generated by magnetization oscillation in the first direction of perpendicular with NV centers orientation. (e) The sinusoidal magnetic field in the second direction of perpendicular with NV centers. All scale bars $2 \mu\text{m}$ .	106
6.7	(a) Static magnetic field image in bias field $B_y = -0.6 \text{ mT}$ . (b) Image of ODMR contrast. (c) Image of Rabi frequency. All scale bars $2 \mu\text{m}$ . . . . .	108

# List of Tables

- 3.1 Optical components used for confocal optics. The positions of the components are shown in Figure 3.3. . . . . 39
- 3.2 Electronics and Microwave components. This is utilized to design a microwave and measurement system as illustrated in the Figure 3.6. . . . . 46
- 3.3 Tuning forks based scanning probe microscope electronics. This is used to build the scanning probe electronics as seen in the Figure 3.10. . . . . 53

This page intentionally left blank.

# List of Abbreviations and Symbols

## Abbreviations

2D	Two-dimensional
AC	Alternating current
ADC	Analog to digital converter
AFM	Atomic force microscope
AOM	Acousto optical modulator
APD	Avalanche photodiodes
AWG	American wire gauge
CVD	Chemical vapor deposit
CW	Continuous wave
DAC	Digital to analog converter
DAQ	Data acquisition system
DC	Direct current
DD	Dynamical decoupling
DM	Dichroic mirror
ESEEM	Electron spin echo envelope modulation
ESR	Electron spin resonance
FFT	Fast Fourier transform
FM	Frequency modulation
FL	Focal length
FOV	Field of view
FSM	Fast steering mirror
FWHM	Full width at half maximum
GPIB	General purpose interface bus
hBN	hexagonal boron nitride
HV	High vacuum
IQ	In phase & Quadrature
IR	Infrared

ISC	Intersystem crossing
LASER	Light amplification by the stimulated emission of radiation
LLG	Landau-Lifshitz-Gilbert
MFD	Mode field diameter
MFM	Magnetic force microscope
MOKE	Magneto-optical Kerr effect
MW	Microwave
NA	Numerical aperture
ND	Neutral density
NISQ	Noisy intermediate-scale quantum
NV	Nitrogen-Vacancy
ODMR	Optically detected magnetic resonance
OOMMF	The Object Oriented Micro Magnetic Framework project at ITL/NIST
PC	Point contact
PCB	Printed circuit board
PCIe	Peripheral component interconnect express
PID	Proportional-Integral-Differential
PL	Phonoluminescence, unit in counts per seconds (cps). kcps( = kilo – cps = $10^3$ cps) is mainly used.
PMMA	Poly(methyl methacrylate)
PXI	PCI eXtensions for Instrumentation
Py	Permalloy, nickel–iron magnetic alloy, $\text{Ni}_{80}\text{Fe}_{20}$
RF	Radio frequency
RIE	Reactive ion etching
RLC	A resistor (R), an inductor (L), and a capacitor (C)
SEM	Scanning electron microscope
SNR	Signal to noise ratio
SPCM	Single photon counting module
SPM	Scanning probe microscopy
SQUID	Superconduction quantum interference device
TF	Tuning forks
TTL	Transistor to transistor logic
UHV	Ultra high vacuum
UV	Ultraviolet
XMCD	X-ray magnetic circular dichroism
ZFS	Zero field split, symbol $D_0$
ZPL	Zero phonon line

## Symbols

$A$	Area, unit in $\text{m}^2$
$\mathbf{A}$	Hyperfine coupling parameters $A_{\parallel}$ , $A_{\perp}$ represented in matrix, unit in Hz
$\alpha_E$	Accommodation coefficient for gas or vapor particles, dimensionless quantities
$\alpha$	Damping constant in LLG equation, dimensionless quantities
$a$	Mechanical amplitude, unit in nm
$\vec{B}$	Magnetic field, unit in $\text{T} = \text{V s}/\text{m}^2 = \text{kg}/(\text{A s}^2)$
$C$	ODMR Contrast, dimensionless quantity
$C$	Capacitance, unit in $\text{F} = \text{J A}^{-2}$
$c$	Speed of light in vacuum, $c = 299\,792\,458 \text{ m/s}$
$\vec{D}$	Electric displacement field, unit in $\text{C}/\text{m}^2 = \text{A s}/\text{m}^2$
$D_0$	Zero field split by crystal field, at room temperature, $D_0 = 2.87 \text{ GHz}$
$\mathcal{D}$	Diameter, unit in mm
$\nabla$	Vector differential operator, $\nabla = \hat{x} \frac{\partial}{\partial x} + \hat{y} \frac{\partial}{\partial y} + \hat{z} \frac{\partial}{\partial z}$ , unit in $\text{m}^{-1}$
$\Delta$	In front of a variable, change in the certain variable.
$\delta$	In front of a variable, infinitesimal change in the variable.
$\delta_i$	Detuning frequency, unit in Hz, or
$d$	Distance, unit in nm
$E$	Energy, unit in J or eV
$\vec{E}$	Electric field, unit in $\text{V}/\text{m} = \text{kg m}/(\text{A s}^3)$
$\mathcal{E}$	Young's modulus, unit in Pa
$\epsilon_0$	Permittivity in vacuum, $\epsilon_0 = 8.854\,187\,812\,8 \text{ F/m}$ , $\text{F}/\text{m} = \text{C}/(\text{V m})$
$\varepsilon$	Emissivity of thermal radiation, dimensionless quantity
$e$	Euler's number, $e = 2.718\,281 \dots$
$e$	An electron, $-1.602\,176\,634 \times 10^{-19} \text{ C}$
$\mathcal{F}$	Focal length, unit in mm
$f$	Frequency, unit in Hz
$\Gamma$	Line width or decay channel rate, unit in Hz
$\gamma_e$	Gyromagnetic ratio of electron spin, $\gamma_e = 28 \text{ MHz/mT}$
$\gamma_N$	Gyromagnetic ratio of nitrogen, $\gamma_{^{14}\text{N}} = 3.08 \text{ kHz/mT}$ and $\gamma_{^{15}\text{N}} = 4.32 \text{ kHz/mT}$
$\gamma$	Heat capacity ratio, dimensionless quantity
$g_e$	Electron g-factor, $g_e \simeq -2$ . <i>cf.</i> $g_N$
$\mathbf{g}$	Green's function matrix, $\mathbf{g}(k_x, k_y, z)$ . Same dimension with permeability $\mu_0$
$g^2(\tau)$	Correlation function
$\vec{H}$	Magnetic field strength, unit in A/m
$\hat{H}$	Hamiltonian operator, dimension in energy
$h$	Planck constant, $h = 6.626\,070\,15 \times 10^{-34} \text{ J Hz}^{-1} = 4.135\,667\,696 \times 10^{-15} \text{ eV Hz}^{-1}$
$\hbar$	Reduced Planck constant, $\hbar = \frac{h}{2\pi} = 1.054\,571\,81 \times 10^{-34} \text{ J s} = 6.582\,119\,569 \times 10^{-16} \text{ eV s}$

$h$	Height, unit in mm
$\eta_B$	Magnetic field sensitivity, unit in $\text{T}/\sqrt{\text{Hz}}$
$\vec{I}$	Nuclear spin operators, dimensionless operator in this dissertation
$I$	Intensity of photoluminescence, unit in kcps
$i$	Imaginary number, $i = \sqrt{-1}$ . In a subscript letter, it means index.
$\vec{J}$	2D Current density, unit in $\text{A}/\text{m}$
$\vec{j}$	Current density, unit in $\text{A}/\text{m}^2$
$j$	Current, unit in A
$k_B$	Boltzmann constant, $k_B = 1.380\,649 \times 10^{-23} \text{ J K}^{-1} = 8.617\,333 \times 10^{-5} \text{ eV K}^{-1}$
$k$	Spring constant, unit in $\text{N}/\text{m}$
$\vec{k}$	Fourier space vector, unit in $\text{rad m}^{-1}$
$\kappa$	Thermal conductivity, unit in $\text{W}/(\text{m K})$
$L$	inductance, unit in $\text{H} = \text{J A}^{-2}$
$\ell$	Length, unit in m
$\lambda$	Wavelength, unit in nm
$\vec{M}$	Volume magnetization, unit in $\text{A}/\text{m}$
$M$	Molar mass, Typically, unit in $\text{g}/\text{mol}$ . But, here, kg is used.
$m$	Mass, unit in kg
$m_s$	Spin quantum number, integer or half-integer, dimensionless quantity
$m_I$	Nuclear spin quantum number, integer or half-integer, dimensionless quantity
$\mu_0$	Permeability in vacuum, $\mu_0 = 4\pi \times 10^{-7} \text{ H}/\text{m}$ , $\text{H}/\text{m} = \text{N}/\text{A}^2 = \text{T m}/\text{A}$
$\mu_B$	Bohr magneton, $\mu_B = 9.274\,010\,078\,3 \times 10^{-24} \text{ J}/\text{T} = 5.788\,381\,806\,0 \times 10^{-5} \text{ eV}/\text{T}$
$N$	Number of photons, dimensionless quantity
$\hat{n}$	Unit vector, dimensionless vector
$n$	Refraction index, dimensionless quantity
$\Omega_R$	Rabi frequency, unit in rad Hz
$\Omega$	Solid angle, unit in sr
$\omega$	Angular frequency, unit in rad Hz
$P$	Power, unit in W or $\text{dBm} = 10 \log_{10}(P \text{ in W}) + 30$
$\mathcal{P}$	Normalized photoluminescence, dimensionless quantity
$p$	Pressure, unit in Torr, $1 \text{ Torr} = 133 \text{ Pa} = 133 \text{ N}/\text{m}^2$
$p$	Probability, dimensionless quantity
$\pi$	Circular constant, $\pi = 3.141\,592 \dots$
$\phi$	Azimuthal angle in spherical coordinates, unit in rad
$\varphi$	Phase, unit in rad
$Q$	Nuclear quadrupole coupling, unit in Hz
$\mathcal{Q}$	Q factor in oscillator, dimensionless quantity
$R$	Resistance, unit in $\Omega = \text{J}/(\text{s A}^2)$
$R_i$	Rotation on an axis, unit in rad

$\mathcal{R}$	Gas constant, $R = 83\,144\,598\text{ J}/(\text{mol K})$
$\mathcal{R}$	Radius, unit in mm
$\vec{r}$	Distance vector, $\vec{r} = x\hat{x} + y\hat{y} + z\hat{z}$ , $x, y, z$ in Cartesian coordinate, unit in m
$\rho$	Electric charge density, unit in $\text{C}/\text{m}^3 = \text{A s}/\text{m}^3$
$\rho$	Density matrix, dimensionless matrix
$\vec{S}$	Spin operators, dimensionless operator in this dissertation, So, $S_z  m_s\rangle = m_s  m_s\rangle$ , $[S_l, S_m] = i\epsilon_{lmn} S_k$ , $\vec{S}^2 = S(S+1)$ , where $\epsilon_{lmn}$ denotes the Levi-Civita symbol.
$s$	Optical saturation parameter, dimensionless quantity
$\sigma$	Stefan-Boltzmann constant, $\sigma = 5.670\,374\,419 \times 10^{-8}\text{ W m}^{-2}\text{ K}^{-4}$
$\sigma_i$	Pauli matrix, $\sigma_0 = \mathbb{I} = \begin{pmatrix} 1 & 0 \\ 0 & 1 \end{pmatrix}$ , $\sigma_x = \begin{pmatrix} 0 & 1 \\ 1 & 0 \end{pmatrix}$ , $\sigma_y = \begin{pmatrix} 0 & -i \\ i & 0 \end{pmatrix}$ , $\sigma_z = \begin{pmatrix} 1 & 0 \\ 0 & -1 \end{pmatrix}$
$T$	Temperature, unit in K
$T_1$	Longitudinal relaxation time or spin-lattice relaxation time, unit in s
$T_2$	Transverse relaxation time or spin coherence time, unit in s
$T_2^*$	Inhomogeneous dephasing time or free induction decay time, unit in s
$t$	Time, unit in s
$\tau$	Evolution time, unit in s
$\ell$	Thickness, unit in m
$\theta$	Polar angle in spherical coordinates, unit in rad
$\hat{U}$	Unitary operator, dimensionless operator
$V$	Voltage, unit in $\text{V} = \text{J}/\text{C} = \text{kg m}^2 \text{s}^{-3} \text{A}^{-1}$
$v$	Velocity, unit in $\mu\text{m}/\text{s}$
$ \psi\rangle$	A ket represents a wave function in bra-ket notation. <i>cf.</i> A bra $\langle\psi $ .
$\zeta$	Density, unit in $\text{kg}/\text{m}^3$

This page intentionally left blank.

# Chapter 1

## Introduction

“Seek, and ye shall find.” *Matthew 7:7* and “Seek out *Terra Incognita*”  
from Don Eigler’s talk “There’s Plenty of Room Beyond The Horizon” [1].

Diamonds are one of the most well-known gems [2], shown in Figure 1.1(a). There are multiple factors that determine the value of a diamond, but there is a representative factor known as ‘4C’ [3], which includes ‘Carat’, which indicates weight (size), ‘Clarity’, which indicates transparency, ‘Cut’, which determines how a diamond reflects light, and ‘Color’, which denotes the hue of the diamond [4]. As shown in Figure 1.1(b-f), natural diamonds appear in a variety of hues. This color is a result of atoms within the diamond crystal not being in their original position or being replaced by impurities. A color center is a defect that absorbs and emits light of a specific wavelength. Among these color centers, the Nitrogen-Vacancy (NV) centers in diamond have been studied because of their properties [5, 6]. This dissertation will discuss how the NV center in diamond is used as a magnetic field sensor and its applications [7–10].

Quantum information science is important for various reasons since it integrates quantum mechanics and information theory to facilitate the advancement of novel technologies and capabilities not only fundamental science, but also economic [11, 12] and technological growth [13]. The primary reasons for its worth are given below.

## Chapter 1. Introduction

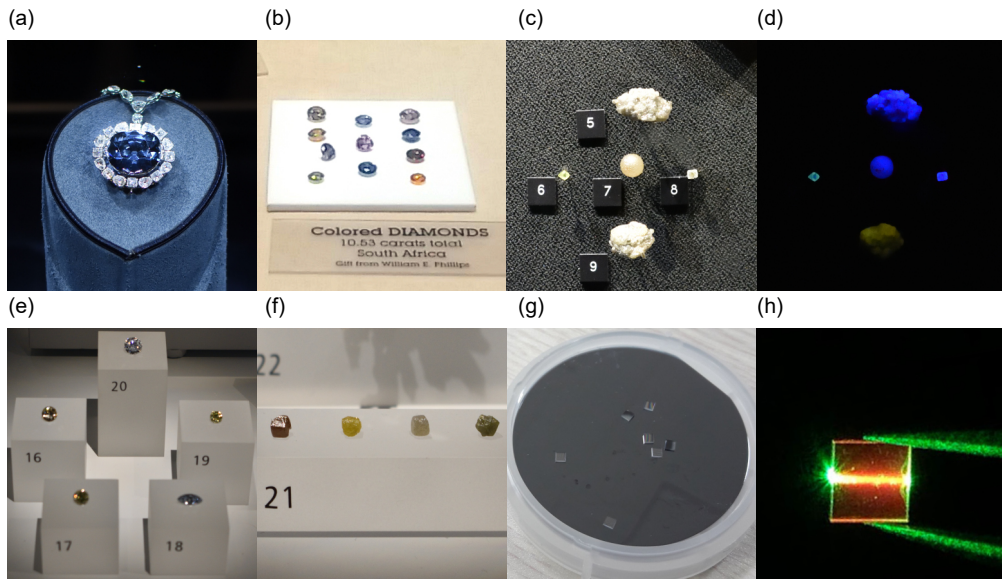


Figure 1.1: (a) The Hope diamond. Photo taken at Smithsonian National Museum of Natural History, July 2022. (b) Natural colored diamonds. Photo taken at Natural History Museum of Los Angeles County, August 2017. (c) Diamonds under a daylight lamp. (d) Diamonds under an UV light. Photo taken at American Museum of Natural History, August 2022. (e) Cut coloured diamonds (f) Natural colored diamonds. Photo take at Royal Ontario Museum, August 2022. (g)  $2 \times 2 \times 0.5 \text{ mm}^3 (= 7.04 \text{ mg} = 0.0352 \text{ carat})$  CVD diamonds on a 2'' wafer. (h)  $2 \times 2 \times 0.5 \text{ mm}^3$  diamond after NV center treatment glowing red shined by green laser.

The first is quantum computing. Quantum computing is a subfield of quantum information science that focuses on the construction of computers that process information using quantum bits (qubits) instead of classical bits [14, 15]. Quantum computers use quantum physics principles, such as superposition and entanglement, to do calculations faster than classical computers. This helps them to handle complex problems in a variety of fields, including cryptography, optimization, materials science, and drug discovery [16, 17].

The second is quantum communication. Quantum communication is the transmission and processing of quantum information using quantum systems [18]. The aim of this is to develop secure and effective communication channels that utilize the unique capabilities of quantum mechanics. Quantum communication technologies include quantum key distribution, which provides ultra-secure message encryption and decryption, and quantum teleportation [19, 20].

The third is quantum simulation. Quantum simulation is the research and development of techniques to simulate and calculate Hamiltonian using quantum systems [21]. Quantum simulators can be used to research the behavior of complex quantum systems, such as molecules and materials, that are challenging or impossible to study with classical approaches. Quantum simulations can provide insights into fundamental physics, quantum chemistry, and materials science, advancing drug discovery, and material design [22].

Quantum sensing and metrology are the last. Quantum sensing and metrology are focused on the development of high-precision measurement techniques and instruments that rely on quantum phenomena [23]. Due to quantum mechanics, quantum sensors and measurement devices can be more sensitive and accurate than the classical limit. Quantum metrology applications include atomic clocks, gravitational wave detection, and high-resolution imaging [24, 25].

In summary, quantum information science covers quantum computing, quantum communication, quantum simulation, and quantum metrology, all of which apply the principles of quantum mechanics to develop quantum technology. Quantum information science can realize the quantum advantage and overcome the classical limitations. The current situation is in a noisy intermediate-scale quantum (NISQ) era where quantum advantage is not yet realized. Quantum information science is growing rapidly due to the huge potential of this field

of study. In addition, the interest and investment of each country in quantum information science are increasing [13, 26–29].

Using the unique quantum features of these defect structures, quantum sensing with NV centers in diamonds produces highly sensitive and precise sensors, especially for magnetic fields [30]. Several properties of the NV center make it an attractive candidate for quantum sensing.

The electron spin state of the NV center is relatively stable and has long coherence times, allowing it to maintain a quantum state for a long time. Its stability is important for precise sensing and enables precise measurements even at ambient temperature [31]. The electron spin state of NV centers can be optically initialized and read, making it convenient for experimental setups [32, 33]. It is possible to initialize the spin state of the NV center by shining a laser on it, and the fluorescence emitted by the NV center is related to the spin state. The electron spin state of the NV centers is sensitive to magnetic fields [34, 35], electric fields [36], temperature [37, 38], and strain [39]. Magnetic field sensitivity enables highly precise detection and measurement of these fields. The NV center's energy levels split under an external magnetic field, a phenomenon known as the Zeeman effect. Therefore, the magnetic field can be measured quantitatively, and magnetic field sensing has been studied.

The advantages of NV centers make them suitable for utilization with a variety of devices and scanning probes. Its unique properties enable the construction of highly sensitive and precise sensors with high spatial resolution and operation from low temperature to room temperature [40–42]. Following are some of the most important advantages and characteristics of NV centers. The quantum properties and long coherence time of NV centers make it possible to detect weak magnetic fields with sensitivities as low as nT or even pT [34, 43]. This high sensitivity is advantageous for situations in which the detection of tiny magnetic field changes is required [44, 45]. The NV centers in diamonds can be placed close to the sample of interest, allowing nanometer-scale measurements with high spatial resolution [46]. Its spatial resolution is advantageous for imaging magnetic materials and spintronics devices. It is feasible to create and control NV centers at the nanoscale and fabricate them so that they may be integrated into a variety of devices and scanning probes [47–50]. Its scalability allows

for the creation of high-resolution sensors and imaging systems. NV centers show quantum states that are stable under a variety of conditions [51, 52], and diamonds are chemically stable [30, 53, 54]. Therefore, they can be utilized for precise and reliable measurements. Its stability enables the incorporation of NV centers into devices and scanning probes without degrading their sensing capabilities. This makes them valuable in a variety of fields, including materials science [55], biophysics [56], geophysics [57], and medical imaging [58, 59]. In conclusion, the advantages of NV centers, such as high sensitivity, high spatial resolution, scalability, and stability, make them suitable for scanning probes [60, 61]. These characteristics enable the fabrication of highly sensitive and precise sensors that can be utilized in a wide variety of applications that cover different fields. We will describe how to do this and its applications.

The dissertation is structured as follow:

- Chapter 2 introduces the electrical, optical, and spin structure of the basic NV center and magnetic field sensing using it. The result of measuring the basic NV structure, the method of coherently manipulating the spin, the result of this measurement, and the theoretical background will be discussed.
- Chapter 3 describes experimental details of NV center scanning microscopy. The scanning NV center microscopy is constructed with confocal microscopy, electrical systems, microwave control, and tuning forks scanning probe microscope. We will discuss why these devices are used and how they work.
- Chapter 4 presents the magnetic field imaging of a single ferromagnetic nanowire. These experimental results were performed before the construction of the scanning probe microscope. The imaging results from magnetic field sensing using confocal microscopy will be discussed.
- Chapter 5 presents the imaging result of the current profile on graphene point contacted devices. The current map reconstruction method from the magnetic field map imaged by a single spin will be discussed.



## Chapter 2

# Quantum Sensing with Single Spin in Diamond

### 2.1 The Nitrogen-Vacancy center in diamond

The NV center in diamond is a point lattice defect. It is made of two nearby carbon atoms replaced by a nitrogen atom and a vacancy [33] shown in Figure 2.1. These NV centers are like atoms trapped in the crystal lattice of a diamond. This diamond lattice provides an environment that can protect the quantum state from boiling helium temperature [62] to the temperature of the universe to boiling water temperatures to over the melting point of aluminum near 1000 K [51] and in high pressure over GPa [52], the pressure being in deeper than in the Mariana trench and core of the earth. The NV center is an electron spin qubit that can be read or initialized using an optical approach, controlled by spin resonance, and has a relatively long coherence time, therefore meeting the DiVincenzo and Loss criteria for spin qubits [63].

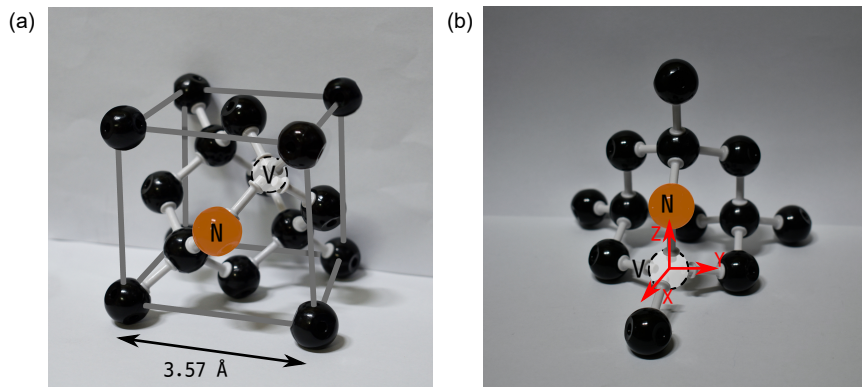


Figure 2.1: NV center structures. (a) NV center oriented along  $[111]$  crystal direction in a diamond unit cell which size is  $3.57 \text{ \AA}$ . Carbon atoms are represented by black spheres, a nitrogen atom is represented by an orange sphere, and a vacancy is represented by a dashed lined circle. In a diamond unit cell, 18 carbons are positioned. So total 8 carbons are in the unit cell. The diamond shown in Figure 1.1(g) made by  $\approx 3.52 \times 10^{20}$  carbon atoms. (b) NV center in a different view. A symmetry axis  $z$  in NV center frame is indicated in a vertical red arrow. Optical dipoles are allowed in two perpendicular directions to the symmetry axis.

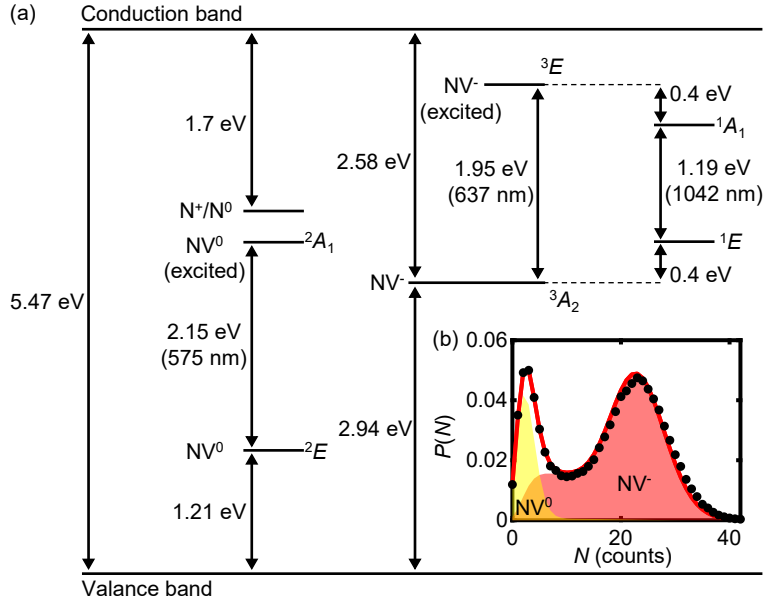


Figure 2.2: (a) Electronics energy level in the band gap of a diamond. There are energy states of several charge states of NV centers and ionized nitrogen. (b) Charge state readout via 594 nm yellow laser.

### 2.1.1 Electronic structures

The  $C_{3v}$  symmetry and the number of electrons trapped in the NV center define the electron energy structure of the NV center [64]. There are several charge states with NV center shown in Figure 2.2 [65–70]. The neutral  $NV^0$  and positively charged  $NV^+$  states do not exhibit spin-dependent photoluminescence [71]. The electrically negatively charged  $NV^-$  state exhibits a spin-dependent change in luminosity, which is why it is being studied for applications in metrology and quantum information purposes [72]. In this dissertation, the ‘NV’ center will denote the  $NV^-$  center.

This NV centers electronic energy is defined by three electrons from  $sp^3$  dangling bond of adjacent carbon atoms, two electrons from nitrogen, and one electron from the environment, such as another impurity in the crystal [70, 73]. Because of the Pauli exclusion principle, the dangling bonds can accommodate 2 electrons each, allowing a total of 8 electrons to be

fully occupied. However, in the negatively charged NV center, there are 6 electrons, which can be represented as having 2 hole defects depending on the model used [74]. It is a  $C_{3v}$  symmetric group [75] because an NV center with such an electronic structure is symmetrical for a  $120^\circ$  rotation but not when inverted. Therefore, energy states can be stated using the Mulliken notation, such as  $A_1$ ,  $A_2$ , and  $E$  [76]. According to this, the magnitude of the spin angular momentum was expressed as  $2s + 1$  on front notation. So it is expressed as  ${}^3A_2$ ,  ${}^1A_1$ ,  ${}^3E$  and  ${}^1E$ .

### 2.1.2 Optical transitions

Understanding the optical property of color centers is pretty simple. Let there be light, which energy is larger than the color center energy. The color centers absorb this light and emit photons with energy lower than that of the color centers. Now, the details of the optical transition of the NV center are discussed.

Dipole radiation oriented perpendicular to the axis of symmetry produces optical light emission in NV centers [77]. The level of optical transition is shown in detail in Figure 2.3. First, considering the spin triplet state, the NV ground state  ${}^3A_2$  and the excited state  ${}^3E$  are separated by an energy difference of 1.95 eV (637 nm, 471 THz) [70, 72]. This is called the zero-phonon line (ZPL). At low temperatures, the  ${}^3E$  state has an orbital structure, but at room temperature it is broad and difficult to distinguish [39].

The transition between the ground state and the excited state is connected to the phonon mode, which in general absorbs more energy and emits less energy [78], as represented by the green and red arrows, respectively. Therefore, the NV center has a wide absorption spectrum and may be efficiently excited with photon wavelengths of around 400 nm to 637 nm [70]. In this dissertation, a 532 nm laser is used for off-resonant excitation.

For the emitted photon, less than 4% of the photons are released at ZPL [72], and the dominant wavelength range is 650 nm to 800 nm. This wavelength band is called the phonon side band. The  $|m_s = 0\rangle$  state and the  $|m_s = \pm 1\rangle$  state are separated in a spin triplet. Quantum states are displayed using the bracket notation. It is excited while conserving spin. After excitation, it emits light with a decay rate of approximately  $\sim 10$  ns, and returns to its ground

## 2.1. The Nitrogen-Vacancy center in diamond

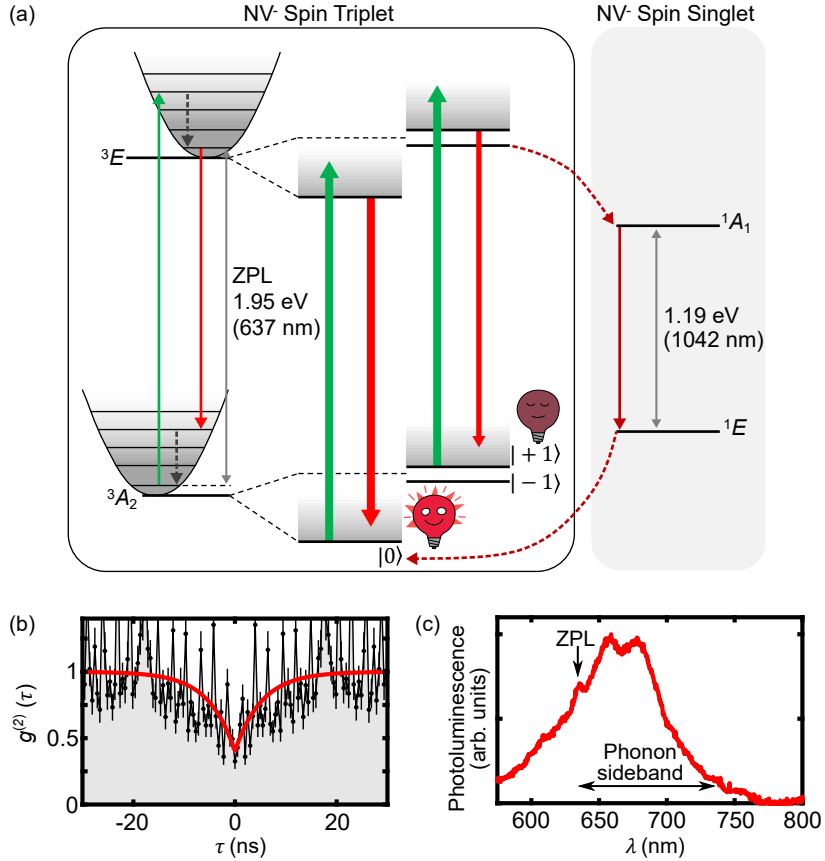


Figure 2.3: NV center energy level focused its photonic state. (a) Optical transition levels. In spin triplet, Green arrows refer excitation light such as 532 nm laser, and red arrows refer emitted photons in phonon side bands. A black arrow refer the zero phonon line, and dashed black arrows refer phonon decay. Intersystem crossing (ISC) between spin triplet and singlet state are referred in dashed dark red arrows. In spin singlet, Solid dark red arrow refer 1042 nm transition in infra-red (IR) wavelength. (b)  $g^{(2)}(\tau)$  correlation measurement for single photon and fitted decay rate 5.2(32) ns. (c) Photoluminescence spectrum on wavelength.

state [79]. However, there are spin structures  $\sim$  GHz that have a magnitude much smaller than that of the optical level  $> 10^2$  THz. In the ground state, it is as distinct as the zero field split (ZFS)  $D_0 = 2.87$  GHz [72, 75]. Depending on the spin state, the optical transition differs slightly. This spin dependence is a key component of the optical cycle of the NV center. The NV electronic structure allows for an all-optical spin polarization method and a spin-dependent photoluminescence readout mechanism, as discussed in the next section. By applying these characteristics, it will be possible for us to accomplish optically detected magnetic resonance of the ground state spin states and also single qubit gates.

### Spin initialization

The capability to initialize a quantum state is an important criterion for a good quantum system. Because of comparing with optical transition energy, thermal energy and ground state spin state energy

$$\begin{aligned}
 E_{\text{ZPL}} &= 1.95 \text{ eV} \simeq 637 \text{ nm} \simeq 471 \text{ THz} \\
 &\gg k_{\text{B}}T|_{T=300\text{K}} \sim 25.9 \text{ meV} \simeq 6.27 \text{ THz} \gg k_{\text{B}}T|_{T=4\text{K}} \sim 345 \text{ } \mu\text{eV} \simeq 83.6 \text{ GHz} \quad (2.1) \\
 &\gg D_0 = 2.87 \text{ GHz}
 \end{aligned}$$

, where  $k_{\text{B}}$  is Boltzmann constant and NV ground state energy is  $D_0 = 2.87$  GHz, at thermal equilibrium, the energy state of the NV center is electrically in the ground state. In a ground state spin structure, the probability of the NV energy states is the same regardless of the spin states in triplet. But, optical pumping can initialize the spin of the NV center in high fidelity. This method has the ability to polarize the spin with remarkable fidelity, even under ambient conditions.

The spin polarization method depends on the fact that the optical transition from the ground state to the excited state is not totally closed. Because of transverse spin-orbit interaction and the overlap of the vibrational wave function [80], the  $|m_s = \pm 1\rangle$  spin population enters an ISC about  $\sim 30\%$  of the time [81–84] and is non-radiatively transferred to a metastable singlet structure with an effective lifetime of 300 ns [79]. Through a second non-

## 2.1. The Nitrogen-Vacancy center in diamond

radiative ISC, the spin population of the singlet state converge to its ground state. As a result, the initialization of the spin state in the ground state to the  $|m_s = 0\rangle$  state will be effectively performed by a number of optical cycles. The spin state can be initialized experimentally by operating a 532 nm laser several times longer than its non-radiative decay lifetime. This fidelity is limited by NV charge state hopping from-to  $NV^0$  [85].

### Spin readout

The following information can be used to determine the spin state. The spin-dependent fluorescence difference is confirmed by non-radiative decay through ISC and its longer lifetime than radiative decay. When observable, the optical contrast appears to be approximately  $C \sim 30\%$ . To confirm this, a 532 nm laser pulse with a level similar to or less than the non-radiative lifetime can be used.

As shown in Figure 2.4(a), After preparing the quantum states for  $|m_s = 0\rangle$  and  $|m_s = 1\rangle$ , a 50 ns measurement time window coordinated with a green laser was used. Time is the interval between the measuring time window and the start of the green laser excitation for measurement. But, because of the larger time window than the excitation state lifetime  $\sim 10$  ns, early excitation analysis is not clearly shown here. As shown in Figure 2.4(b), the photoluminescence generated by the NV displays two features. First, in the  $|m_s = 1\rangle$  state, due to the ISC channel and the non radiative decay channel, the photoluminescence appears darker than in the  $|m_s = 0\rangle$  state, when the photoluminescence is bright. The second is that there is no difference in the amount of light after attempting to green laser pumping for more than 1000 ns due to initialization to  $|m_s = 0\rangle$ . By integrating this signal, we estimate under which conditions it is possible to obtain signal gain while maintaining spin-dependent contrast in photoluminance. Figure 2.4(c) shows the result of accumulating earlier real-time data. The average number of photons that can be acquired during a single measurement tends to increase in both states, and the difference between them remains stable after 1000 ns without further increase. In general,  $\langle N \rangle \sim 0.03$  photons are detected when a 400 ns time window is used for a single-shot measurement. To compare the contrast of this measurement, we can divide the difference in accumulation by  $|m_s = 0\rangle$ . As shown in Figure 2.4(d), the contrast

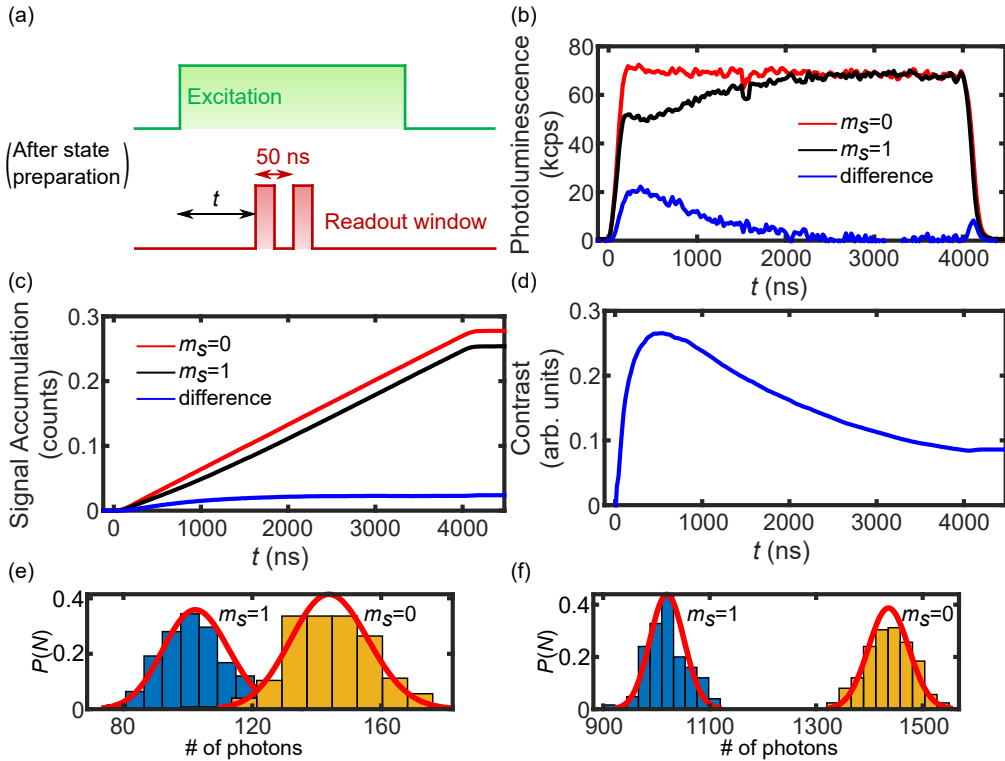


Figure 2.4: Spin readout time analysis. (a) After state preparation, Green laser was used for optical pumping and synchronized readout time window with vary start time from excitation. Two pulses on readout window show start and end timing of measurement. (b) Photoluminescence unit of counts rate in kilo-counts per seconds (kcps). (c) Accumulated signal from two state and its difference. (d) The contrast is calculated signal accumulation difference divided by signal accumulation of  $m_s = 0$ . (e, f) Photon statistics with 5000 and 50 000 reps.

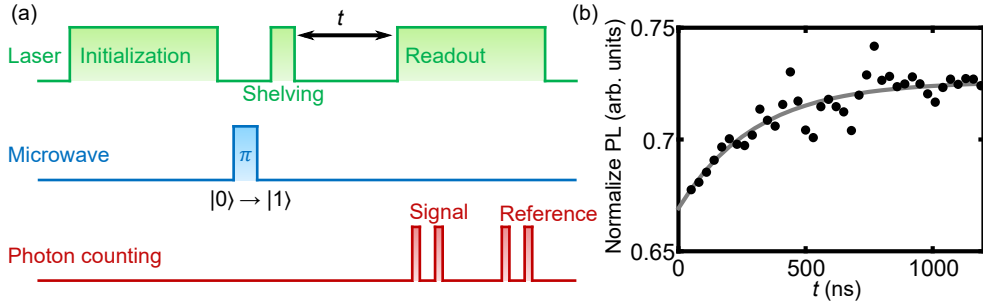


Figure 2.5: Depopulation time measurement. (a) Pulse sequence for depopulation measurement. “ $\pi$ ” means pi pulse. (b) Result of depopulation time for time.

reaches its highest value approximately 300 ns, and the longer the measurement duration, the more it approaches zero. If contrast is not considerably reduced when the readout time is slightly increased, a readout time of  $\geq 300$  ns is used, since it is possible to gain more signal by gently raising the readout time. As shown in Figures 2.4(e-f), photon statistics was demonstrated with different spin states. After preparing the spin state, data was collected by performing a single measurement of 400 ns readout time and initialization for 5000 repetitions in Figure 2.4(e) and for 50 000 repetitions in Figure 2.4(e). This measurement was taken 200 times and analyzed statistically. Since a single NV with a signal of nearly 70 kcps was used for comparison, approximately  $\langle N \rangle \sim 0.028$  photons were measured at a readout time of 400 ns and approximately 144.3(17) counts were acquired after 5000 repetitions. The histogram on the right side of Figure 2.4(e) displays the counts in the  $|m_s = 0\rangle$  state, which were fitted with a Poisson distribution to measure an average of 144 counts. In comparison, when prepared in  $|m_s = 1\rangle$  state, an average of 102.8(14) counts is measured, as shown by the histogram on the Figure 2.4(e) left. This distribution has a line width of roughly 13 and 11 counts, and there is overlap within the distribution, therefore it may be difficult to distinguish fully when measured. In comparison, when 50 000 repeats are counted as seen in Figure 2.4(f), the two distributions are 1436.4(53) counts and 1020.1(44) counts, which are far off from one another, making it easy to distinguish between them. Additionally, since the line width of the histogram is 43 counts and 38 counts, the ratio of the measured value

to the line width, namely the SNR of the measurement, is improved. Actually relatively, the SNR of contrast for 5000 repeats is  $\text{SNR}_{5000} \sim \frac{144-102}{13} = 3.2$  and for 5000 repetitions it is  $\text{SNR}_{50000} \sim \frac{1436-1020}{43} = 9.6$ . On the other hand, the spin-to-charge conversion technique can be used to improve the SNR when measuring after a long period of time, such as a  $T_1$  relaxation measurement [86].

By exploring the dynamics in the spin readout and the depopulation time as a characteristic of the NV centers, it is possible to transition from the excited state  $|m_s = 1\rangle$  to the ground state  $|m_s = 0\rangle$  via the non-radiative decay channel. This time is called the depopulation time. The timing length can be measured using the pulse sequence shown in Figure 2.5(a). The process of measurement is outlined as follows. At first,  $|m_s = 0\rangle$  is prepared by initialization and subsequently transformed into  $|m_s = 1\rangle$  with the use of a  $\pi$  pulse. This  $\pi$  pulse will be described in further detail in Section 2.2.2 on Rabi oscillation. Second, a short laser pulse with  $\sim 100$  ns is used to shelve it into the  $|m_s = 1\rangle$  excited state. The short laser pulse is utilized due to avoid initialization spin state by a long laser pulse. Third, the spin readout is performed after a duration of  $t$ .

The photoluminescence result shown in Figure 2.5(b) is acquired by measuring the depopulation time. Data is fitted by  $\text{PL}_0 + \Delta\text{PL}e^{-\tau/\tau_0}$  where  $\tau_0 = (3.0 \pm 2.0) \times 10^3$  ns. After shelving, it can be observed that nearly  $\sim 70\%$  of the population in the excited spin 1 state show photons emitting within  $< 10$  ns, subsequently returning to the ground state spin 1 state. The remaining  $\sim 70\%$  of the population, however, undergoes non-radiative decay. There, only  $\sim 70\%$  of  $|m_s = 1\rangle$  will contribute to photoluminescence, which is relatively small. On the contrary, after the depopulation time, the initial  $30\%$  of the population decays to the ground state  $|m_s = 0\rangle$ . The spin readout shows that  $30\%$  of  $|m_s = 0\rangle$  and  $70\%$  of  $|m_s = 1\rangle$  contribute to photoluminescence, resulting in a relatively bright measurement.

The initialization process includes the depopulation process. The depopulation time is due to the internal structures of the ISC and the non-radiative decay channel. The power of the pumping laser is not an important consideration for the depopulation time. Initialization, on the other hand, is determined by the amount of transfer through the depopulation channel produced by chances of pumping in the spin triplet. Consequently, a positive correlation

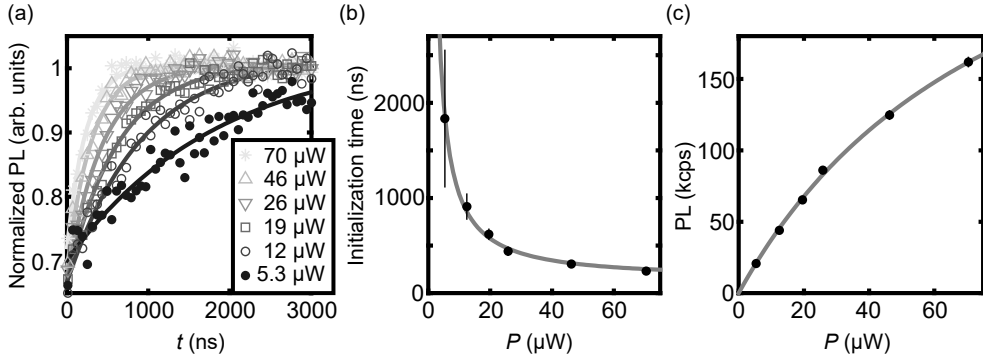


Figure 2.6: Laser power and initialization and photon counts. (a) Normalized photoluminescence result from time trace when initialization with different pumping laser powers. (b) Initialization time for different powers. (c) Photoluminescence on different laser powers.

exists between the intensity of the laser and the speed of the initialization process.

The measurement process is simple. Initialization and pi pulse are used to prepare the  $|m_s = 1\rangle$  state, and then laser pumping is performed, and the readout is taken after time  $t$  from pumping. Figure 2.6(a) shows the result of the initialization measurement. The experiment consisted of measuring initialization against time at varying laser powers, measured at the objective lens back aperture. According to the findings, the beginning PL is relatively low due to its state  $|m_s = 1\rangle$ . However, with continued pumping, it moves bright because of  $|m_s = 0\rangle$  state. The relationship between power and initialization time is inversely correlated, whereby an increase in power results in a decrease in the time taken to return to  $|m_s = 0\rangle$ . Figures 2.6(b, c) illustrate how results can be investigated for pumping power. The data presented in Figure 2.6(b) indicates a negative correlation between power and initialization time. Specifically, as the power increases, the initialization time decreases. The data is fitted by  $t_0/(1 - e^{-P/P_0})$  where  $t_0 = 193(99)$  ns, and  $P_0 = 48(27)$   $\mu\text{W}$ . The data presented in Figure 2.6(c) indicates that there is a positive correlation between power and PL, which eventually reaches a saturation point. The data is fitted by  $PL_0/(1 + P/P_0)$  where  $PL_0 = 359(50)$   $\mu\text{W}$ , and  $P_0 = 85(18)$   $\mu\text{W}$ .

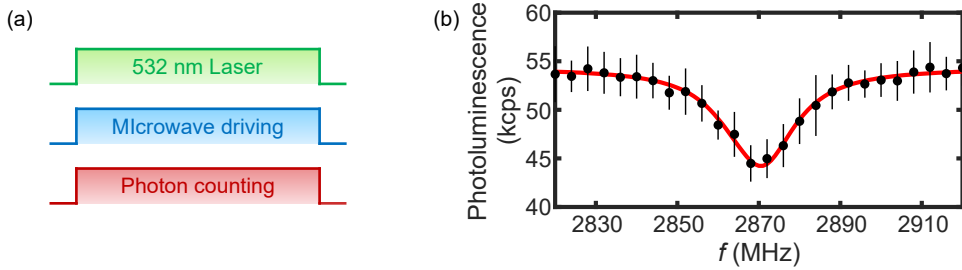


Figure 2.7: Optically detected magnetic resonance. (a) CW-ESR measurement pulse scheme. Optical pumping, microwave driving and photon counting are operated in same time when the microwave frequency is varying. (b) Photoluminescence of ESR spectrum as a function of microwave frequency.

### Optically detected magnetic resonance (ODMR)

We confirmed that the NV center spin can be initialized optically in the same manner as described previously and that the intensity of the light differs depending on the spin state. This allows us to optically measure the paramagnetic resonance of the electron spin of the NV center. This is known as optically detected magnetic resonance.

Easily validate this by observing the continuous wave (CW)-electron spin resonance (ESR). As illustrated in Figure 2.7(a), while continually pumping a green laser, microwaves near the NV ground-state energy are employed, and photons are continuously detected. The spin transition can be confirmed as the frequency of the microwave sweeps approaches the NV ground state of 2.87 GHz. If the microwave frequency is not equal to the NV ground-state energy, the spin remains in the  $|m_s = 0\rangle$  state and the light's brightness remains. When the frequency equals the energy of the NV ground state, the ground state transitions and the darkness of light may be confirmed. The ESR of a single NV spin can be validated, as demonstrated in Figure 2.7(b). Photoluminescence as a function of microwave frequency is derived from ODMR. There is a dip on the spin resonance curve when the microwave frequency matches the ZFS.

So far, we have only considered the optical difference between  $|m_s = 0\rangle$  and  $|m_s = 1\rangle$  without making a distinction between  $|m_s = 1\rangle$  and  $|m_s = -1\rangle$ . Now, the ground state energy

will be investigated in more detail, and the optical detection magnetic resonance method for measuring magnetic fields will be discussed in better detail.

## 2.2 Magnetic field sensing

One myth says that an ancient Greek shepherd tending sheep with an iron staff discovered the staff attached to a particular rock. The rock was magnetite, and because the Magnesia region of Greece is where this magnetite is found in abundance, it is believed that the magnet's name was Magnet. The sheep are also said to have been cared for by a shepherd named Magnes, who gave the name [87].

Magnets have been a part of human existence since the beginning of history. Various spintronics materials and devices are currently the subject of research, and the nanometer-scale imaging technique is important not only for fundamental research but also for information device applications. The Zeeman split of the NV center electron spin can be measured with high spatial resolution and high magnetic field sensitivity.

### 2.2.1 Electron spin resonance with Zeeman split

The energy of the electron spin at the NV center can be calculated quantum mechanically, and several quantum calculation methods follow this reference. Description of NV center ground state Hamiltonian is start simply with

$$\begin{aligned}\hat{H}/h &= D_0\hat{S}_z^2 + \gamma_e\vec{B} \cdot \vec{S} \\ &\simeq D_0\hat{S}_z^2 + \gamma_e B_z \hat{S}_z \equiv D_0\hat{S}_{NV}^2 + \gamma_e B_{NV} \hat{S}_{NV}\end{aligned}\tag{2.2}$$

, where ground level crystal zero field split  $D_0 = 2870$  MHz in room temperature, electron gyromagnetic ratio is  $\gamma_e = g_e\mu_B = 28$  MHz/mT, and  $z$ -axis is NV orientation shown in Figure 2.1(b) [30]. So,  $B_z, \hat{S}_z$  are written as  $B_{NV}, \hat{S}_{NV}$  along the NV axis which will be used to avoid confusing other coordinates. Other energy terms may be added such as hyperfine interaction, temperature shift, strain, and electric field coupling, but let us focus on this for

## Chapter 2. Quantum Sensing with Single Spin in Diamond

now.  $D_0$  is a ZFS that takes  $|m_s = 0, \pm 1\rangle$  to a quantum number. In addition, there is a Zeeman energy term in which the electron spin is induced by a magnetic field. It is defined by the gyromagnetic ratio of the electron  $\gamma_e$ . Because  $D_0$  is large enough compared to  $D_0/\gamma_e \approx 0.1$  T, in  $B_\perp \ll 100$  mT, it can be approximated. From this Hamiltonian, transition levels between  $|m_s = 0\rangle \leftrightarrow |m_s = 1\rangle$  and  $|m_s = 0\rangle \leftrightarrow |m_s = -1\rangle$  are calculated by

$$f_{0\leftrightarrow\pm 1} = D_0 \pm \gamma_e B_z \quad (2.3)$$

, where  $f$  is ESR frequency, and  $B_z$  is magnetic field parallel to NV axis  $B_\parallel$ . We can determine the magnetic field  $B_z = \Delta f/2\gamma_e$  from the two frequencies in the ODMR.

In only with perpendicular magnetic field with  $B_\perp \ll D_0$ , transition frequency is calculated by

$$f_+ = D_0 + 2\frac{\gamma_e^2 B_\perp^2}{D_0}, \quad f_- = D_0 + \frac{\gamma_e^2 B_\perp^2}{D_0} \quad (2.4)$$

, where  $f_+$  is transition between  $|\tilde{0}\rangle \leftrightarrow |+\rangle$ ,  $f_-$  is transition between  $|\tilde{0}\rangle \leftrightarrow |-\rangle$ ,  $B_\perp$  is perpendicular magnetic field  $B_\perp = \sqrt{B_x^2 + B_y^2}$ ,  $|\tilde{0}\rangle \simeq |0\rangle$ ,  $|+\rangle \simeq \frac{|1\rangle+|-1\rangle}{\sqrt{2}}$ , and  $|-\rangle \simeq \frac{|1\rangle-|-1\rangle}{\sqrt{2}}$ . Also, in the case of a strong perpendicular magnetic field  $> 20$  mT, the PL is quenched, which is used in magnetic field imaging [83].

But generally with two component of magnetic field with parallel and perpendicular, transition frequency is calculated by

$$f_{\pm 1} = D_0 \pm \gamma_e B_\parallel + \frac{3}{2} \frac{\gamma_e^2 B_\perp^2}{D_0} \quad (2.5)$$

In this dissertation, we will focus on the parallel magnetic field  $B_{\text{NV}} = B_\parallel$ . As shown in Figure 2.8(a), photoluminescence signal was fitted by summation of Lorentzian functions

$$I(f) \simeq I_0 \left( 1 - C \frac{\Gamma^2/4}{(f - f_1)^2 + \Gamma^2/4} - C \frac{\Gamma^2/4}{(f - f_{-1})^2 + \Gamma^2/4} \right) \quad (2.6)$$

, where  $I$  is photoluminescence intensity,  $C$  is ODMR contrast,  $\Gamma$  is linewidth defined by full

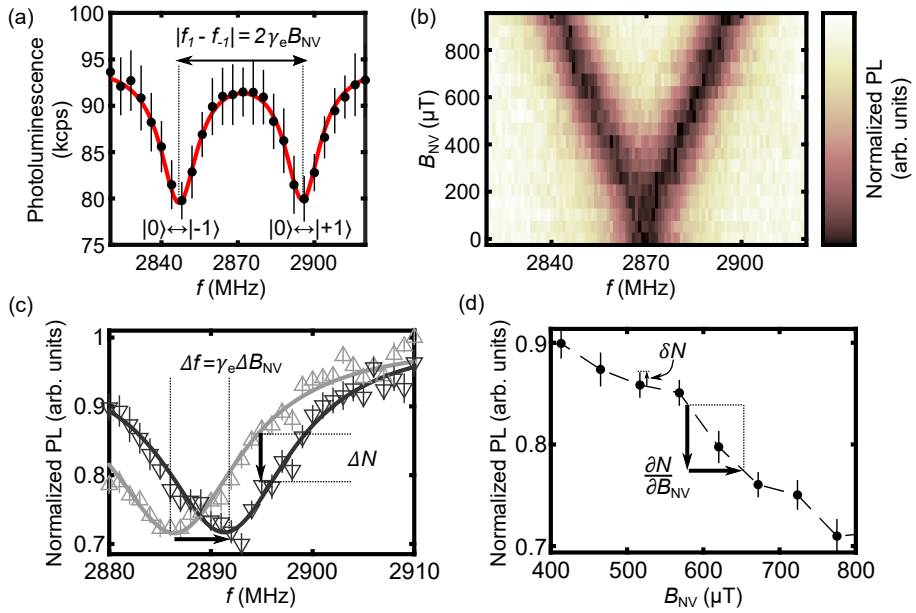


Figure 2.8: ESR spectrum on varying magnetic field. (a) ESR spectrum on magnetic field. (b) ESR spectrum with varying magnetic field. Darker V-shape shows Zeeman split. (c) Comparison ESR result with different magnetic field. (d) Magnetic field sensing using PL change.

width half maximum (FWHM). This line width is typically defined by the rabi frequency related to microwave power. But its downside is limited by the inverse of  $T_2^*$  (called T two star) time. We will derive this Lorentzian function in the Rabi oscillation Equation 2.11. As shown in Figure 2.8(b), the ground spin states of the NV center are subject to change by an external magnetic field via the Zeeman effect. Upon continuous illumination of the pumping laser and GHz microwave photons, ESR transitions of  $|m_s = 0\rangle \leftrightarrow |m_s = -1\rangle$  and  $|m_s = 0\rangle \leftrightarrow |m_s = +1\rangle$  occur. The ESR signals appear as valleys in the photoluminescence measurement due to the dark transitions associated with the  $|m_s = \pm 1\rangle$  states. The sensitivity of the DC magnetic field based on this method is determined by the minimum resolvable frequency shift  $\delta f$  defined as  $\delta f = \frac{\delta N}{\partial N / \partial f}$ , where  $\delta N$  is the minimal resolvable photon counts and  $N$  is the number of photons measured [88].

From this resolvable frequency, minimum detectable magnetic field  $B_{\min}$  and magnetic field sensitivity  $\eta_B$  is defined by

$$B_{\min} = \frac{\delta f}{\gamma_e} \approx \frac{\sqrt{I_0 t}}{\gamma_e C I_0 t / \Gamma} = \frac{\Gamma}{\gamma_e C \sqrt{I_0 t}}, \quad (2.7)$$

$$\eta_B = B_{\min} \sqrt{t} \approx \frac{\Gamma}{\gamma_e C \sqrt{I_0}}$$

, where  $t$  is total measurement time [89]. The magnetic field sensitivity is depending on ‘4C’ which includes ‘Collection of photons’, ‘Contrast of ODMR’, ‘Coherence time’ in single NV center [34], and also ‘Concentration of NV centers’ in the case of ensemble [43, 90, 91].

The relationship between photon counts, contrast, and linewidth with laser power and microwave power is illustrated in Figure 2.6(c), and Figure 2.9. Therefore, experiments are performed after finding the optimal sweet spot for these powers. In a single NV center, the magnetic field measurement sensitivity is several  $\sim \mu\text{T}/\sqrt{\text{Hz}}$ , where linewidth is a couple of tens MHz, contrast is between 0.2  $\sim$  0.3, and intensity is several tens of kcps.

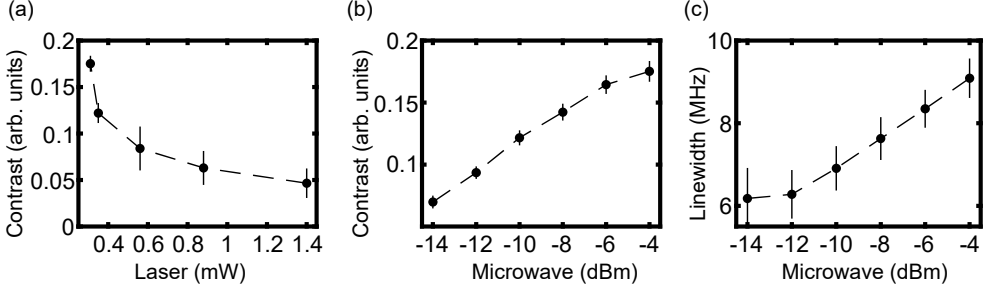


Figure 2.9: Contrast and linewidth are depending on laser and microwave power. (a) Contrast vs. Laser power. (b) Contrast vs. Microwave power. (c) Linewidth vs. Microwave power.

### 2.2.2 Rabi oscillation

By fixing the microwave frequency to one of the ground-state transitions, we can effectively consider a two-level system to simplify our calculations. So, its total Hamiltonian has two parts. First term, the two-level system Hamiltonian is described stationary. Second term, the oscillating magnetic field induced by the microwave is coupled to the electron spin in the NV center. So, Total Hamiltonian is described by

$$\hat{H}/\hbar = \frac{\omega_0}{2}\sigma_z + \Omega_R \cos(\omega t + \varphi) \sigma_x \quad (2.8)$$

, where  $\omega_0 \sim 2\pi \times 2.87$  GHz is an angular frequency of the ground state transition,  $\sigma_z$  is the Pauli  $z$  matrix,  $\Omega_R$  is the Rabi frequency, oscillating magnetic field  $2\pi\gamma_e B_x$  depending on microwave power,  $\omega$  is an angular frequency of the microwave near  $\omega_0$ ,  $\varphi$  is a phase of the microwave,  $\sigma_x$  is the Pauli  $x$  matrix, basis  $|m_s = 0\rangle \equiv |0\rangle = \begin{pmatrix} 0 \\ 1 \end{pmatrix}$ , and  $|m_s = 1\rangle \equiv |1\rangle = \begin{pmatrix} 1 \\ 0 \end{pmatrix}$ .

We can convert these Hamiltonian in the interaction picture as known as rotating frame (See Appendix A). In interaction picture, time independent Hamiltonian is chosen to change frame from Schrödinger picture or Heisenberg picture. The total Hamiltonian is described separately  $\hat{H} = \hat{H}_0 + \hat{H}_1(t)$ . At this time, we choose  $\hat{H}_0/\hbar = \frac{\omega}{2}\sigma_z$  and  $\hat{H}_1(t)/\hbar = \frac{\omega_0 - \omega}{2}\sigma_z + \frac{\Omega_R}{2} \cos(\omega t + \varphi)\sigma_x$ . The new form of ket vectors and operators is calculated with transform using  $\hat{U}_0(t) = e^{-i\hat{H}_0 t}$ , where the ket vector is  $|\tilde{\psi}\rangle = \hat{U}_0(t)^\dagger |\psi\rangle$ , and the Hamiltonian oper-

## Chapter 2. Quantum Sensing with Single Spin in Diamond

ator is  $\hat{H}_I(t) = \hat{U}_0^\dagger \hat{H}_1(t) \hat{U}_0$ . From this,  $\hat{H}_I(t)/\hbar = \frac{\omega_0 - \omega}{2} \sigma_z + \frac{\Omega_R}{2} (\cos(\varphi) \sigma_x + \sin(\varphi) \sigma_y) + \frac{\Omega_R}{2} (\cos(2\omega t + \varphi) \sigma_x - \sin(2\omega t + \varphi) \sigma_y)$ , where  $\sigma_y$  is the Pauli y matrix. Because the rotating wave approximation can reduce terms with  $2\omega t$  in fast rotating regime  $\omega \gg \Omega_R$ , the Hamiltonian is simplified as

$$\hat{H}_I(t)/\hbar = \frac{\Delta\omega}{2} \sigma_z + \frac{\Omega_R}{2} (\cos(\varphi) \sigma_x + \sin(\varphi) \sigma_y) = \begin{pmatrix} \Delta\omega/2 & \Omega_R e^{-i\varphi} \\ \Omega_R e^{+i\varphi} & -\Delta\omega/2 \end{pmatrix} \quad (2.9)$$

, where  $\Delta\omega = \omega_0 - \omega$  is angular detuning frequency. When we match the angular frequency of the microwave  $\omega = \omega_0$  with  $\varphi = 0$  or  $\varphi = \pi/2$ , we can rotate the spin on the Bloch sphere on the  $x$  or  $y$  axis with Rabi frequency  $\Omega_R$ .

Bloch sphere is a representation of the spin expectation values on or in the sphere [92, 93]. State can be written in  $|\psi\rangle = \cos\theta |1\rangle + \sin\theta e^{i\varphi} |0\rangle$ . From this  $(\theta, \varphi)$ , the Bloch vector is represented by  $\vec{S} = (\sin\theta \cos\varphi, \sin\theta \sin\varphi, \cos\theta)$  on the Bloch sphere. In using density matrix  $\rho = \sum_j p_j |j\rangle \langle j|$ , where  $\rho$  is density matrix, and  $p_j$  is probability of  $|j\rangle$ , the Bloch vector generally represents by

$$\rho = \begin{pmatrix} \rho_{11} & \rho_{10} \\ \rho_{01} & \rho_{00} \end{pmatrix} = \frac{1}{2} (I + \vec{S} \cdot \vec{\sigma}) = \frac{1}{2} \begin{pmatrix} 1 + S_z & S_x - iS_y \\ S_x + iS_y & 1 - S_z \end{pmatrix}. \quad (2.10)$$

This Bloch vector  $S$  can be ‘in’ Bloch sphere. In comparison with conventional notation, the north pole of the Bloch sphere will be represented as the  $|1\rangle$  state in this dissertation, so that coefficient of  $\sigma_z$  in the Hamiltonian has a positive value and this procedure is connected by the Rabi oscillation Hamiltonian above Equation (2.8).

Rabi oscillation can be performed with In-phase & Quadrature (IQ) modulation of microwave signal generator to control rotation axis of Bloch vectors. Probability of each state started with  $p_0(t=0) = 1$  is calculated

$$\begin{aligned} p_0(t) &= \cos^2(\sqrt{\Omega_R^2 + \Delta\omega^2} t) + \frac{\Delta\omega^2}{\Delta\omega^2 + \Omega_R^2} \sin^2(\sqrt{\Omega_R^2 + \Delta\omega^2} t) \\ p_1(t) &= \frac{\Omega_R^2}{\Delta\omega^2 + \Omega_R^2} \sin^2(\sqrt{\Omega_R^2 + \Delta\omega^2} t). \end{aligned} \quad (2.11)$$

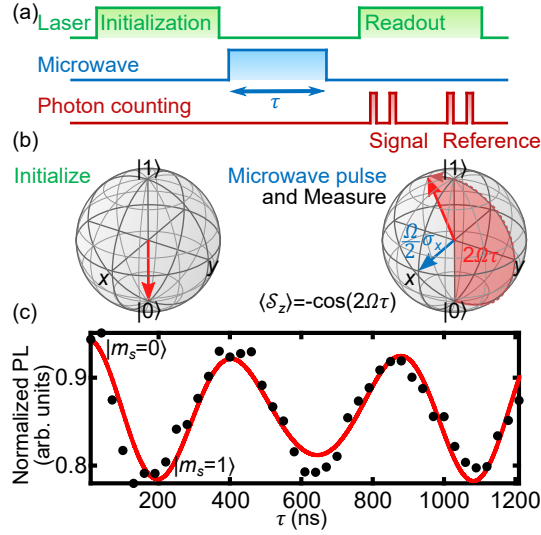


Figure 2.10: (a) Rabi oscillation pulse scheme. Every pulse is synchronized. The microwave pulse is controlled by a switch, and the measurement is performed by varying the duration of the pulse. As the duration of the pulse varies, so do the relative positions of the laser and photon count triggers. (b) Rabi oscillation measurement result. The spin state is readable via photoluminescence. It begins in  $|m_s = 0\rangle$  and changes to  $|m_s = 1\rangle$  after  $\sim 200$  ns. If we use a  $\sim 100$  ns microwave pulse, we can achieve superposition of spin states.

From this equation, We can confirm the Lorentzian curve on its coefficient on sinusoidal term.

It is demonstrated in Figure 2.10. Normalized photoluminescence (PL) value can be used to determine the spin state. This is the photon count of the signal divided by the photon count of the reference. By fitting these time-varying PL data, it is possible to determine the Rabi frequency and determine when the spin state changes. Its Rabi frequency is  $\Omega_R = 2\pi \times 2.34(2)$  MHz. From this result, the transition time from  $|m_s = 0\rangle$  to  $|m_s = 1\rangle$  is 213 ns. We call this time the  $\pi$ (pi)-time. This means that the spin rotated by  $180^\circ$  at this time. In addition, we can determine  $\frac{\pi}{2}$  time, half of  $\pi$  time, rotated by  $90^\circ$ . These  $\frac{\pi}{2}$ ,  $\pi$  time pulses are used for other measurement such as Ramsey, Echo,  $T_1$ , and dynamical decoupling. Rabi oscillation can be used for magnetic field sensing. If our target microwave frequency is

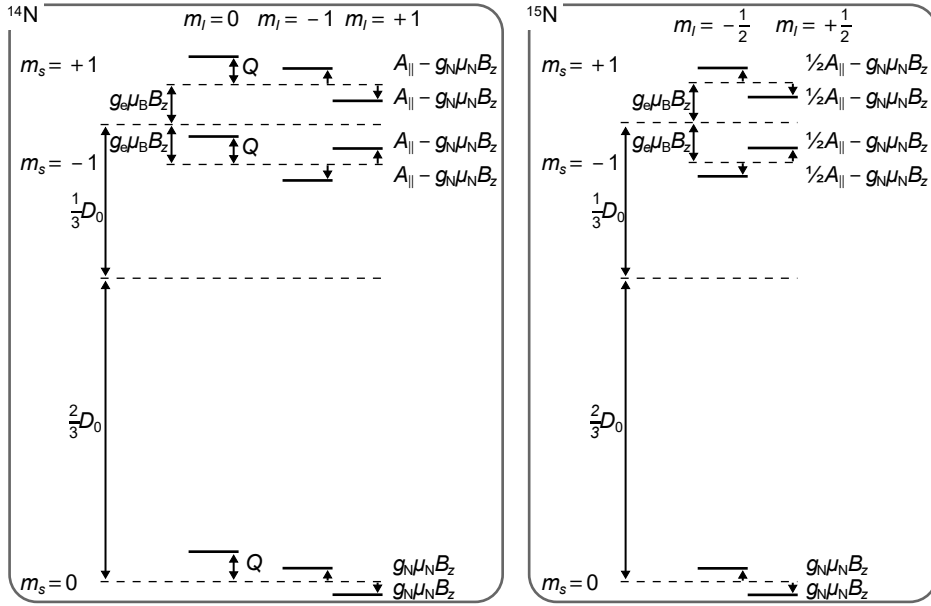


Figure 2.11: Ground state energy level and hyper fine interaction of NV centers with  $^{14}\text{N}$  and  $^{15}\text{N}$ . Ground state crystal field split is  $D_0 = 2.87$  GHz in room temperature.

matched with the NV energy level, we may determine the microwave amplitude from the Rabi frequency. Furthermore, this Rabi oscillation measurement is limited by the spin relaxation time  $T_1$ .  $T_1$  is dominantly impacted by high-frequency noise. Additionally, it can be utilized for high-frequency measurement [23].

### 2.2.3 Ramsey measurement

The Hamiltonian of the NV center with hyperfine interaction with nitrogen nuclear spin is described by

$$\begin{aligned} \hat{H}/h = & D_0 \hat{S}_z^2 + \gamma_e \vec{B} \cdot \vec{S} \\ & - \gamma_N \vec{B} \cdot \vec{I} + A_{\parallel} \hat{S}_z \hat{I}_z + A_{\perp} (\hat{S}_x \hat{I}_x + \hat{S}_y \hat{I}_y) + Q \hat{I}_z^2 \end{aligned} \quad (2.12)$$

, where nuclearspin gyromagnetic ratio is  $\gamma_N = g_N \mu_B = 3.08$  kHz/mT for  $^{14}\text{N}$  and  $\gamma_N = 4.32$  kHz/mT for  $^{15}\text{N}$ , nuclear quadrupole coupling is  $Q = -5.01$  MHz for  $^{14}\text{N}$  and  $Q = 0$

for  $^{15}\text{N}$ , hyperfine parameter are  $A_{\parallel} = -2.14$  MHz,  $A_{\perp} = -2.70$  MHz for  $^{14}\text{N}$  and  $A_{\parallel} = 3.03$  MHz,  $A_{\perp} = 3.65$  MHz for  $^{15}\text{N}$  [94]. These main hyperfine parameters are Fermi-contact interaction and off-diagonal terms are zero because of NV symmetry. So, ESR transition levels  $D - g_e \mu_e B_z - A_{\parallel}$ ,  $D - g_e \mu_e B_z$ ,  $D - g_e \mu_e B_z + A_{\parallel}$  are defined in  $|m_s = 0 \leftrightarrow -1, m_I = -1, 0, 1\rangle$  of  $^{14}\text{N}$ . And,  $D - g_e \mu_e B_z - \frac{1}{2}A_{\parallel}$ ,  $D - g_e \mu_e B_z + \frac{1}{2}A_{\parallel}$  are defined in  $|m_s = 0 \leftrightarrow -1, m_I = \pm \frac{1}{2}\rangle$  of  $^{15}\text{N}$ . And, Hamiltonian with other nuclear spin such as  $^{13}\text{C}$  is described by

$$\hat{H}/h = -\frac{\mu_0 \gamma_e \gamma_I h}{16\pi^3 r^3} (3(\vec{S} \cdot \hat{r})(\vec{I} \cdot \hat{r}) - \vec{S} \cdot \vec{I}) \quad (2.13)$$

, where  $\mu_0 = 4\pi \times 10^{-7}$  H/m is vacuum permeability,  $\gamma_I = 10.7$  MHz/T is gyromagnetic ratio of  $^{13}\text{C}$ ,  $r$  is distance from a nuclear spin, and negative sign is due to negative electron spin [95]. Typically, energy with  $^{13}\text{C}$  in within  $\sim \text{nm}^3$  lattice is  $\sim$  kHz. There are 1.1 % of  $^{13}\text{C}$  in naturally without isotropic purification, So  $\frac{8 \text{ atoms}}{(3.57 \text{ \AA})^3} \times 1 \text{ nm}^3 = 2 \text{ atoms}$

We can focus on the NV ESR with weak microwave power to determine this nitrogen nuclear spin energy level. As shown in Figures 2.12(a,b), the nuclear spin energy levels are indicated. For Figure 2.12(a), it shows the energy level of NV center with  $^{14}\text{N}$ . There are 3 valleys with transitions between

$$|m_s = 0, m_I = -1, 0, 1\rangle \leftrightarrow |m_s = 1, m_I = -1, 0, 1\rangle \quad (2.14)$$

states. For NV with  $^{15}\text{N}$ , There are two energy levels in nuclear spin states. So, there are 2 valleys with the transitions between

$$|m_s = 0, m_I = \pm \frac{1}{2}\rangle \leftrightarrow |m_s = 1, m_I = \pm \frac{1}{2}\rangle \quad (2.15)$$

states shown in Figure 2.12(b).

The Ramsey measurement is similar to pulse methods such as Rabi oscillation measurement in principle but utilizes microwave pulses differently. To actually implement the Ramsey measurement, we must first determine the Pi time from the Rabi measurement. The

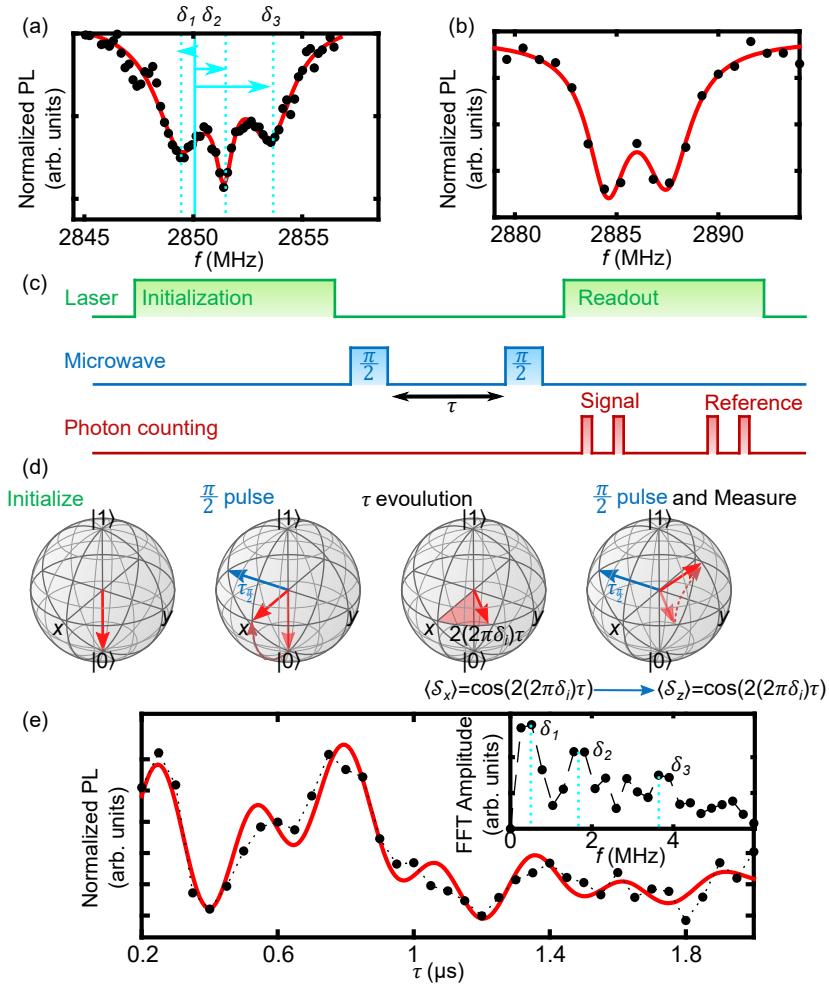


Figure 2.12: Ramsey measurement. (a) and (b) Hyperfine structure of NV center with  $^{14}\text{N}$  and  $^{15}\text{N}$ . (c) Ramsey experiment pulse scheme. There are 3 valleys in (b) with  $m_I = 0, \pm 1$  transitions, and 2 valleys in (c) with  $m_I = \pm \frac{1}{2}$  transitions. (d) Ramsey experiment on in condition (b).

Ramsey measurement requires the creation of a superposition of states and the subsequent observation of their interference. The following is a detailed explanation on how to make a Ramsey measurement on an NV center in diamond shown in Figures 2.12(c,d).

At first, the NV center should be initialized in the  $|m_s = 0\rangle$  state. This is often performed by optically pumping the NV center to its ground state spin  $|m_s = 0\rangle$  using a green laser. Initialization should take only a few microseconds. Two microwave pulses are required. It is the initial microwave pulse. We apply a microwave pulse of duration  $\frac{\pi}{2}$  to the NV center. This pulse is resonant with the transition between the spin states  $|m_s = 0\rangle$  and  $|m_s = 1\rangle$ , and provides a superposition of these two states. The Rabi oscillation frequency determines the duration of the  $\frac{\pi}{2}$  pulse, which is typically on the order of several tens of nanoseconds. Let the NV center freely evolve in the magnetic field for a free precession time  $\tau$ . During this interval, the superposition of states will accumulate a relative phase that is dependent on the duration and the detuning frequency  $\delta_i$  related to the magnetic field. The detuning frequency  $\delta_i$  is defined by

$$\delta_i = f_{\text{MW}} - f_i \quad (2.16)$$

, where  $f_{\text{MW}}$  is the microwave frequency represented by solid line shown in Figure 2.12(a), and  $f_i$  are the NV center transition energy on each hyperfine levels shown in dashed lines in Figure 2.12(a). We apply a second microwave  $\frac{\pi}{2}$  pulse. This pulse rotates the superposition states, causing interference of the  $|m_s = 0\rangle$  and  $|m_s = 1\rangle$  states when the system is measured. Shortly, we measure the  $x$  component of the Bloch arrow using the  $\frac{\pi}{2}$  pulse converting it to the  $z$  component of the Bloch arrow that we can readout. Using readout pumping laser pulse, we evaluate the state of the NV center. We determine the probability that the NV center is in the  $|m_s = 1\rangle$  state by collecting the photoluminescence. The intensity of the measured photoluminescence is correlated with the population under  $|m_s = 1\rangle$  conditions. Repeat the experiment with various values of the free precession time. The collected data will show a pattern of oscillations. Examine the data by fitting the Ramsey measurement to a sinusoidal function with a decay envelope indicating exponential decay shown in Figure 2.12(e). The decay time constant of the envelope is equal to the inhomogeneous decay time or the free

## Chapter 2. Quantum Sensing with Single Spin in Diamond

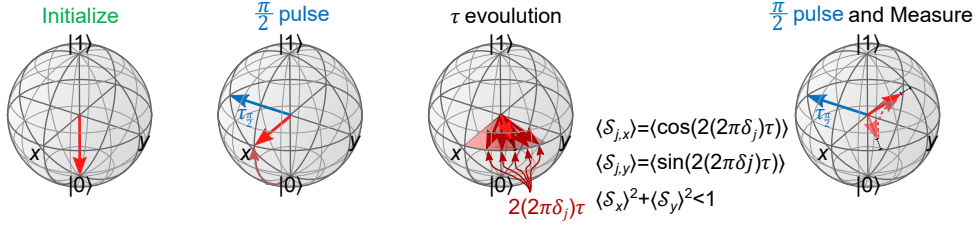


Figure 2.13: Qualitative graphical description of decoherence and  $T_2^*$  when Ramsey measurement.

induction decay time  $T_2^*$ .

This method is used for DC magnetic field sensing. The detuning frequency offers information on the Zeeman shift caused by the magnetic field when performing the Ramsey measurement to estimate the magnetic field applied on the NV center. The Zeeman shift is caused by the interaction between the magnetic field and electron spin of the NV center, which causes splitting of its energy levels. The detuning frequency is extracted from the Ramsey measurement data such as Figure 2.12(e). If the detuning frequency varies, the magnetic field change is detected by using a Zeeman split. The difference in the magnetic field is described by  $\Delta\delta_i = \gamma_e\Delta B$ . The sensitivity of this measurement is confined to  $T_2^*$  in the measurement. If the  $T_2^*$  is longer, smaller variations in the magnetic field can be observed.

Coherence and decoherence will be discussed to explain  $T_2^*$ . Decoherence is the loss of quantum coherence of a quantum system. Quantum coherence is a feature that enables qubits to remain in a superposition of states and complete quantum operations. The interaction of qubits with their environment causes decoherence by inducing noise and random perturbations into the quantum system [93]. This interaction makes the quantum state (pure state) into a mixed state, resulting in the degradation of the quantum information contained in the qubits.

In short, the superposition state is a state with a  $|0\rangle$  and a  $|1\rangle$ . If the qubit is coherent, the states  $|0\rangle$  and  $|1\rangle$  can interfere with each other, and if it is decoherent, the states  $|0\rangle$  and  $|1\rangle$  cannot interfere with each other.

So,  $T_2^*$  will be described as an example. The inhomogeneous dephasing time  $T_2^*$  is a time

of how fast this dephasing occurs due to the environment. In a system of spin qubits, such as NV centers, for instance,  $T_2^*$  indicates the time it takes for the phase difference between the qubits to become randomized because of fluctuations in the local magnetic fields. When a qubit is exposed to a magnetic field, its state begins to precess about the the axis of magnetic field. The qubit would process coherently and retain their relative phases in a perfect system. This is because both qubit states are accumulating up their phases. Nevertheless, due to environmental factors, such as fluctuations in the local magnetic field, the qubit in the ensemble will undergo slightly different magnetic fields, applying it to precess at slightly different frequencies. In the graphical description using the Bloch sphere, dephasing corresponds to the spreading or divergence of the trajectories of an ensemble of precessing qubits around the magnetic field axis, as shown in the dark red arrows in Figure 2.13. This causes the distribution of qubit states on the Bloch sphere to become more widespread, like dark red arrows, resulting in a loss of phase coherence between the qubits. So, the length of the red arrow that is the ensemble of the dark arrows decreases in the Bloch sphere. It is described by decreasing to zero of the off-diagonal components in Equation 2.10.

Techniques such as spin echo and dynamical decoupling (DD) can be used to minimize the impacts of dephasing [96]. These techniques include applying a sequence of pulses to the qubits in order to refocus the phase variations resulting from dephasing. Therefore, it is capable of increasing the coherence time  $T_2$  beyond the inhomogeneous dephasing time  $T_2^*$ , providing more robust quantum operations. Therefore, echo measurement and  $T_2$  will be discussed.

### 2.2.4 Echo measurement

We will discuss dynamical decoupling such as a Spin-Echo (or Hahn-Echo) and how to use this method for quantum sensing. In general, it looks like the Ramsey measurement. The difference is that a  $\pi$  pulse is added in the center of evolution, as shown in Figure 2.14(a). This  $\pi$  pulse can rotate the spin, eliminating phase accumulation that occurs during evolution times with  $\tau$ . This will be shown with a Bloch sphere in Figure 2.14(b). During the first of evolution, phase  $\varphi_1$  is accumulated. The Bloch arrow then revolves around the y-axis with

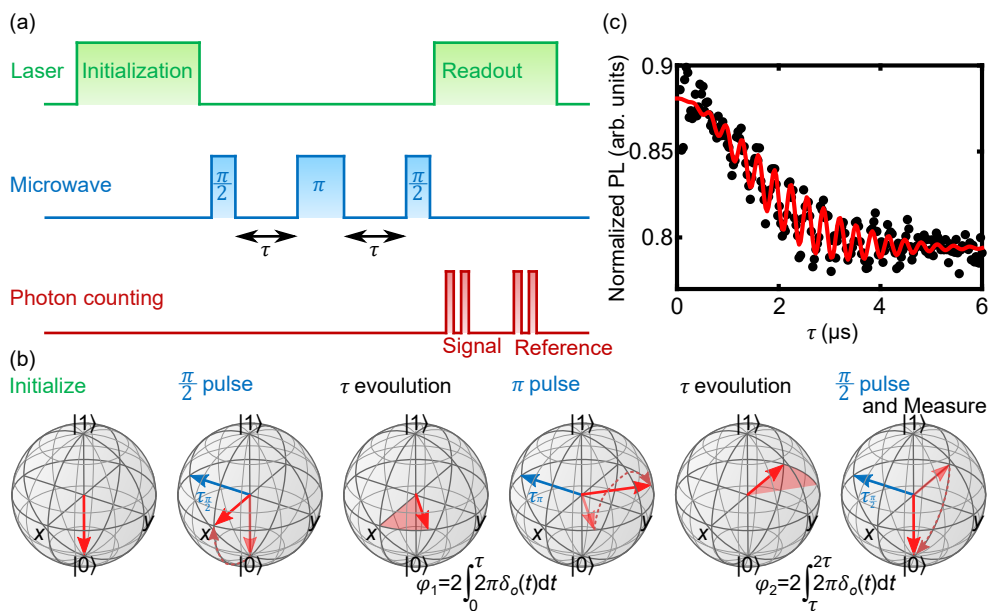


Figure 2.14: Hahn-Echo measurement. (a) Pulse scheme of Echo measurement. (b) Graphical representation of Echo measurement in the Bloch sphere. (c) Echo measurement example with ESEEM in  $^{15}\text{N}$ .

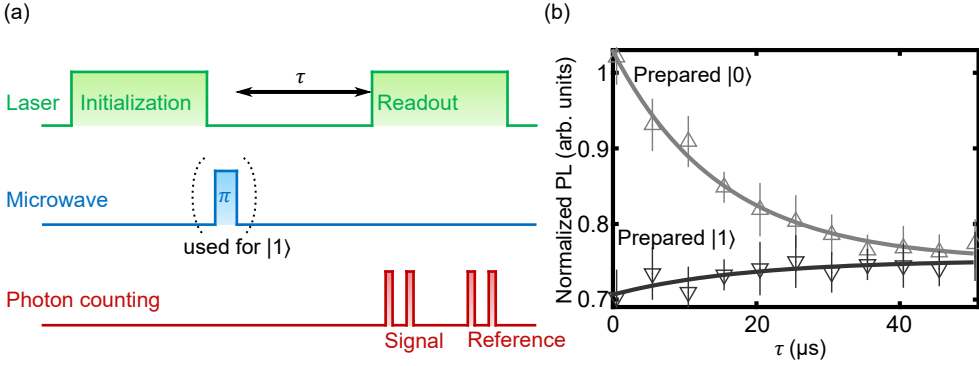


Figure 2.15:  $T_1$  measurement (a) Pulse scheme of  $T_1$  measurement. If the  $\pi$  pulse displayed in the dashed round bracket is utilized, it prepares  $|1\rangle$  state, and if it is not, it prepares  $|0\rangle$  state. (b) Result of  $T_1$  measurement. There are two results prepared at  $|0\rangle$  and  $|1\rangle$  states.

the  $\pi$ -pulse to reach the equator. The phase  $\varphi_2$  then accumulates during the second evolution. The  $\varphi_1$  and  $\varphi_2$  will be equalized and canceled each others if  $\delta_o(t)$  is induced by a DC field independent of time. Consequently, applying again the  $\frac{\pi}{2}$  pulse will allow the spin to return to its initial condition of  $|0\rangle$  state. However, if an AC field with a period equal to  $2\tau$  exists, the phases will not cancel and the two phases will constructively interfere. In contrast to the Ramsey measurement, the Echo measurement reduces DC noise by not detecting the DC field and shifting a noise-sensitive frequency by  $\frac{1}{2\tau}$ . This noise-sensitive area is known as the filter function, and it may be determined by using different dynamical decoupling methods [97]. So, this Echo measurement could be used to AC fields sensing.

Figure 2.14(c) shows the results of the Echo measurement. In this case, the envelope obtained from the echo measurement depends on the coherence time  $T_2$ . The envelope of the NV center with  $^{15}\text{N}$ , which differs from  $^{14}\text{N}$ , presents a  $\sim 3$  MHz oscillation. The oscillation in the envelope is produced by electron spin echo envelope modulation (ESEEM) [95].

### 2.2.5 Spin-lattice relaxation measurement

The time taken to reach thermal equilibrium is the spin-lattice relaxation time  $T_1$ . According to Equation 2.1, the energy at the  $\sim$  GHz level of the NV ground state is significantly less

## Chapter 2. Quantum Sensing with Single Spin in Diamond

than the thermal energy. The partition function calculation results in the probability of the NV center being in all ground states in thermal equilibrium is almost the same. Using optical or electron spin resonance techniques, we can modulate the spin state of the NV center  $|0\rangle$  or  $|1\rangle$ , but at thermal equilibrium it becomes a mixed state with the same probability in all states. This  $T_1$  time is affected by the temperature. Temperature has a major effect on the  $T_1$  time of the NV centers. At low temperatures  $< 100$  mK, the  $T_1$  time can be measured in ms or even longer, but at room temperature it can decrease to several tens of  $\mu$ s or even shorter [62]. Also, it is affected by high frequency magnetic noise, so it is used to measure high frequency magnetic fields [23, 86]. This  $T_1$  measurement is due to the fact that at higher temperatures, the system is more dependent on interactions with lattice vibrations (phonons), which might result in rapid energy dissipation and spin relaxation. This is simple to measure experimentally. The Figure 2.15(a) shows two techniques, the first of which is to utilize a  $\pi$  pulse after initialization to get the spin to state  $|1\rangle$  and then measure the spin state after  $\tau$  time. The second technique involves measuring the spin state after  $\tau$  time has finished after initialization to state  $|0\rangle$ . Using both techniques, we can confirm that the time scales of the two observations from spin  $|1\rangle$  and spin  $|0\rangle$  to the mixing state are identical.

This chapter covered the basic structures and measurement of NV centers. The next chapter shows how to realize these measurements experimentally and utilize them to construct a single scanning magnetometer.

## Chapter 3

# Nanoscale Imaging Experiment Setup

We have a little compass known as the NV Center [88]. In this chapter, we will describe an experimental method to explore solid-state physics systems by placing this compass on a scanning probe microscope, which is a ship shown in Figure 3.1. A solid-state physics system is one in which spins are ordered or whirled like vortex, or in which a current flows and a magnetic field is produced around the current. To perform the experimental method, we present confocal microscopy, a technique that can optically address and read individual NV centers. In addition, the microwave experiment equipment used to realize the ODMR and the electrical device used to detect the optical signal will be described. Finally, we will describe how to connect the previous experimental setup with the scanning probe microscope and how to use it to perform single spin scanning magnetometry.

### 3.1 Confocal optics

By utilizing a confocal microscope to optically measure the single electron spin of a single NV center, research using a single NV center has begun to get attention [98]. In this section, we will introduce confocal optics to address NV centers in diamonds.

Before starting about confocal optics, all optical components and equipment written in Table 3.1. are on an optical table. Using an optical table serves two purposes: isolating the

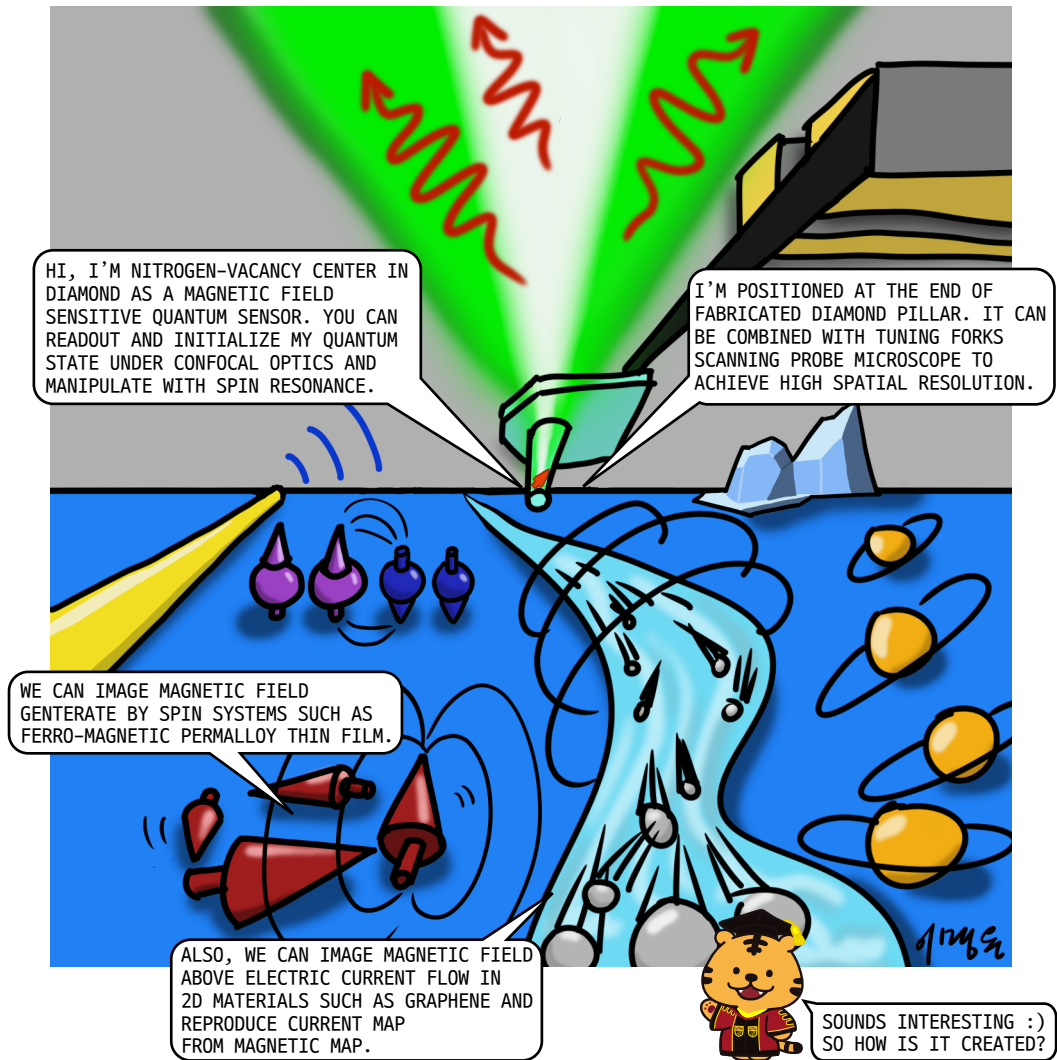


Figure 3.1: A cartoon describing dissertation experiments. In the middle of the figure is a diamond probe with a small red arrow indicating to a single NV center. Above this, an optics that focus a green laser and tuning forks at scanning probe microscope are attached to the diamond probe. On the bottom left of the picture, there is a radio antenna that creates spin resonance. Next to it are magnets that represent spin systems, and then there is a picture of a current with electrons moving through it. On the far right, the orbital magnetic moment is displayed. In the background, a cold iceberg is visible.

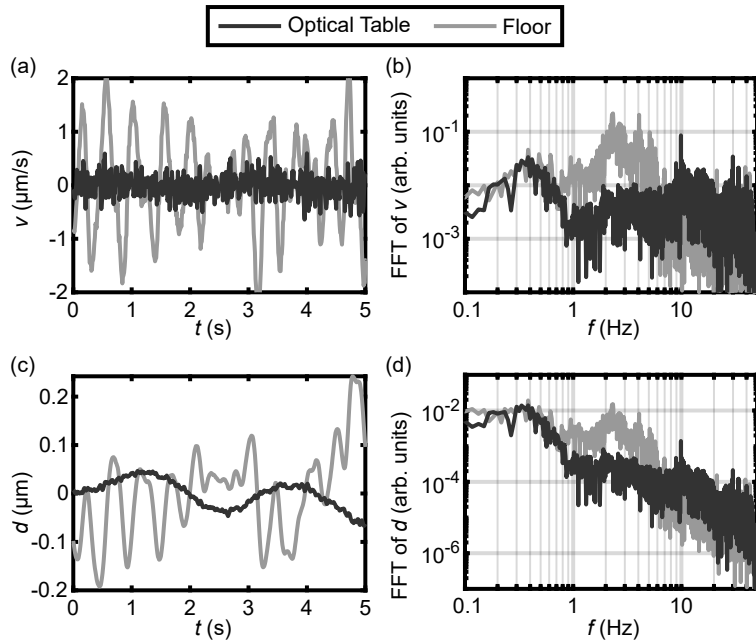


Figure 3.2: Vibration level on an optical table and a floor. (a) Time trace of vertical velocity. (b) Frequency spectrum of velocity. (c) Time trace of vertical distance. (d) Frequency spectrum of distance.

### Chapter 3. Nanoscale Imaging Experiment Setup

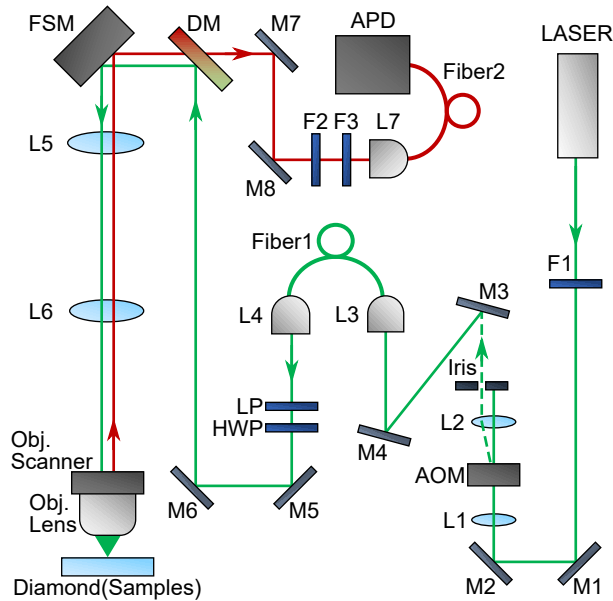


Figure 3.3: Optical components of confocal microscopy. Each components details are written in Table 3.1.

optics from external vibrations and fixing the optics. To protect the optics from vibration noise, the optical table is made up of a few hundred kilograms of iron and columns that float it above the ground. This is represented by an oscillator with a large mass and damping. So, it has a low natural frequency, and is able to block the transmission of higher frequency vibrations. Columns are suspended by nitrogen gas or pump pressure.

Figure 3.2 shows the vibrational characteristics that were measured using a geophone on an optical table and its floor. A geophone is an instrument that uses inertia and electromagnetic induction to measure vibration and earthquakes. The velocity results are shown in Figure 3.2(a) for time and Figure 3.2(b) for frequency spectrum. The displacement results are shown in Figure 3.2(c) for time and Figure 3.2(d) for frequency spectrum. On the optical table, both the velocity and the amplitude of the displacement are reduced, and the high frequency noise is also suppressed.

The description of confocal microscopy begins with excitation 532 nm CW laser. This solid state laser is used for pumping NV centers in off resonant excitation. We used 532 nm

### 3.1. Confocal optics

Components	Description	Vendor	Part No.
Laser	100 mW CW solid state 532 nm laser	CNI	MLL-III-532
F1	ND Filter Series, Optical Density: 0.4	Thorlabs	NE04A
M1-6	Silver Mirrors	Thorlabs	PF10-03-P01
L1	AOM Focus Lens $\mathcal{F} = 125$ mm	Thorlabs	LA1986-A
AOM	Acousto-Optic Modulator, TeO <sub>2</sub> , 200 MHz	IntraAction	ATM-200C1
L2	AOM Collimate Lens 250 mm	Thorlabs	LA1461-A
Iris	Block Iris Diaphragms	Thorlabs	SM2D25
Fiber1	Optical Fiber for Green Laser	Thorlabs	P3-460B-FC-2
L3	Fiber Couple Lens $\mathcal{F} = 6.2$ mm	Thorlabs	C171TMD-A
L4	Fiber Port Lens $\mathcal{F} = 11$ mm	Thorlabs	C220TMD-A
LP	Nanoparticle Linear Polarizer	Thorlabs	LPVIS050-MP2
HWP	Half Wave Plate 532 nm	Foctek	WPC225H-532
DM	Dichroic Beamsplitter 560 nm	Semrock	FF560-Di01-25x36
FSM	Fast Steering Mirror, 2-axis, $\pm 1.5^\circ$	Newport	FSM-300-02
L5	Scanning Mirror $\mathcal{F} = 300$ mm	Thorlabs	AC508-300-B
L6	Scanning Mirror $\mathcal{F} = 750$ mm	Thorlabs	AC508-750-B
Obj. Scanner	Objective Piezo Scanner, 250 $\mu$ m	nPoint	nPFocus250
Obj. Lens	Objective Lens 50x	Olympus	LCPLFLN50xLCD
M7,M8	Broadband Dielectric Mirror 400 – 750 nm	Thorlabs	BB1-E02
F2	Notch Filters 532 nm	Thorlabs	NF533-17
F3	Long pass filter 594 nm	Semrock	BLP01-594R-25
L7	Fiber Collection Lens $\mathcal{F} = 8.0$ mm	Thorlabs	C240TME-B
Fiber2	Optical Fiber for Photoluminescence	Thorlabs	P1-830A-FC-2
APD	Single Photon Count Module	Excelitas	SPCM-AQRH-10-FC

Table 3.1: Optical components used for confocal optics. The positions of the components are shown in Figure 3.3.

### Chapter 3. Nanoscale Imaging Experiment Setup

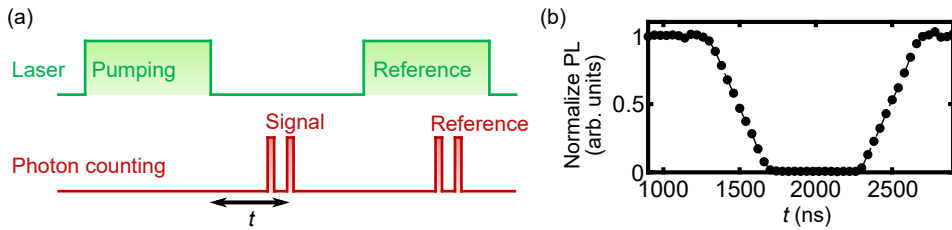


Figure 3.4: AOM delay measurement. (a) The pulse sequence for AOM delay measurement. (b) Photoluminescence data vs. time result of AOM delay measurement.

CW with 100 mW power laser. The beam from the green laser passes through a couple of neutral-density (ND) filters to optimize the focused laser power at the end of the microscope and block the laser beam for returning to the laser as shown in F1 of Figure 3.3. This laser beam is then aligned with the lens and Acousto-optic modulator (AOM) after being reflected by two mirrors labeled M1 and M2. Because of their capacity to control both the position and angle of the laser beam, the two mirrors are used in pairs. For instance, if we use a single mirror to control the position, its position will determine the angle. However, using two mirrors in pairs allows you to adjust both. The laser generates a beam that is collimated. Furthermore, the laser beams reflected from the two mirrors are collimated. The laser beam is focused on the AOM by passing through the L1 lens. Since the focal length of the L1 lens is 125 mm, the AOM is 125 mm away from the L1 lens. The AOM is a device that modulates light using the acoustics of the inner crystal. Microscopically interacting phonons in the inner crystal with photons traveling through the crystal changes the momentum of light. This AOM is powered by a radio frequency of 200 MHz. While the AOM is not being driven, the beam simply passes through the AOM; however, when the AOM is being driven, the beam separates into light with various momentum. We can turn ON and OFF the beam using only one of these separated beams. These AOM beams are collimated by passing through the L2 lens. The focal length of the L2 lens is 250 mm, which is twice that of the L1 lens, expanding the diameter of the beam by double. These beams are blocked at the aperture. Only one of the beams can pass through the aperture, the beam that splits when the AOM is driven. Therefore, we can only excite and read the sample when the AOM is driven.

Let us describe the practical use of AOM. The AOM used in this instance is an element of equipment that drives a mechanical oscillator. Therefore, running the devices takes time. This AOM time delay should be synced with other pulses. Therefore, the AOM delay must be measured, calibrated to the position of other pulses, and synchronized during the actual pulse operation. The measurement method is simple, as shown in Figure 3.4(a). After pumping the NV center for time  $t$ , photon counting follows. At this point, the photoluminescence starts to drop. The AOM delay, which in the example of Figure 3.4(b) delay time is  $\sim 1300$  ns, defines the amount of time when the photoluminescence starts to decrease at this time. The following pulse measurements will continue to apply this parameter.

The laser beam is now aligned towards the fiber port after the two mirrors following going through the AOM and iris. Through lens L3, the laser is coupled to a fiber that is attached to the fiber port. Fiber is utilized to isolate the laser part's optics system from the confocal part's optics system and to filter the mode of the used green laser.

Here, a single mode FC/APC fiber with an operating wavelength of 532 nm is used. When selecting a fiber, the wavelength of the light to be transmitted is considered to determine whether it is not constrained by the cutoff wavelength. Additionally, the spatial mode that can pass through the fiber must be given consideration, single mode and multi mode. The diameter of the core of the fiber differs according to the mode. The diameter of single mode fiber is smaller and can only capture light with a single spatial mode. Multimode fiber has a wider diameter and can capture multiple types of light. We used a single mode because it also functions to filter light. We utilized an FC/APC fiber with an angled cut at its end. This enables more light to be emitted instead of being reflected off the fiber's end.

To couple light from the free space to the fiber, lens L3 with a focal length of 6.3 mm was used. The focal length of the lens L4, which collimates light from the fiber, is 11.0 mm. When choosing the L3 lens, the numerical aperture (NA) of the fiber (0.1 – 0.14) must be considered, in addition to the relationship  $\mathcal{D}/2\mathcal{F} < \text{N.A.}$ , where  $\mathcal{D}$  is the diameter of the beam,  $\mathcal{F}$  is the focal length of the lens. If the diameter is too large, for instance, the area of light outside the incidence angle of the fiber cannot be coupled. The NA of L4 must be greater than the NA of the fiber. The L4 used for collimation is approximately twice as large

### Chapter 3. Nanoscale Imaging Experiment Setup

as L3, suggesting that the diameter of light passing through the fiber is approximately twice as large. If the M3, M4 mirrors are utilized properly to couple light to the fiber, approximately 70 – 80 % of the light arrives.

Light that has been collimated now travels via a linear polarizer and a half wave plate. The linear polarizer is an optical component that allows only one polarization of light to pass through and linearly polarizes it. Since we use a diode laser, the light is already over 95 % linearly polarized, but it is filtered again. The next optical component, the half wave plate, enables us to modulate linearly polarized light by rotating the linear polarization to any desired angle. This can be used to change the polarization direction. Although not used here, the quarter wave plate can convert linearly polarized light to circularly polarized light. The linear polarizer can be utilized over a broad range of wavelengths, but the half wave plate can only operate to a single wavelength.

The light now travels aligned after two mirrors, M5 and M6, then onto a dichroic mirror and a fast steering mirror before reaching the 4 –  $\mathcal{F}$  scanning system, which consists of L5 and L6. The dichroic mirror either reflects or transmits light, depending on the wavelength. Therefore, we may use it to reflect the 532 nm used to shine the NV and deliver it to the diamond, while allowing the 600 – 800 nm light from the NV to pass through to the photon counting module. The fast steering mirror is a device that tilts the angle of the reflected light by a small amount. It is used to scan the sample's surface. A galvano mirror can be used instead.

Let us now review the 4 –  $\mathcal{F}$  scanning system. The goal of this method is to image and address a single NV center in a diamond and measure the photons it emits. To explain the imaging process, we will first describe the configuration of the optical system as shown in Figure 3.5(a). Following L5 at a distance of  $\mathcal{F}_5$  from the fast steering mirror, L6 is at a distance of  $\mathcal{F}_5 + \mathcal{F}_6$ . Lastly, there is an objective lens at the  $\mathcal{F}_6$  distance from L6.  $\mathcal{F}_5$  is the focal length of L5, and  $\mathcal{F}_6$  is the focal length of L6. Since four focal lengths of the optical path are required, we call this 4 –  $\mathcal{F}$  scanning optics.

First, let's discuss the beam size of this optical system. When the collimated light is refracted at L5, it becomes focused  $\mathcal{F}_5$  from L5. Subsequently, the light spreads over a distance

Figure 3.5: (a) Schematics of 4- $\mathcal{F}$  scanning microscope. (b) Collection from NV to the end of objective lens. (c) Optical image acquired by confocal optics. Scale bar 1  $\mu\text{m}$ .

of  $\mathcal{F}_6$  and is refracted at L6. The light is collimated at L6 because it began at a distance of  $\mathcal{F}_6$  from L6. Finally, this increases the beam size by  $\frac{\mathcal{F}_6}{\mathcal{F}_5}$ , which makes the green laser beam used to shine diamond. The end result is a beam spot large enough to fill the back aperture of the objective lens. Filling the back aperture sharpens the light's focus, thus minimizing the depth of field. This will decide the object's focal resolution. The diameter of the beam in the direction of light collection from the NV will be reduced by a factor of  $\frac{\mathcal{F}_5}{\mathcal{F}_6}$ . This beam size is considered when designing the fiber port lens for the confocal part front of a single photon counter.

The distance and angle of the laser beam are now described. When the fast steering mirror is tilted at an angle of  $\theta$ , the light is tilted at an angle of  $2\theta$ . The light reflected by  $2\theta$  reaches the optical axis at a distance equal to  $\mathcal{F}_5 \tan(2\theta)$ . Light starting at a focal length  $\mathcal{F}_5$  of L5 is refracted parallel to L5's optical axis. After going through  $\mathcal{F}_5 + \mathcal{F}_6$ , light parallel to this optical axis is refracted at position L6. At distance  $\mathcal{F}_6$ , the parallel incident beam is refracted at L6 and passes through the optical axis. This is the location of the objective lens. The incident

### Chapter 3. Nanoscale Imaging Experiment Setup

angle of the collimated light is equal to  $\arctan(\frac{\mathcal{F}_5}{\mathcal{F}_6} \tan(2\theta))$ . Now that the collimated light has arrived, the objective lens will focus this light at a distance of  $\mathcal{F}_{\text{Obj}}$ . And since the angle of incidence is  $\arctan(\frac{\mathcal{F}_5}{\mathcal{F}_6} \tan(2\theta))$ , light will focus on  $\frac{\mathcal{F}_5}{\mathcal{F}_6} \tan(2\theta) \mathcal{F}_{\text{Obj}}$  as shown in Figure 3.5(b).

So, the field of view of this system is calculated by

$$\text{FOV} = \frac{\mathcal{F}_5}{\mathcal{F}_6} \tan(2\theta) \mathcal{F}_{\text{Obj}} = \frac{300 \text{ mm}}{750 \text{ mm}} \times \tan(2 \times (\pm 26.2 \text{ mrad})) \times 3 \text{ mm} \approx \pm 60 \mu\text{m} \quad (3.1)$$

, where all parameters are used in this dissertation. The fast steering mirror we used has 4 digit resolution, so it can be address and image single NV centers in diamond. When the distance of the stage attached to the lens is adjusted, the focus position of the diamond in depth could be adjusted. The stage could move by  $\pm 100 \mu\text{m}$ , which is significantly less than  $\mathcal{F}_6$  to have no effect on the image. NV centers are imaged with this system in Figure 3.5(c). In addition, a piezo stage can be used instead of this 4 –  $\mathcal{F}$  scanning system. It is slower, but easier to make smaller.

We can roughly estimate the upper bound of photon counts at saturation from a single NV center. It will begin with the excited state lifetime of  $\sim 10 \text{ ns}$  of the NV centers. It is assumed that photons radiate uniformly in all directions, ignoring the optical transition dipole direction. These photons are collected using an objective lens with 0.7 NA. NA is specified by  $n \sin \theta$ , therefore light will be captured inside the solid angle defined by  $\Omega_1 = \int_0^{2\pi} d\phi \int_0^{\theta_1} d\theta \sin \theta$ , where  $\theta_1 = \arcsin(0.7) \approx \frac{\pi}{4} \text{ rad}$ . Unfortunately, the diamond refractive index is  $n = 2.42$ , which is a high value. So many photons are caught and cannot exit the diamond. The effective angle  $\theta_2 = \arcsin(\sin \theta / n)$  is defined by Snell's law as shown in Figure 3.5(b). Therefore, the estimated value for the solid angle is 0.26 sr, which is 2% to the total solid angle  $4\pi \text{ sr}$ . To enhance this collection rate, there are study results that suggest the fabrication of a wave guide in the shape of a diamond pillar or a solid immersion lens. In this bare diamond case, The estimated upper bound of photon counts at saturation is computed by

$$\text{PL} \approx \frac{1}{t_{\text{NV}}} \frac{\int_0^{2\pi} d\phi \int_0^{\arcsin(\text{NA}/n)} d\theta \sin(\theta)}{4\pi \text{ sr}} \approx 2 \text{ Mcps} \quad (3.2)$$

### 3.2. Microwave and electronics setups

where  $t_{\text{NV}}$  is NV excited state life time,  $n = 2.42$  is refraction index of diamond, and  $\text{NA} = 0.7$  is numerical aperture of objective lens. In practice, however, a saturation value is on the order of a hundred due to dipole directions, wavelength band, optical mode, polarization, and optical system loss.

Thus, the light from the NV returns to its former path, passing this time across the dichroic mirror. Subsequently, the light is reflected by mirrors M7 and M8 and aligned to the fiber port. Broadband dielectric mirrors are used in this case to capture as much photon as possible from the phonon sideband. This light travels to a single photon counting module after confocal optics. Confocal optics is an optical imaging technique that removes out-of-focus light by a pinhole. For instance, light collected from a source in front of or behind the focused NV is focused in front of or behind the pinhole and cannot pass through because it is not focused at the precise location of the pinhole. Light captured by a light source near to the focused NV is focused near the pinhole and is unable to pass through it. A fiber can serve as an alternative to the pinhole [97]. Because it may be directly linked to the fiber port of the single photon count module, a fiber is used. In this case, the lens utilized to couple to the fiber matches the following focal length

$$\mathcal{F} = \frac{\pi \mathcal{D} \text{MFD}}{4\lambda} \simeq \frac{\pi \times 1.2 \text{ mm} \times 5.8 \mu\text{m}}{4 \times 700 \text{ nm}} \simeq 8 \text{ mm} \quad (3.3)$$

, where  $\lambda$  is the wavelength of the light,  $\mathcal{D}$  is the diameter of the beam in this case defined by back aperture of objective lens and  $\frac{\mathcal{F}_5}{\mathcal{F}_6}$  reduction ratio, and MFD is the mode field diameter of the fiber.

## 3.2 Microwave and electronics setups

The microwave is electromagnetic radiation with frequency from 300 MHz (wavelength is  $\lambda = \frac{c}{f} \simeq 1 \text{ m}$ ) to 3 GHz ( $\simeq 10 \text{ cm}$ ) to 300 GHz ( $\simeq 1 \text{ mm}$ ). The results of electron spin resonance utilizing microwaves are read optically. The optical method was explained in the preceding section. So, how do we process the data read optically? How are the lasers

## Chapter 3. Nanoscale Imaging Experiment Setup

Components	Description	Vendor	Part No.
Microwave Source	RF Signal Generator DC to 4 GHz	SRS	SG384
Microwave Switch	TTL Driven Switch, DC to 5 GHz	Mini-Circuits	ZASWA-2-50DR+
Amplifier	Amplifier 16 W, 1.8 GHz to 4 GHz	Mini-Circuits	ZHL-16W-43+
Circulator	Microwave Circulator 2 GHz to 4 GHz	MECA	CS-3.000
Coupler	Directional Coupler 2 GHz to 4 GHz	MECA	780-dB-3.000
Pulseblaster(PC network)	Programmable Pulse Generator 500 MHz	SpinCore	PBESR-PRO-500-PCI
DAQ(PC network)	Multifunction Data Acquisition	NI	PXIe-6363
GPIB(PC network)	GPIB Module	NI	PXI-GPIB
AOM Driver	RF Driver 200 MHz	Isomet	535C-2

Table 3.2: Electronics and Microwave components. This is utilized to design a microwave and measurement system as illustrated in the Figure 3.6.

and microwaves used in the experiment controlled? In this section, we will describe the microwave and electronic equipment written in Table 3.2 and briefly explain how they are utilized for the processing of data. As shown in Figure 3.6, every device is managed by a desktop. The blue line represents the microwave transfer typically connected with SMA cables, the black line represents the electronic connection, and the green and red line represent optics. On the desktop, there are PCIe slots for the PXI interface that connects DAQ and GPIB, and PCI slots for the pulseblaster. The desktop-connected GPIB, Pulseblaster, and DAQ will be described, but the description will begin with the GPIB to explain the microwave element first.

The desktop-connected GPIB, Pulseblaster, and DAQ will be described, but the description will begin with the GPIB to explain the microwave element first. Using the GPIB, the microwave's power, frequency, and mode are mainly controlled. And through the modulation section of the rare panel for the microwave source, the modulation is adjusted such as I/Q modulation, frequency modulation, etc. This I/Q modulation is used to change the phase of the microwave to define a rotating axis on the Bloch sphere. The modulation part of this experiment is controlled by the signal from the pulse blaster. This microwave source's frequency range to cover the NV center ground state energy. The microwaves generated by the source are sent through a microwave switch. The ON/OFF of the switch is controlled by the Transistor-transistor logic (TTL) signal from the pulse blaster. So, we can generate microwave pulses with several tens of ns from microwaves using the pulse blaster and

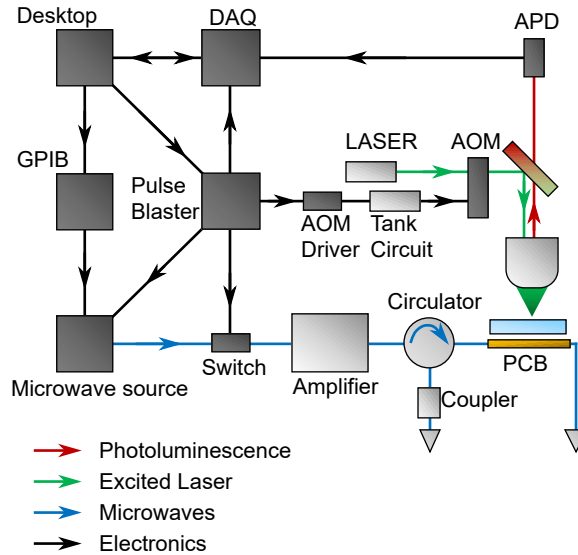


Figure 3.6: Electronic parts. Each components details are written in Table 3.2.

the switch. Microwave pulses are amplified in the amplifier with 45 dB gain. So, it can be achieved to  $\pi$  pulse time with several tens of ns (related to Rabi frequency  $\sim$  MHz, and microwave amplitude  $\sim$  0.1 mT). The circulator is a device that transmits microwaves in one direction, similar to a roundabout road. This device helps to protect the amplifier. The circulator has three ports: the signal entering port 1 is transmitted to port 2, the signal entering port 2 is transmitted to port 3, and the signal entering port 3 is transmitted to port 2. Port 1 is connected to the amplifier's output, and port 2 is connected to the sample. When the amplified microwave reaches the sample and the not terminated microwave is reflected back, it returns to port 2, then exits through port 3, and then terminates. This prevents the power from reflecting back to the amplifier. At the end of the circulator port 3, a coupler and a terminator are connected. The coupler is used to double check the reflected microwave. The circulator port 2 is connected to the sample PCB through a DC block and terminated. On a sample PCB, wiring connected by a wire bonder is used to generate microwaves on NV centers, or the PCB itself designed for an antenna generates microwaves.

In this section, our aim is to explain the role of the pulse blaster. The pulse blaster is

### Chapter 3. Nanoscale Imaging Experiment Setup

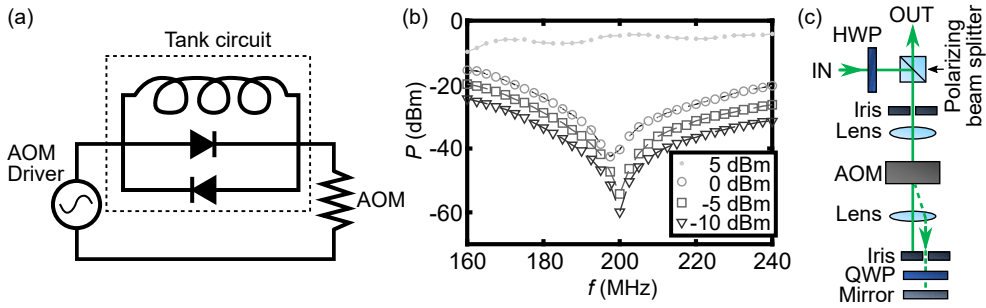


Figure 3.7: AOM leakage reduction (a) Tank circuit diagram. (b) The Bode plot of the tank circuit. (c) Double passed AOM optics.

a device that generates TTL signals synchronized at 500 MHz with 10 ns minimum pulse width and 2 ns resolution, which are then used to produce and control pulses. This pulse blaster is connected with five output usages. First, the first output is connected to the AOM driver, which is used to turn the AOM driver ON and OFF. The AOM driver generates a 200 MHz RF signal that activates the AOM, ultimately enabling the control of the laser pulses ON/OFF. The tank circuit in between will be discussed later. Second, the second output is connected to the DAQ. The trigger is used to adjust the photon counting readout window, which allows the number of photons to be counted within a specified time interval. Third, the third output is connected to the microwave switch, which controls the passage of microwaves and enables the use of microwave pulses. Finally, the fourth and fifth outputs are connected to the microwave source. Specifically, they are connected to the frequency modulation and I/Q modulation of the microwave source rear panel. Using frequency modulation is as simple as plugging it in. In this case, the change is discontinuous and limited to a single frequency difference modulation. However, in the case of IQ modulation, the pulseblaster signal must be modified to utilize the entirety of  $\pm I$ , and  $\pm Q$ . For this purpose, an IQ adder is utilized. This PCB is utilized between the pulseblaster and the microwave source. The  $+X$ ,  $-X$ ,  $+Y$ , and  $-Y$  input signals of the pulseblaster are converted into two  $\pm I$ , and  $\pm Q$  output signals.

The Tank circuit, which is used as a noise eater in the AOM, is described. When the pulse blaster is not activating the AOM driver, the AOM driver still outputs a weak 200 MHz signal. This causes the AOM to operate, allowing light to pass even when the AOM is intended to be

turned off. If light leaks out, there could be unwanted initialization during spin manipulation in the dark state. To prevent this, a noise eater circuit is used. This circuit blocks weak 200 MHz signals when the driver is not in operation, while allowing strong 200 MHz signals to pass through. Other frequencies are permitted to pass as well. To operate at 200 MHz, the frequency  $f$  is defined by  $f = \frac{1}{2\pi\sqrt{LC}}$ . According to the value of  $f$ , the circuit is made with two diodes (1N4148 or 1N914) with opposite directions and capacitance on the scale of pF, along with a coil with inductance on 0.3  $\mu\text{H}$ , as shown in Figure 3.7(a), enclosed in small Pomona electronics box. The results of the transmission measurement of this circuit are presented in Figure 3.7(b). When power is low, RF cannot pass through at 200 MHz, but it can pass through when power is 5 dBm. In practice, when the AOM is turned on, 8.35 mW of the laser passes through, and when turned off, 8  $\mu\text{W}$  of the laser passes through. However, when the Tank circuit is added and the AOM is turned off, only 427 nW of the laser passes through. Taking into account the initialization time, if 8  $\mu\text{W}$  passes through, the initialization time is less than  $10^2 \mu\text{s}$ . With the tank circuit, the initialization time of leakage increases about 20 times to the ms level, providing better spin protection. Alternatively, a similar effect can be achieved using a double pass AOM method [99], as shown in Figure 3.7(c).

We explain the DAQ system. First, the analog output of the DAC at DAQ is connected to the FSM and the Obj. scanner shown in Figure 3.3, which is used to adjust the focusing position at samples. The two analog outputs adjust the lateral XY position by controlling the FSM, whereas another analog output adjusts the vertical Z position by controlling the Obj.-Scanner. This allows for a  $100 \times 100 \times 200 \mu\text{m}^3$  imaging area.

The optical signal part is described. The APD single photon count module (SPCM) used for photon counting outputs a TTL signal (width  $\sim 10$  ns) every time a single photon enters the input fiber port. This output is connected to the counter at the DAQ. We only read the signals that correspond to readout times, differentiating them from photon counts measured during initialization, or dark current ( $\sim 10^2$  cps) based on Johnson noise (thermal or white noise), etc. To differentiate these signals, we use the pulse blaster output, synchronized with the AOM, as a trigger. The counter accumulates the number of TTL pulses from the SPCM.

Figure 3.4(a) shows an example of pulses. There are two pulses (width  $\sim 50$  ns) in the signal section, which are width  $\sim 400$  ns apart in the photon counting connected with DAQ represented the solid red line. In addition, there are two pulses in the reference measurement. The signals read by the counter in the DAQ are differentiated by the pulse blaster trigger. By calculating the difference in the accumulated photon counts for each pulse blaster trigger interval, the results are sampled as signal measurements, garbage measurement, and reference measurements [97].

### 3.3 Scanning probe microscope

Various methods can be used to perform magnetic imaging of samples using NV centers, as shown in Figure 3.8. For example, the simplest method, as shown in Figure 3.8(b), is to place the sample on top of a diamond and measure the near NV centers to get a magnetic field [100]. This method has the advantage of not requiring any diamond fabrications. However, it has the disadvantage that the sample must be suitable for placement on the diamond, such as a nanoparticle. Measurement of each NV center individually is also a disadvantage, making it difficult to get continuous images and requiring interpolation to produce images. As shown in Figure 3.8(c), it is possible to obtain magnetic field information by measuring the NV centers of nanodiamonds sprinkled on a substrate with a sample [101]. This method has the advantage of being able to measure various samples without any additional processing. However, it requires measuring NV centers in different directions each time, and measurement at desired locations is limited. Magnetic field information can be obtained using wide-field-of-view imaging with a diamond containing ensemble NV centers, as shown in Figure 3.8(d) [102, 103]. This method has the advantage of being able to obtain continuous magnetic field imaging and to finish the measurement fast. However, there are limitations to the types of samples that can be measured and the measurement limit is restricted by the optical diffraction limit. As shown in Figure 3.8(a), diamond scanning probe measurements are possible [104]. This measurement method offers the advantages of high spatial resolution, the ability to continuously use the same NV center for measurements, and no destructive effects on the

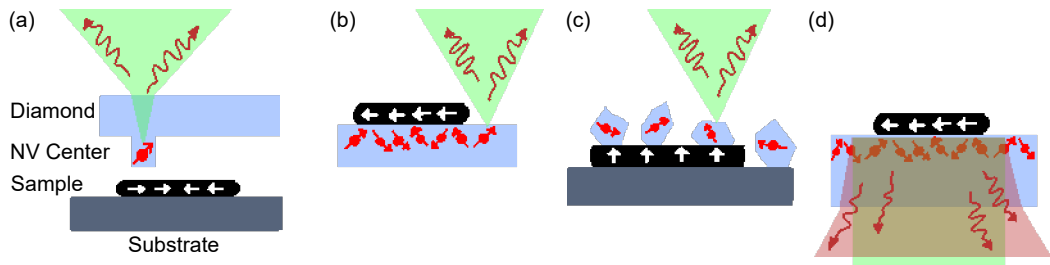


Figure 3.8: NV Imaging methods. (a) Scanning magnetic samples using a diamond tip. (b) Magnetic sample on diamond substrate. (c) Nano-diamonds on magnetic samples. (d) Wide-field of view imaging with diamond NV ensemble.

sample. However, there are disadvantages, such as the need to fabricate the diamond to an optimal pillar structure and the relatively long scanning time.

In this section, the scanning probe microscope with the NV center is explained. There are various scanning probe microscope methods, such as scanning probe microscope, but here we focus on atomic force microscope (AFM). AFM is a microscopy technique for measuring samples using the attractive and repulsive forces between atoms on the sample surface and atoms on the scanning tip. This measurement provides the advantage of achieving nm spatial resolution and even allows for atomic resolution measurements. AFM measurements can be performed using optical methods to measure the cantilever motion, piezo self-resistance methods, or tuning forks (TF) made of materials such as quartz crystal. Since we are already using optical measurements and avoiding optical interference, we employ the tuning forks method.

Continuing with the description of tuning forks, they are made of piezoelectric material, such as quartz. Electrodes are connected to the surface and the end of the tuning forks. When a voltage is applied to the electrodes, a mechanical motion occurs. The resonance frequency of the tuning forks is determined by factors such as their length, width, and thickness dimensions and the material properties of the quartz. Tuning forks with the resonance frequency  $\sim 32$  kHz are commonly used. Their resonance frequency can be read electrically. The mechanical oscillator of the tuning fork can be related to an RLC circuit with the mechanical values of damping constant, mass, and spring constant. These values can be used to calculate

Figure 3.9: NV Scanning method. (a) A fabricated diamond probe. (b) Nano-diamond attached at the end of AFM cantilever. (c) Magnetic samples attached at the end of AFM cantilever. (d) Fabricated diamond pillars and magnetic samples attached at the end of AFM cantilever.

amplitudes. This calculation will be explained after the description of the experimental setup.

Various scanning methods can be used, as shown in Figure 3.9. There are methods like in Figures 3.9(a,b), where the diamond scans the sample, and methods like in Figure 3.9(c,d), where the sample is attached to an AFM cantilever. The advantage of Figures 3.9(a,b) is that there are fewer restrictions for the sample, but the disadvantage is that diamonds need to be fabricated or attached. Furthermore, in Figure 3.9(b) [105], the spin properties of NV may be worse compared to Figure 3.9(a) [106]. Figures 3.9(c,d) have the advantage of being able to use multiple NV centers and the disadvantage of having limited types of samples that can be used. Figure 3.9(d) [107] can obtain better optical properties compared to Figure 3.9(c) [86]. In this dissertation, scanning using fabricated diamond probes is discussed.

The equipment used for scanning setups is described in Table 3.3. The outline of the electronic structures is shown in Figure 3.10. This electronic structure is described here. We

### 3.3. Scanning probe microscope

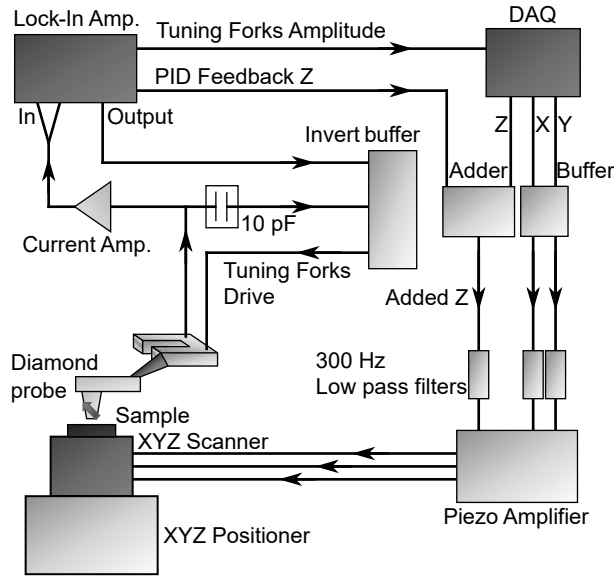


Figure 3.10: Scanning probe microscope electronics. Each components details in Table 3.3.

Components	Description	Vendor	Part No.
Lock-In Amp.	Lock-In Amplifier 500 kHz	Zurich Inst.	MFLI 500 kHz
DAQ	Multifunction Data Acquisition	NI	PXIe-6363
Piezo Amp.	Open-Loop Piezo Controllers	Thorlabs	MDT693B
XYZ Scanner	Piezo-based Scanner, $50 \times 50 \times 24 \mu\text{m}^3$	attocube	ANSxyz100std/LT/HV
Current Amp.	Current Amplifier, Gain $5 \times 10^7 \text{ V/A}$	FEMTO	LCA-100K-50M
XYZ Positioner	Cryo Positioning Stage High Resonance	JPE	Custom ordered CPSHR1-S
XYZ Pos. Controller	Cryo Actuator Driver Module	JPE	CADM

Table 3.3: Tuning forks based scanning probe microscope electronics. This is used to build the scanning probe electronics as seen in the Figure 3.10.

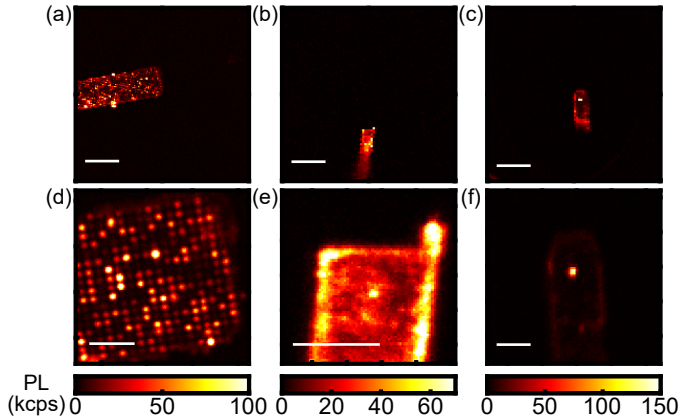


Figure 3.11: Confocal microscope images of diamond scanning probes. (a,d) UCSB probe images. (b,e) QNami probe images. (c,f) QZabre probe images. Scale bars 20  $\mu\text{m}$  for (a-c). Scale bars 5  $\mu\text{m}$  for (d-f).

can consider our system to be divided into two main parts: one is the lock-in amplifier used for driving the TF and readout, and the other is the DAQ that controls the position of the TF. At the start, the DAQ is explained. The DAQ reads the TF amplitude during scanning from lock-in amp. and is used to decide the tip-sample distance and control the position of the tip. The TF amplitude is read through the ADC analog input and the position of the tip is adjusted using the DAC analog output. This analog output is used to control the piezo scanner stage through a piezo amplifier. The XY voltages drive the scanner via a buffer which is based on LT1167 [108] and a 300 Hz low pass filter and piezo amplifier. The 300 Hz low pass filter is built using a passive RC circuit enclosed in a Pomona box. The gain of the piezo amplifier is 7.5. The Z voltage is then passed through the adder and 300 Hz low pass filter to drive the scanner enclosed in Pomona box. Voltage correction is added by a Lock-in PID feedback in the adder which is based on LT1167 and LT1097 [108]. The piezo positioner is driven by high voltage of the positioner controller module connected with usb to the desktop. It is operated using the slip-stick motion [109] of a typical piezo motor. The piezo positioner and piezo scanner parts will be discussed.

Detailed images of the scanning stage are shown in Figure 3.12. The XYZ positioner

### 3.3. Scanning probe microscope

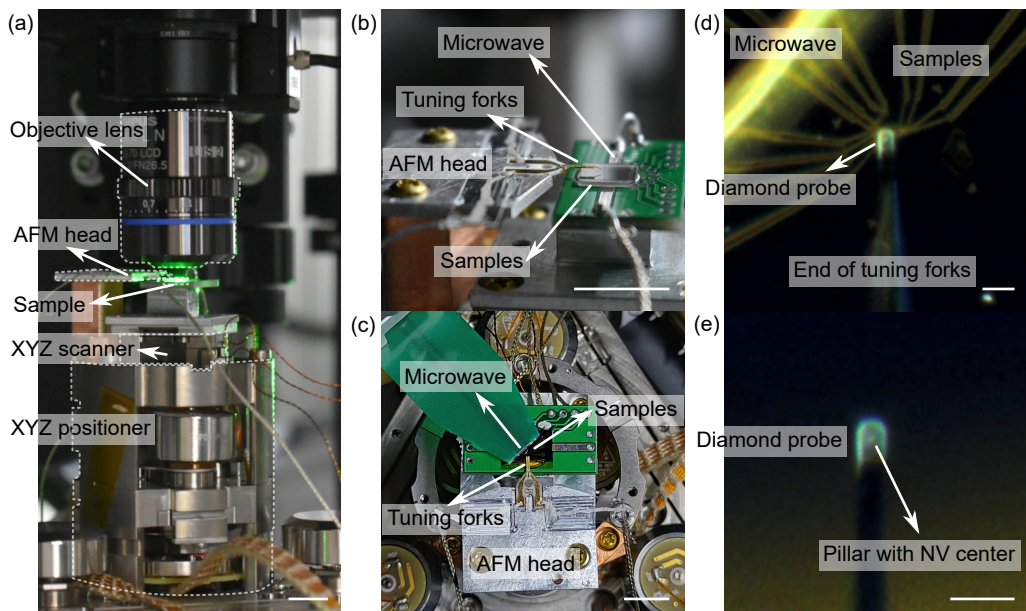


Figure 3.12: (a) Whole side view, and (b) Side view, and (c) Top view photo of scanning systems. Scale bars 1 cm for (a-c). (d) Diamond probe, sample, microwave. (e) Diamond probe and nano pilla on QZabre. Scale bars 10  $\mu\text{m}$  for (d,e).

### Chapter 3. Nanoscale Imaging Experiment Setup

controls coarse movements, which are positioned using three piezo actuators. The home built AFM head is assembled with screws on XYZ positioner. Also, diamond probes are attached to the AFM head and electrically connected to the lock-in amplifier. The scanning probes are from UCSB [40, 110], QNami [111], and QZabre [112, 113] as shown in Figure 3.11. The AFM head is fixed and the positioner is adjusted to control the relative position of the tip and sample. The position is controlled by a combination motion of three piezo knob actuator in  $\pm 0.5$  mm and can be manipulated within approximately  $\lesssim 1 \times 1 \times 1$  mm<sup>3</sup> determined by

$$\begin{pmatrix} \Delta x \\ \Delta y \\ \Delta z \\ \Delta R_x \\ \Delta R_y \\ \Delta R_z \end{pmatrix} = \frac{1}{3\mathcal{R}} \begin{pmatrix} -\hbar\sqrt{3} & 0 & \hbar\sqrt{3} \\ \hbar & -2\hbar & \hbar \\ \mathcal{R} & \mathcal{R} & \mathcal{R} \\ -1 & 2 & -1 \\ -\sqrt{3} & 0 & \sqrt{3} \\ 0 & 0 & 0 \end{pmatrix} \begin{pmatrix} \Delta z_1 \\ \Delta z_2 \\ \Delta z_3 \end{pmatrix} \quad (3.4)$$

, where  $\Delta z_{1,2,3}$  are motions of each piezo knobs, the height of positioner  $\hbar$  is  $\sim 34$  mm, the distance from piezo actuators  $\mathcal{R}$  is 15 mm, and  $\Delta R_{x,y,z}$  are rotations on each axes. For this movement, the angles are coupled, but in practical use it will be a tilt of about  $< 1^\circ$ . The piezo scanner operates at room temperature in the 60 V range with  $50 \times 50 \times 24$   $\mu\text{m}^3$  of movement, and adjusting the output by 1 mV results in 0.4 nm of vertical movement and 6.3 nm of lateral movements calculated by

$$\begin{aligned} \Delta z &= \frac{24 \mu\text{m}}{60 \text{ V}} \times 1 \text{ mV} \approx 0.4 \text{ nm}, \\ \Delta x, \Delta y &= \frac{50 \mu\text{m}}{60 \text{ V}} \times \underbrace{7.5}_{\text{Amplifier}} \times 1 \text{ mV} \approx 6.3 \text{ nm}. \end{aligned} \quad (3.5)$$

Electrical signal part will be explained.

The Lock-in amplifier is a device that measures amplitude and phase robustly against noise. By using it, measurements can be made to suppress  $1/f$  (pink) noise. Output and input signals are mainly used, and the amplitude or PID feedback can be used for the utility.

Figure 3.13: Schematics of tuning forks. (a) Drawing of a structure and electrodes of tuning forks. (b) Equivalent RLC circuit of tuning forks.

The principle of the lock-in amplifier uses a local oscillator of a specific frequency and a modulated output of the same frequency. When reading the input signal, the local oscillator is used for demodulation, and the amplitude and phase are got from the demodulation. For example, the operating principle is simply explained in the Figure 3.10. If the signal coming out of the lock-in amplitude is called voltage output  $V_o(t) = V_o \sin(\omega_o t)$ , the current driving the TF is called  $I_i$ . There is an invert buffer and 10 pF, but these will be explained later. This current  $I_i$  is amplified through a current amplifier and read as  $V_i(t) = V_1 \sin(\omega_o t + \varphi)$  into the lock-in amplifier. The demodulation process is as follows. Multiply an arbitrary input signal  $V_n(t) = V_n \sin(\omega_n t + \varphi)$  and a reference signal  $V_r(t) = V_r \sin(\omega_o t)$  which is the local oscillator. This is calculated by

$$\begin{aligned}
 V(t) &= V_n(t)V_r(t) = V_n V_r \frac{1}{2} (\cos(\omega_o t + \varphi - \omega_n t) - \cos(\omega_o t + \omega_n t + \varphi)) \\
 &\approx \frac{1}{2} V_n V_r \cos(\varphi) \\
 V_{\frac{\pi}{2}}(t) &= V_n(t)V_{r, \frac{\pi}{2}}(t) = V_n V_r \frac{1}{2} (\cos(\omega_o t + \varphi + \frac{\pi}{2} - \omega_n t) - \cos(\omega_o t + \omega_n t + \varphi + \frac{\pi}{2})) \\
 &\approx -\frac{1}{2} V_n V_r \sin(\varphi)
 \end{aligned} \tag{3.6}$$

where  $\omega_n \approx \omega_o$ . If  $\omega_n$  and  $\omega_o$  are similar, the term oscillating at  $\omega_n + \omega_o$  is oscillating fast and removed using a low-pass filter. In this way, only the frequency components matching the reference are measured, and the noise is suppressed by measuring in the frequency reducing  $1/f$  noise. Through this, we can get the amplitude  $V_i$  and the phase  $\varphi$ .

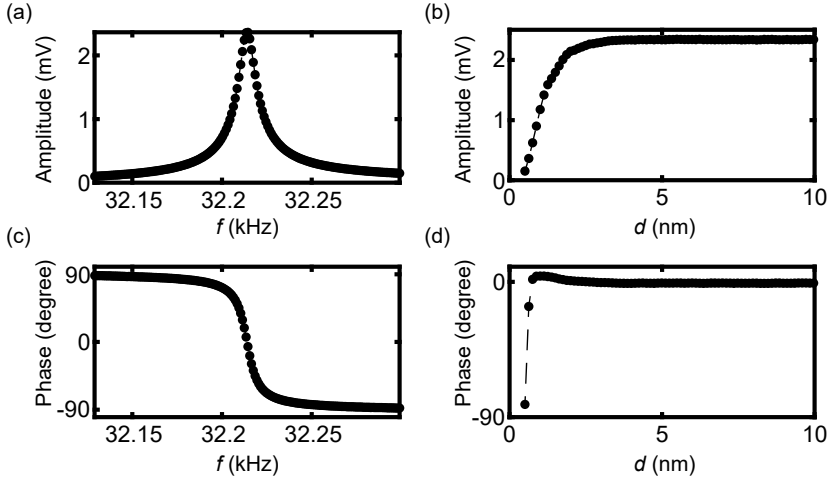


Figure 3.14: Lock-In signal. (a) Amplitude vs. frequency. (b) Amplitude vs. distance. (c) Phase vs. frequency. (d) Phase vs. distance. (e) Comparison distance

The TF mechanism is described with one example what we used. When electric drive occurs, an oscillation of TF is created as shown in Figure 3.13(a). The tuning forks moves in a lateral shear mode. In general, the magnetic field of the sample varies more along the vertical direction, so it is more beneficial to measure the magnetic field by vibrating the diamond probe laterally. The TF have dimensions with length  $\ell \approx 3$  mm, thickness  $t \approx 0.3$  mm, and width  $w \approx 0.37$  mm. An effective mass of TF is defined by  $m_{\text{eff}} = 0.2427\zeta(\ell tw) \approx 0.2$  mg, where density is  $\zeta = 2.65 \times 10^3$  kg/m<sup>3</sup>, and a spring constant is defined by  $k = \frac{1}{4}\mathcal{E}w(\frac{\ell}{t})^3 \approx 7 \times 10^3$  N/m, where Young's modulus is  $\mathcal{E} = 78.7$  GPa [114]. So, its resonance frequency is defined by  $f = \frac{1}{2\pi}\sqrt{\frac{k}{m_{\text{eff}}}} \approx 3 \times 10$  kHz. As shown in Figure 3.13(b), This TF is related with the RLC circuit with a parallel capacitance  $C_e$  caused by electric contacts, and wire connections. The TF resonance curve is transformed asymmetrically because of the parallel capacitance. This parallel capacitance component causes the TF resonance curve to be asymmetric. To compensate for this effect, the invert buffer is used to provide opposite-direction modulation and is connected with 10 pF before the current amplifier [115]. The capacitance 10 pF is enclosed in Pomona box. This invert buffer is based on LT1167, LF356 and Potentiometer [108].

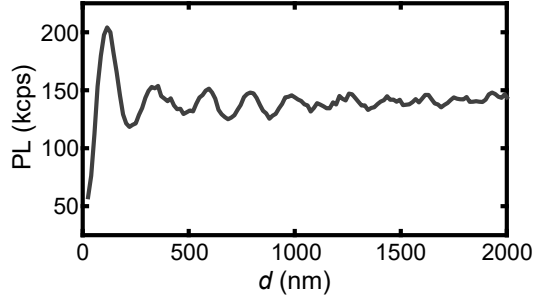


Figure 3.15: PL vs. distance from surface.

So, TF resonance curve for the amplitude and the phase is obtained as shown in Figures 3.14(a,c). In the frequency domain, we can see that it has a resonance of  $\sim 32$  kHz, and its phase shifts 180 deg around the resonance frequency. Also, depending on the tip-sample distance, the amplitude and phase changes rapidly at closer to the sample as shown in Figures 3.14(b,d). For example, if we fix the frequency and move the tip closer to the surface and determine the point where the amplitude changes rapidly, we can measure location of the samples. The diamond pillar is not sharp, so it is difficult to reduce the amplitude to cause the amplitude to change rapidly closer to the sample. This limits our ability to measure distance at the atomic level, so we typically have a deviation of  $\sim 1$  nm. In more distant regions, the distance is estimated through the region where the PL curve is oscillating by reflection from the sample or quenching near the samples surface shown in Figure 3.15.

So there are a couple of ways to check how much this TF is actually moving. We can calculate the amplitude by comparing the mechanical energy dissipation to the driving power [116]. The driving power is defined by  $V_{\text{rms}}I_{\text{rms}}$ , where  $V_{\text{rms}}$  is the driving voltage which is determined at lock-in output, and  $I_{\text{rms}}$  is the driving current which is determined at lock-in input divided by the gain of the current amplifier ( $5 \times 10^7$  V/A). The mechanical dissipation is defined by  $-\frac{2\pi f \hbar a^2}{Q}$ , where the amplitude is  $a$ , and the Q factor is  $Q \sim 2000$  in our cases. The amplitude is calculated by

$$a = \sqrt{\frac{Q V_{\text{rms}} I_{\text{rms}}}{2\pi f \hbar}} \approx 1 \text{ nm} \quad (3.7)$$

### Chapter 3. Nanoscale Imaging Experiment Setup

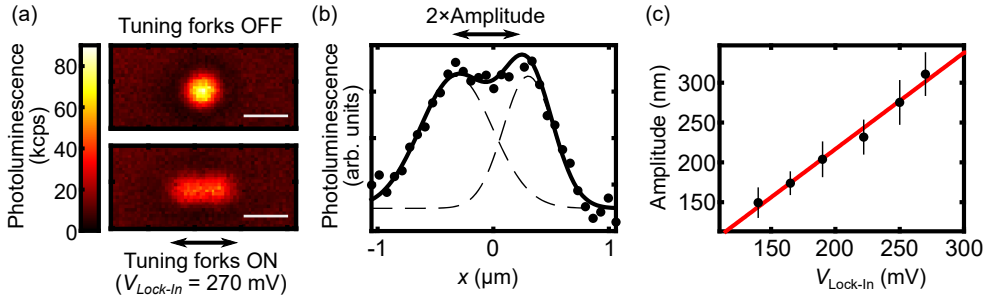


Figure 3.16: Tuning forks amplitude measurement. (a) Optical images of single NV center at diamond probe. Scale bars 1  $\mu\text{m}$ . (b) Line cut of PL image where TF ON. (c) TF Amplitude vs. lock-in input signal.

, where  $V_{\text{output}} \approx 5 \text{ mV}$ , and  $V_{\text{input}} \approx 1 \text{ mV}$ .

The other way is to measure optically and interpolate the results as shown in Figure 3.16. Since the TF frequency is fast enough compared to the timescale of acquiring the confocal image, we will be able to determine from the optical image where the velocity at both ends is zero. An example of this is shown in Figure 3.16(a). The top image shows a single bright spot represented the single NV when the TF is not vibrating. The bottom image shows an image of the NV in the case of mechanical excitation. The NV image looks like a dumbbell, expanding out to the sides. Also, the PL measurement is smaller than when it is at rest because it is not in the same position all the time. We can get a line cut of this image and figure out the amplitude, as shown in Figure 3.16(b). These measurements were repeated for each different lock-in input and interpolated as shown in the Figure 3.16(c). This resulted in a relationship of approximately  $\sim 1 \text{ nm/V}$ , which is roughly similar to the previous calculation Equation 3.7.

The spatial resolution of these measurements is described in the Figure 3.17, where two magnetic field sources are shown. Figure 3.17(a) illustrates two infinite current-carrying wires separated by 100 nm and carrying 10  $\mu\text{A}$ . The NV probe scans at a constant height above them to measure the magnetic field. As the height increases, two factors can be observed. First, the magnitude of the magnetic field decreases. Second, the line width of the magnetic field is broaden. Above 70 nm, it becomes hard to distinguish the magnetic fields

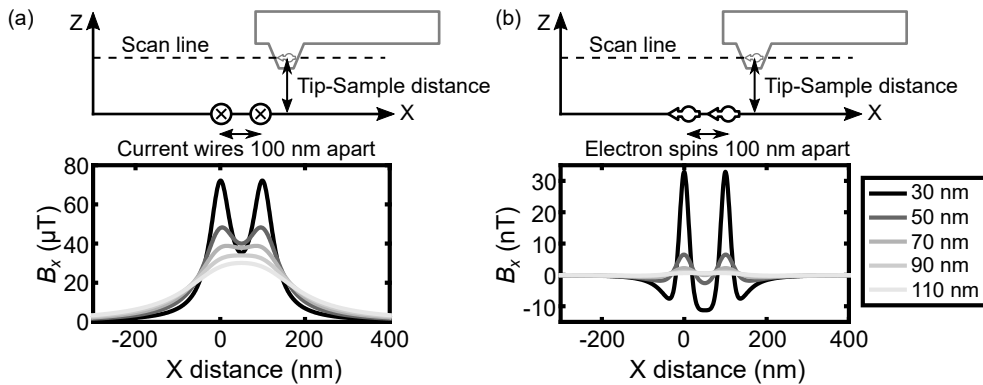


Figure 3.17: The spatial resolution of magnetic field imaging is determined by the distance between the tip and the sample. (a) Magnetic field values along two parallel wires at different heights. (b) Magnetic field values above two electron spins at different heights.

of the two wires.

In Figure 3.17(b), the distance between the two electron spins is 100 nm. The magnetic field of an infinite wire follows  $\sim \frac{1}{r}$  relationship, while the magnetic field of a magnetic dipole follows  $\sim \frac{1}{r^3}$  relationship. As a result, the magnitude of the magnetic field decreases with increasing height. However, the magnetic field peak becomes less diffuse, allowing to be distinguishable at heights of 100 nm. Thus, the spatial resolution is dependent on the distance between the tip (NV) and the sample in both cases, as shown in the Figure 3.17.

### 3.3.1 Imaging method example for various magnetic samples

The methods for actually measuring in scanning. Various measurement methods are used depending on the size of the magnetic field generated by the samples, in order to achieve effective, and fast measurements. For example, when the magnetic field generated by the sample is large and varies greatly in magnitude, the ESR spectrum must be measured over the entire frequency range to find the position of valleys. Alternatively, there are cases where the entire ESR spectrum is not necessary when we want to quickly image the changing pattern or domain of the samples. There are also cases where the magnitude of the magnetic field is similar and the changes are small. Therefore, various measurement methods are

Figure 3.18: Example of ESR spectrum and magnetic field measurement scheme. (a) Drawing of ESR spectrum as a function of microwave frequency. (b) The photoluminescence  $\mathcal{P}(f_0)$  with regard to variations in the magnetic field when the frequency of the microwave is set at  $f_0$ . (c) The difference of PL  $\mathcal{P}(f_1) - \mathcal{P}(f_2)$  with regard to variations in the magnetic field when the frequencies of the microwave are set at  $f_1$  and  $f_2$ . (d) The lock-in PL  $\Delta\mathcal{P}(f)$  spectrum as a function of microwave frequency. In the linear central area, The  $\Delta\mathcal{P}(f)$  measurements at two frequencies can be used to find the frequency where  $\Delta\mathcal{P}(f) = 0$ .

complementarily used.

For example, we can get two valleys through full ESR measurements, and the magnetic field can be measured through their positions. One examples shows in Figure 3.20(a), and Figures 4.3(a,b). The advantage of this measurement is that it can directly obtain magnetic field from the ESR measurement results and quantitatively measure the magnitude of the magnetic field. However, the disadvantage is that the entire spectrum must be measured while performing a frequency sweep. Consequently, the number of frequency positions measured is large, resulting in a longer measurement time.

Figure 3.18(a) shows an illustration representing a valley of the ESR spectrum, and this illustration shows an example to explain other measurement methods. For example, assume that the ESR spectrum in applying a bias field is as shown in Figure 3.18(a). If we fix the microwave frequency at  $f_0$  and measure the PL as a function of the magnetic field variation, the result shows Figure 3.18(b). In this case, the PL is dark at the  $\Delta B = 0$  position and bright at the  $\Delta B \neq 0$  positions. By fixing the frequency and performing normalized PL measurements where microwave ON/OFF, a scanning NV image is obtained, as shown in Figure 3.19. This image shows the contour of the magnetic field related to domains in magnetic films. Alter-

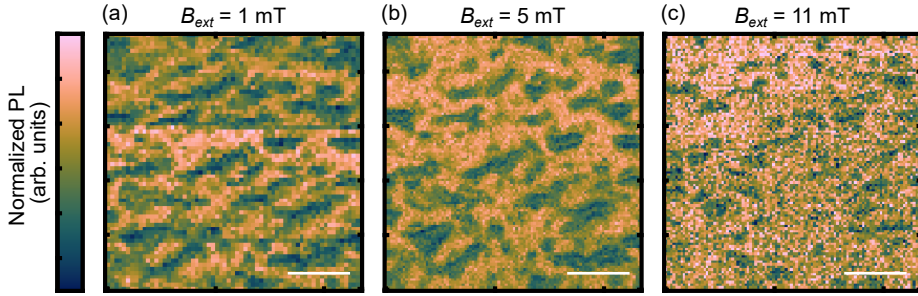


Figure 3.19: Examples for contour image of the magnetic skyrmion sample. This sample is made with Ta(1.5)/Pt(2)/Co(0.3-1.5)/Pt(5)/Ta(2) on MgO(001) Substrate. As the external magnetic field increases from (a) to (c), the magnetic image changes from zebra-like stripes to bubbles-like patterns forming the skyrmions. Scale bars 5  $\mu\text{m}$ .

natively, by using a different microwave frequency, a contour corresponding to a specific magnetic field can be obtained. Also, these examples are compared with a full ESR image shown in Figure 3.20(a) and contour images shown in Figures 3.20(c-g). This measurement offers the advantage of simple and rapid imaging of samples and makes it easy to check for domain changes. However, this imaging is that it provides only partial information about the magnetic field. Furthermore, the range of magnetic fields must be larger than the frequency corresponding to the ESR linewidth. In cases where the magnetic field variation is small, it may be challenging to observe clear contours. For example, in Figure 3.18(b), if the changes in the sample are greater than 0.3 mT, then the contour measurement becomes meaningful.

Another method, similar to the contour imaging discussed earlier, involves using dual microwave frequencies. By measuring the PL  $\mathcal{P}(f_1)$  and  $\mathcal{P}(f_2)$  at frequencies  $f_1$  and  $f_2$  in Figure 3.18(a) and subtracting  $\mathcal{P}(f_1) - \mathcal{P}(f_2)$  values, the result shown in Figure 3.18(c) can be obtained. In this case, the PL is linear to changes in magnetic field in the  $\Delta B \sim \pm 2.5$  mT range. This PL can be used to convert the magnetic field. An example of this measurement is shown in Figure 3.20(b), Figure 6.2(c), and Figure 6.3(g-i). This method allows for some degree of quantitative measurement and is faster than a full ESR measurement. However, it has the disadvantage of having a fixed dynamic range, and it is hard to use in magnetic field values larger than the range.

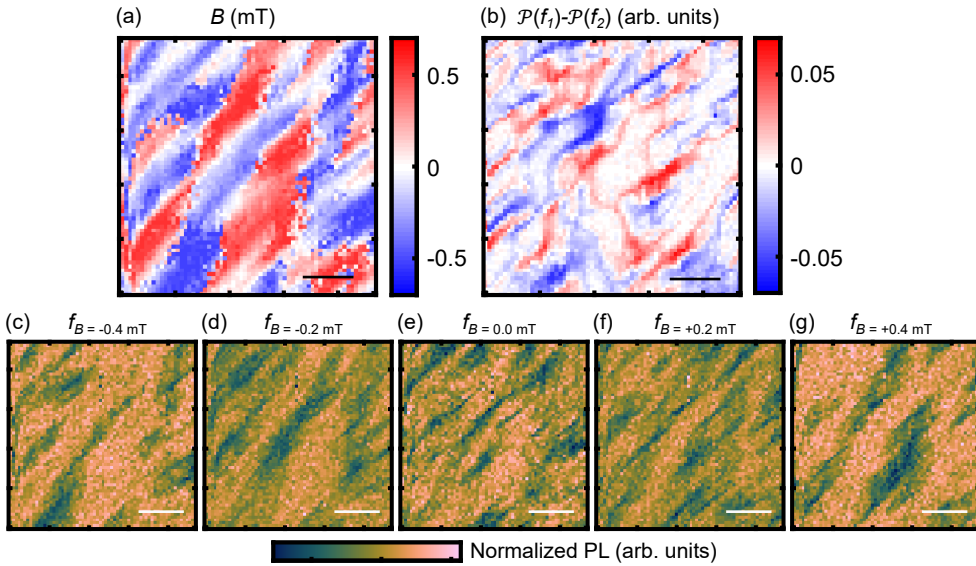


Figure 3.20: Various magnetic imaging of ferromagnetic film with IrMn(5). (a) Full ESR measurement image. (b) Dual microwave frequency image. (c-g) Contour image with several microwave frequency for picked magnetic field variations. Scale bars 500 nm.

Another method is the Frequency Modulation (FM) lock-in measurement technique. This approach is similar to the lock-in measurement. It employs FM modulation of the microwave generator, centering the frequency  $f$  and modulating the frequency within a range of  $\Delta f$ , such as  $\sim 100$  kHz. In this process, the measured PL is demodulated, resulting in a value referred to as  $\Delta\mathcal{P}(f)$  shown in Figure 3.18(d). By measuring  $\Delta\mathcal{P}(f)$  near  $\Delta B = 0$  at two points and determining the x-intercept of the frequency domain between these two points, the precise location of the valley can be determined. The advantage of this method is that it allows quantitative measurement by determining the ESR valley position. Additionally, the use of the lock-in technique enables robust and precise measurements in noisy situations. However, this method includes a limited dynamic range and the requirement of a frequency modulation function. An example of this measurement can be seen in Figures 5.2(b,c), Figure 5.3(c), Figure 5.7(a), and Figure 5.8(a).

### 3.4 Experiment in cryostat

These NV center experiments can be performed in a cold environment. Vacuum levels and temperature and thermal transfer should be discussed for experimentation in cryogenic conditions. Vacuum levels and a pump to provide a vacuum environment are discussed. There are several units to present vacuum level. Typically, atmospheric pressure is described by 1 atm which is same with

$$1 \text{ atm} = 1.013 \times 10^5 \text{ Pa} = 1013 \text{ mbar} = 14.7 \text{ psi} = 760 \text{ mmHg} = 760 \text{ Torr}. \quad (3.8)$$

In this dissertation, Torr is used. The degree of vacuum and vacuum levels are divided by

• Atmospheric pressure	760 Torr	101 kPa
• Low vacuum	$\sim 10^{-3}$ Torr	$\sim 0.1$ Pa
• High vacuum (HV)	$10^{-5} \sim 10^{-3}$ Torr	1 $\sim$ 100 mPa
• Ultra high vacuum (UHV)	$10^{-11} \sim 10^{-10}$ Torr	1 $\sim$ 10 nPa
• Extreme high vacuum	$\sim 10^{-13}$ Torr	$\sim 10^{-11}$ Pa
• Outer space	$10^{-17} \sim 10^{-9}$ Torr	$10^{-15} \sim 10^{-7}$ Torr.

In physically, the vacuum is comparable to the mean free path of a gas molecule and the volume of a vacuum chamber. An appropriately high vacuum must be created to suppress the condensation of gases such as vapor in the experiment [117]. These levels determine the type of vacuum pump. For example, at low vacuum levels, a rotary pump is used. At higher vacuum levels, a turbomolecular pump or an ion pump may be used. At low temperatures, a cryo pump may be used for high vacuum. In addition to pumps, clean materials are required. Dirty elements cause surface evaporation and make it difficult to produce a vacuum. Ultra-sonic cleaning is used to remove an oil or matter and chemical cleaning with citric acids is used to remove metal oxidation.

### Chapter 3. Nanoscale Imaging Experiment Setup

Thermal transfer is explained to present how to make the temperature cold and a cooling power of the cryostat. There are three types of thermal transfer such as ‘Conduction’, ‘Convection’, and ‘Radiation’ [118]. We are talking about heat transfer by conduction. The temperature drops through the base plate connected to a cryocooler. Methods to prevent heat transfer by radiation from room temperature are discussed. In the case of high vacuum, the heat transfer by convection is small enough, but several methods for calculating it are discussed.

For conduction, heat transfer is described in solid by

$$P = \kappa A \frac{dT}{dx} \quad (3.9)$$

, where  $\kappa$  is thermal conductivity of the materials,  $A$  is area and  $x$  is distance between objects. This means that the larger the cross-section and the shorter the length, the more heat it transfers. The heat of the base plate is transferred to the cryocooler and the base plate is cooled. For the heat sink from a sample to the base plate, a ribbon made of oxygen-free high-conductivity copper is used as shown in Figure 3.21. In addition, electrical connection can inject heat  $> 10$  mW from the housing to the samples. Phosphorus bronze thin wires are used to prevent conduction. For example, the thermal conductivities of copper are  $k = 300 \text{ W}/(\text{m K})|_{T=4\text{K}} = 700 \text{ W}/(\text{m K})|_{T=10\text{K}}$ , and conductivities of phosphorus bronze are  $k = 1.6 \text{ W}/(\text{m K})|_{T=4\text{K}} = 4.6 \text{ W}/(\text{m K})|_{T=10\text{K}}$ . In the case of electric wiring as shown in Figure 3.21, the phosphorus bronze wire with 36 AWG is used to avoid transfer heat from housing shield (at 30 K) which is calculated by

$$P \simeq 4.6 \text{ W}/(\text{m K}) \times (2.5 \times 10^{-8} \text{ m}^2) \times \frac{30 \text{ K} - 4 \text{ K}}{0.1 \text{ m}} = 0.46 \text{ mW}. \quad (3.10)$$

In the case of heat sink ribbons, the copper ribbon with the width of 2 cm, and the thickness of 0.2 mm connected between base plate and samples is considered by conduction equation

$$P \simeq 300 \text{ W}/(\text{m K}) \times (4 \times 10^{-6} \text{ m}^2) \times \frac{10 \text{ K} - 4 \text{ K}}{0.1 \text{ m}} = 72 \text{ mW}. \quad (3.11)$$

For better conductance, surface polishing or acid cleaning are performed on ribbons, and a little N grease is spread for better thermal contact on surface.

For radiation, black-body radiation power is calculated by

$$P = A\varepsilon\sigma T^4$$

$$P_{1,2} = A \frac{\varepsilon_1\varepsilon_2}{\varepsilon_1 + \varepsilon_2 - \varepsilon_1\varepsilon_2} \sigma (T_1^4 - T_2^4) \quad (3.12)$$

, where  $P$  is a radiation power,  $P_{1,2}$  is the power exchange between matters, the Stefan-Boltzmann constants is  $\sigma = 5.67 \times 10^{-8} \text{ W}/(\text{m}^2 \text{ K}^4)$ , an emissivity is  $\varepsilon$ , and  $A$  is the area. Radiation shields (at 30 K) are used to prevent thermal radiation heating between the base plate (at 4 K) and the outer housing (at 300 K). The power of heat  $\sim 10 \text{ mW}$  is radiated through a circle  $\sim \text{cm}$  of diameter between 4 K and 300 K.

For convection, there are two types of thermal transfer such as the viscous regime and molecular regime. At first, viscous regime is discussed in high gas pressure, where the mean free path of the gas is larger than the size between two objects. This power is described by

$$P = \kappa A \frac{dT}{dx} \quad (3.13)$$

, where  $\kappa = \kappa(T)$  is the thermal conductivity independent of pressure and  $\frac{dT}{dx}$  is the temperature difference between the object. At second, molecular regime is discussed in low gas pressure, where the mean free path of gas is smaller than the size between two objects. This power is described by Kennard's law

$$P = A\alpha \left( \frac{\gamma + 1}{\gamma - 1} \right) \sqrt{\frac{\mathcal{R}}{8\pi M}} \frac{T_2 - T_1}{\sqrt{T}} \mathcal{P} \quad (3.14)$$

, where accommodation coefficient  $\alpha$  depends on the gas species,  $\gamma$  is the heat capacity ratio,  $\mathcal{P}$  is the pressure of the gases,  $M$  is Molar mass of gas (unit in kg here),  $\mathcal{R}$  is the gas constant. Power of this convection is smaller than  $< 1 \text{ mW}$  in typical cryostat conditions.

So, NV experiment in low temperature requires the cryostat supporting high vacuum,

### Chapter 3. Nanoscale Imaging Experiment Setup

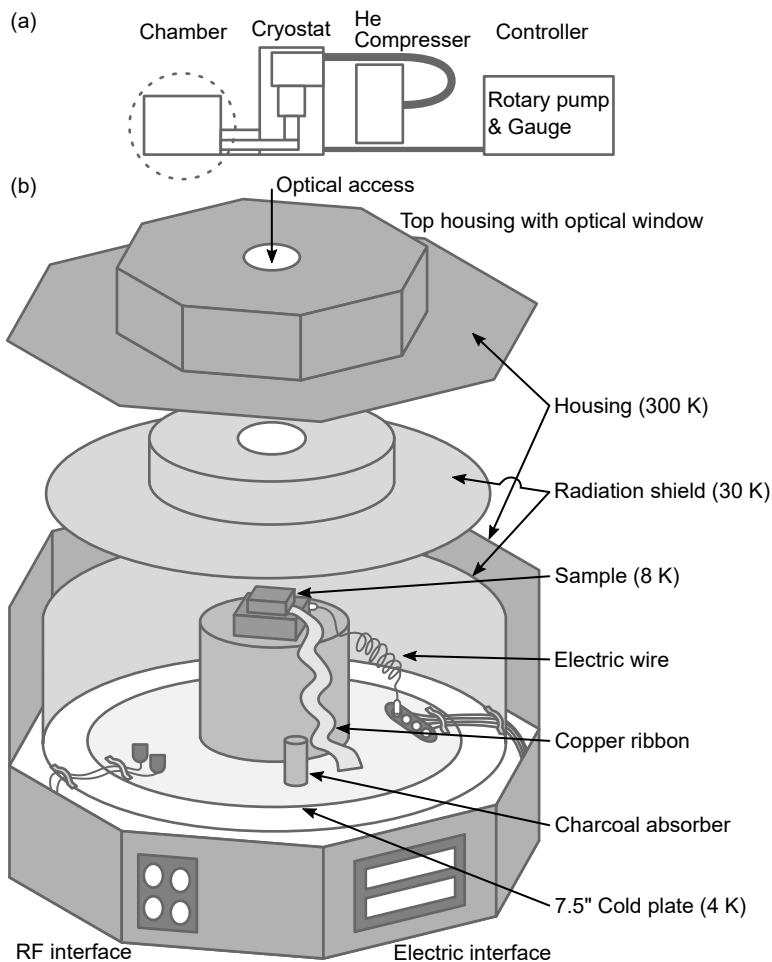


Figure 3.21: (a) A block diagram of an optical cryostat. (b) Schematic of experiments in the cryostat chamber. The radiation shield to prevent radiation is kept at 30 K, which is the temperature of the first stage of the cryocooler, to prevent radiation heating at room temperature. The upper part of the radiation shield has a hole for optical access through which most of the radiation heat is transferred. Electronics pass through the radiation shield, which inhibits heat transfer through conduction.

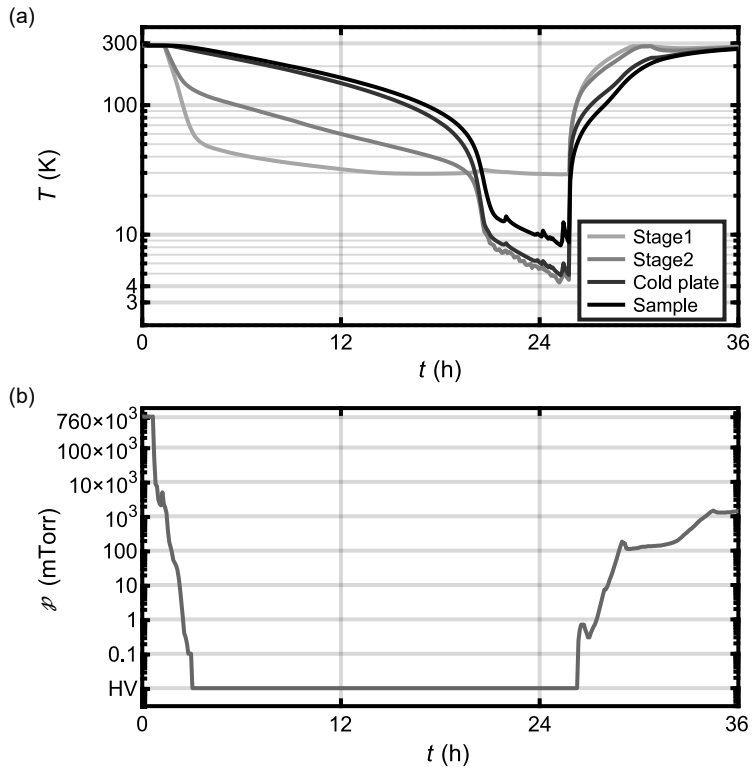


Figure 3.22: Temperature and vacuum data were measured during the 36-hour cooling process. (a) Temperature data. Due to the presence of samples and experimental equipment, the cooling time is several hours longer. Stages 1 and 2 are the temperature of the pulse-tube of the cryostat GM cryocooler. The temperature of the radiation shield is equal to the temperature of Stage 1. It is cooled to  $\sim 30$  K first and maintained at that temperature. The temperature of the cold plate drops to  $\sim 4$  K. The temperature of the sample drops to  $\sim 8$  K. The sample is close to the upper window of the chamber and receives a lot of heat transfer  $> 10$  mW through radiation from the outside, so its temperature does not drop further. (b) Pressure data. A vacuum of  $< 1$  Torr is created using a rotary pump before starting cooling. During the cooling process, a high vacuum is achieved through a decrease in temperature and a cryopump.

### Chapter 3. Nanoscale Imaging Experiment Setup

cryogenic temperature, and an optical access. The s200 with custom hat design (Montana instruments) is used for the optical cryostat as shown in Figure 3.21. It provides a cooling power 50 mW at 4 K, a high vacuum condition  $< 10^{-6}$  Torr, a low vibration  $< 10$  nm, and cryogen-free experiments. In this cryostat, the rotary pump is used to achieve low vacuum level. Also, a turbo pump can be used in addition to that. After a low vacuum level, cryo pumps such as a charcoal column are used under the cooling condition to provide high vacuum conditions. In this cryostat, a Gifford-McMahon cryocooler is used here. This cryocooler uses a helium compressed in a compressor and expanded by a pump in the cryohead to take away heat and cool the object. This cryocooler cooling power is temperature dependent; as the temperature decreases, it decreases its cooling power. Thus, we can decrease the temperature until thermal equilibrium is reached. Therefore, at approximately  $3 \sim 4$  K, the cryocooler output is  $\sim 50$  mW, which is equal to  $\sim 50$  mW of heat transfer by radiation, and the temperature is maintained. In addition, the  $\sim 10$  mW of heat is generated during the experiment using optics and microwaves. In this situation, the cooler can provide higher cooling power at higher temperatures, so at higher temperatures, the sum of the heat generated within the device and the heat received from the outside balances the cooling power at higher temperature  $\sim 100 \text{ mW}|_{T=10 \text{ K}}$ . So the experiment can be performed at  $8 \sim 10$  K shown in Figure 3.22.

In this chapter, we described the NV center experiments and how to make measurements with them. In the following chapter, we present the results of our measurements.

## Chapter 4

# Magnetic Nanowire

From spintronics to recent biomedical applications, ferromagnetic nanowires attract growing interest due to their potential applications in nanotechnology, such as magnetic data storage, logic devices, sensors and actuators [119–127]. In these applications, it is crucial to realize precise control over time-varying magnetic properties such as domain wall motion or locomotion of nanowire itself. In terms of the dynamical control, ferromagnetic nanowires possess unique advantages owing to their combined geometrical properties of high aspect ratio and cylindrical symmetry [124–131]. In spintronics applications, for instance, uniform and stable domain wall motion is possible [128–130], and the Walker breakdown problem can be surpassed by using ferromagnetic nanowires [131]. On the other hand, large magnetic shape anisotropy results in enhanced magnetic force and torque when an external magnetic field is applied, which allows for improved locomotion of nanowires [124]. In this regard, ferromagnetic nanowires can act as untethered mechanical robots whose motion can be wirelessly maneuvered by means of external magnetic fields. The motion capability of ferromagnetic nanowires makes them promising biomedical platforms such as drug delivery nanocarriers. For instance, the nanoscale machines driven into target biological systems can deliver medications, actuate force/heat and probe local change within the systems [125–127].

Despite the unique advantages of magnetic nanowires, monitoring and tracking their dynamics in fluids remains challenging as it requires precise measurement with high magnetic

## Chapter 4. Magnetic Nanowire

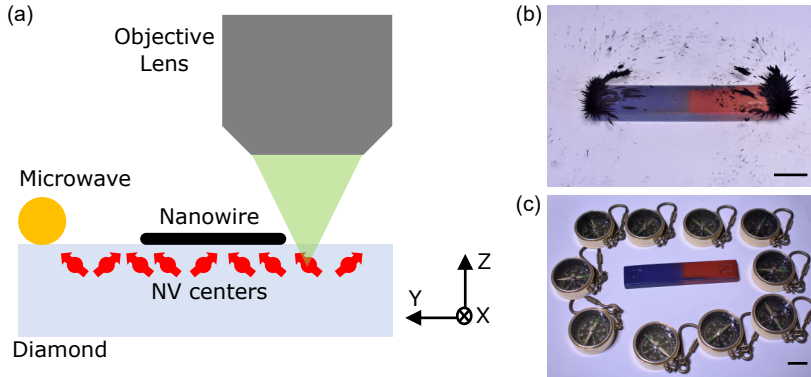


Figure 4.1: (a) Schematics of magnetic field imaging of single nanowire. (b) Bar magnet and iron powders. (c) Bar magnet and compasses. Scale bars 2 cm.

field sensitivity, high spatial resolution, and stable operations in liquid environment. While various sensitive magnetic measurements have been evaluated for magnetic imaging, satisfying all the conditions simultaneously is a demanding task. For instance, magneto-optical Kerr effect microscopy, an optical imaging technique with magnetic contrast, provides relatively fast imaging speed and may be applied to image samples in aqueous solutions [132–134]. However, it is based on optical detection making it hard to monitor the motion of nanowire when it is located inside opaque biological cells or tissues. In contrast, magnetic force microscopy (MFM) is advantageous with regards to this issue since MFM measures magnetic stray fields, which can penetrate biological samples more easily than light [135–137]. However, measuring fast changing magnetic fields while operating in solution is difficult for MFM since it is a force sensitive scanning probe technique.

Recently a novel magnetic sensor based on nitrogen-vacancy (NV) color centers in diamond has been introduced and successfully demonstrated magnetic sensing and imaging of various biological samples [56, 58, 138–140]. NV center is an atomic-scale defect in diamond whose spin states sensitively respond to small changes in magnetic field via Zeeman effect. When negatively charged, the NV center exhibits a spin triplet configuration in the ground state [30]. In the presence of a magnetic field, the NV center's spin Hamiltonian can be written as  $\hat{H}/h = D_0 \hat{S}_z^2 + \gamma_e \vec{B} \cdot \vec{S} + \vec{S} \cdot \mathbf{A}_N \cdot \vec{I}$ , where  $D_0 = 2.87$  GHz is the crystal-field

splitting,  $\gamma_e = 28 \text{ MHz/mT}$  is the gyromagnetic ratio of the NV electronic spin (i.e.  $S = 1$ ),  $\vec{B}$  is a vector magnetic field, and  $A_N$  is the hyperfine coupling to the nitrogen nucleus spin (e.g.  $I = 1$  for  $^{14}\text{N}$ ). The second term in the Hamiltonian corresponds to the Zeeman effect which splits the  $|m_s = \pm 1\rangle$  spin states by an amount proportional to the magnetic field along the NV's quantization axis. The change in the spin states can be optically read out (optically detected magnetic resonance; ODMR), and thus magnetic information can be recorded.

In this way, the NV center can detect magnetic stray fields from biological samples with high spatial resolution and field sensitivity. The magnetic field sensitivity is in the order of  $\text{nT/Hz}^{1/2}$  for a single NV center [34] and can be smaller than  $\text{pT/Hz}^{1/2}$  for NV ensembles [43]. Furthermore, the host diamond crystal is non-toxic and biocompatible suitable for biomedical research [30]. NV centers can also be operated in liquid environment and have potentials to monitor ferromagnetic nanowires even inside biological samples. Therefore, these unique properties make the diamond NV center as an appealing candidate for nanoscale magnetic sensors for biomedical applications.

Here, we demonstrate magnetic imaging of individual ferromagnetic nanowires by measuring magnetic stray fields around the wire with diamond NV centers. The experiment is conducted in dry and ambient condition to test NV center's capability of sensing magnetic fields from the nanowire. We locate a single Co nanowire on a diamond plate where multiple NV centers are closely located underneath the surface. NV centers surrounding a nanowire detect static magnetic field generated from the wire whose strength depends on the relative separation between the nanowire and the NV center. The magnitude of magnetic field is extracted from the amount of Zeeman splitting observed in ODMR signal during the NV measurement. The obtained image shows a good agreement with the simulation result of magnetic field. We also demonstrate improved sensing of DC magnetic field with Ramsey measurement. This work represents an important step toward biomedical sensing devices capable of probing and tracking the dynamics of ferromagnetic nanowires.

## 4.1 Ferromagnetic nanowires and diamond NV centers

Co nanowires are synthesized by means of template-assisted electrodeposition. The electrolyte consists of  $120 \text{ g l}^{-1}$  of cobalt (II) sulfate hexahydrate ( $\text{CoSO}_4 \cdot 6\text{H}_2\text{O}$ ) and  $45 \text{ g l}^{-1}$  of boric acid ( $\text{H}_3\text{BO}_3$ ). The pH of the electrolyte was  $\text{pH} = 5.0$  and it was operated at room temperature. Nanoporous templates of anodic aluminum oxide (AAO) (Whatman Co.) with a pore size of  $200 \text{ nm}$  were used.  $200 \text{ nm}$  of a thick Au layer is thermally evaporated on one side of the AAO template to serve as a working electrode. A Pt sheet is used as a counter electrode. Co nanowires are electrochemically grown using a current density of  $-5 \text{ mA cm}^{-2}$  for 3 h. After the deposition, the membrane is chemically etched away in  $5 \text{ M}$  sodium hydroxide (NaOH) solution for 1 h. The nanowires are rinsed with DI water several times to remove aluminum oxide residuals.

The nanowires are characterized using a scanning electron microscopy (SEM). An SEM specimen is prepared by dispersing the nanowires aqueous suspension on a Si wafer ( $1 \text{ cm} \times 1 \text{ cm}$ ). After drying the suspension at room temperature, an SEM image is acquired using a secondary electron detector in Zeiss ULTRA 55.

Diamond NV centers are formed by implanting nitrogen into an electronic grade single crystal diamond plate (Element six, size  $2 \times 2 \times 0.5 \text{ mm}^3$ ) grown by a chemical vapor deposition.  $^{14}\text{N}$  implantation with a dosage of  $5 \times 10^{11} \text{ ions cm}^{-2}$  at an energy of  $15 \text{ keV}$  with angled  $7^\circ$  preventing ion channeling generates NV centers at the depth of about  $30 \text{ nm}$ . The sample is further annealed at  $850^\circ \text{C}$  for 2 h inside a tube furnace with a flow of  $200 \text{ cc Ar}$  gas.

## 4.2 Experimental setup and ODMR measurement

Experiments are carried out at room temperature and in an ambient condition. A home-built confocal microscope is used to detect the NV center's PL signal. The NV center is excited with a diode laser at  $532 \text{ nm}$  and emits broad band photons of  $600 - 800 \text{ nm}$ , which can be detected by an avalanche photodiode. Typical laser power used for the measurement is in the range of several hundreds of  $\mu\text{W}$  to  $1 \text{ mW}$ . Microwave photons around  $2.87 \text{ GHz}$  are applied to the diamond with a gold wire. While the laser optically pumps and initializes

the NV center into the  $|m_s = 0\rangle$  state, the microwave photons manipulate transitions between the  $|m_s = 0\rangle$  and  $|m_s = \pm 1\rangle$  spin states. Neodymium permanent magnets are used to generate a static magnetic field-of 1.5 mT to lift the ground state spin degeneracy. We carefully align the magnets along the direction of the NV's quantization axis (i.e. [111] in this paper) to isolate the NV centers of this orientation from the NV centers of other crystal axes, and to minimize the field component perpendicular to the NV axis.

Continuous-wave ODMR measurements are conducted by recording the PL signal as a function of microwave frequencies. A reduction in the signal about  $\sim 10\%$  occurs at the spin transition frequencies and the amount of splitting between the transitions is proportional to the magnetic field along the NV axis. For pulsed measurements, such as Ramsey sequences, the laser and microwave photons are gated with an acousto-optic modulator and a RF switch respectively.

### 4.3 Magnetic field simulation

We conduct micromagnetic simulations with the object oriented micromagnetic framework (OOMMF) [141], open source software commonly used to compute magnetization and stray field distributions of magnetic samples. We simulate static magnetic field around a single Co nanowire with the following parameters: magnetization  $M = 1.4 \times 10^5 \text{ A m}^{-1}$ , wire length  $\ell = 12 \mu\text{m}$ , wire diameter  $\mathcal{D} = 300 \text{ nm}$ , and cell size  $2 \times 2 \times 5 \text{ nm}^3$ . The size of the nanowire is determined from SEM image. The magnetization value is determined from the saturation magnetization,  $M_s$  values in references, i.e.  $M_s \sim 1.4 \times 10^6 \text{ A m}^{-1}$  [142, 143] as well as from our own magnetic hysteresis measurements on the nanowire arrays ( $M \sim 5 \times 10^5 \text{ A m}^{-1}$ ). The external magnetic field used in the ODMR experiment is approximately 5% of the magnetic field for the saturation magnetization. To obtain the magnetization value, we consider this ratio and adjust the value further within an order of magnitude in order to match the simulation results to the experimental data. Based on the OOMMF results, we calculate the magnetic field component along the NV axis since it is what we measure from the ODMR measurement.

## 4.4 Magnetic field imaging in confocal optics

Figure 4.1(a) shows schematics of the confocal setup and ODMR measurement. A single Co nanowire on a diamond plate generates a local magnetic field whose distribution is detected by a group of NV centers located at various distances from the wire as shown in Figure 4.1(a). The NV centers serve as the iron powders or compasses in Figure 4.1(b,c). The direction and magnitude of the magnetic field can be determined from Zeeman splitting in the ODMR spectrum. The  $|m_s = 0\rangle$  spin level is split from the degenerated  $|m_s = \pm 1\rangle$  states by  $D_0$  at room temperature. The degenerated  $|m_s = \pm 1\rangle$  states are further split upon applied magnetic field along the NV axis. The Zeeman splitting is manifested by two resonance dips in the ODMR spectrum whose separation in frequency is given by  $\Delta f = 2\gamma_e |B_{\text{NV}}|$ , where  $B_{\text{NV}}$  is the magnetic field parallel to the NV axis as shown in Figure 2.1. While the field magnitude is obtained from the amount of splitting, the field direction can be determined from the relative change in the splitting with respect to the external field from the permanent magnets. If the magnetic field from the nanowire aligns as the same (opposite) direction as the field from the magnets, for instance, the Zeeman splitting will increase (decrease).

For the quantitative analysis of magnetic field distribution, we compare measured data with the OOMMF simulation results. Figures 4.2(a,b) show typical SEM and confocal images of a single Co nanowire, respectively. Bright spots visible in the confocal image correspond to the NV centers while the Co nanowire appears dark as it blocks PL from underneath NVs. The wire's length and orientation in the image are used for the simulation in Figure 4.2(c). We use the saturation magnetization value from the magnetic hysteresis loop shown in the inset of Figure 4.2(a), obtained from a vibrating sample magnetometer measurement on nanowire arrays. When an external magnetic field is applied parallel to the wire long axis, the nanowire generates a magnetic field emanating from the wire's upper end and enters toward the lower end, as dictated by the arrows in Figure 4.2(c). The arrow length is proportional to the field strength which becomes larger near the ends.

Total 92 NV centers around the nanowire are used for the measurement, marked as circles in Figure 4.3(a). Their colors denote the measured  $B_{\text{NV}}$  values. There are four different crystal orientations possible for NV center i.e.  $[\bar{1}\bar{1}\bar{1}]$ ,  $[1\bar{1}\bar{1}]$ ,  $[111]$ , and  $[\bar{1}\bar{1}1]$ . Since NV center detects magnetic field component parallel to its crystal axis,  $B_{\text{NV}}$  values vary depending on

#### 4.4. Magnetic field imaging in confocal optics

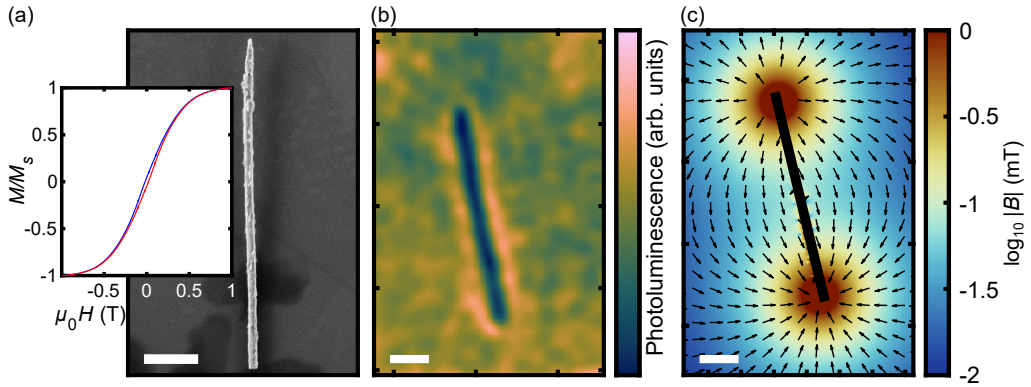


Figure 4.2: Magnetic properties of a single Co nanowire. (a) An SEM image of a single Co nanowire. Scalebar,  $2 \mu\text{m}$ . The magnetic hysteresis loop obtained from nanowire arrays (inset) confirms the soft ferromagnetic property of the Co nanowire. The saturation magnetization of the arrays,  $M_s$ , is  $\sim 5 \times 10^5 \text{ A m}^{-1}$ . (b) Confocal microscope image of a single Co nanowire on a diamond plate. The nanowire appears as a dark rod. The bright spots are NV centers. Scalebar,  $2 \mu\text{m}$ . (c) An OOMMF simulation of the magnetic field around the wire. A magnetization value of  $M = 1.4 \times 10^5 \text{ A/m}$  is used for the simulation. Field strength is indicated by color while field direction is denoted by the arrows. Scale bar,  $2 \mu\text{m}$ .

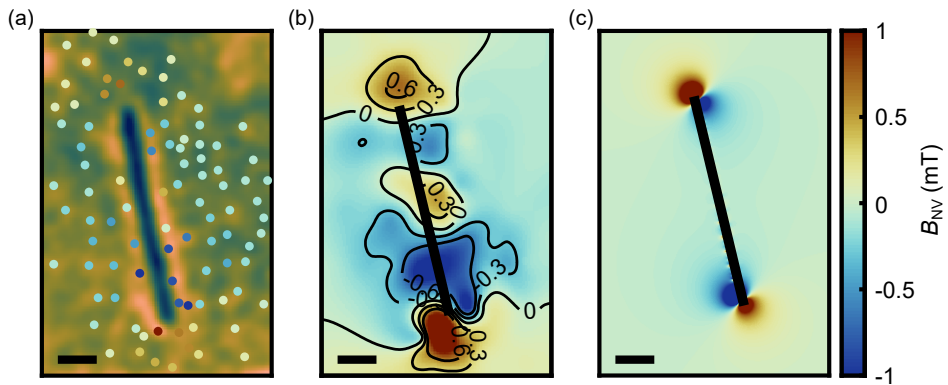


Figure 4.3: Magnetic imaging of a single Co nanowire. (a) 92 NV centers of  $[\bar{1}\bar{1}\bar{1}]$  crystal orientation are used to image magnetic stray field around the nanowire. Circles denote the NV centers and color represents  $B_{NV}$ . (b) For the purpose of smooth and continuous field display, the data in (a) are reconstructed by a biharmonic spline interpolation method. For clarity, constant field contour lines are added. (c) Simulated magnetic field along the  $[\bar{1}\bar{1}\bar{1}]$  direction. The results in Figure 4.2(c) are converted into the field component along the NV axis. Dipole-like patterns at the nanowire's tips are well visible both in (b) and (c). All scale bars, 2  $\mu\text{m}$ .

which NVs are used. In this measurement, we choose 92 NV centers with the same crystal axis of [111] by carefully aligning the permanent magnets along this direction and obtain  $B_{\text{NV}}$  value from one NV center at a time. The results are plotted in Figure 4.3(a) showing the distribution of magnetic field around the nanowire with the minimum field strength of  $\sim 0.1$  mT. However, the image looks quite sparse, mainly due to the low NV density and random locations of the [111] NVs. By using a biharmonic spline interpolation method, we reconstruct the data and obtain a smooth continuous magnetic field map shown in Figure 4.3(b). The image displays that the measured  $B_{\text{NV}}$  becomes stronger near the ends of the nanowire, but its sign gets changed from positive to negative or vice versa. It is because NV center can measure not only the magnitude but also the direction of magnetic fields. This is clearly seen in Figure 4.3(c) which is the calculated magnetic field along the  $[\bar{1}\bar{1}\bar{1}]$  axis from the OOMMF results in Figure 4.2(c). Dipole-like features appeared at the tips agree well with the measurement in Figure 4.3(b). Note that small but non-zero positive magnetic fields appear around the middle of the nanowire in Figures 4.3(a,b). This may come from the intra-magnetic structures of the nanowire, however, fully understanding this phenomenon is beyond the scope of this paper and is an important subject for future research.

## 4.5 Ramsey measurement applications

The continuous-wave ODMR used in Figure 4.3 is a direct and simple, but quite insensitive, method for magnetic sensing and imaging. Its magnetic field sensitivity is limited to the line-width of the resonances, and its fundamental limit can be determined by the inhomogeneous dephasing time of the NV center,  $T_2^*$ . Due to the power broadening effect resulting from laser and microwave photons, the practically achievable smallest magnetic field for a single NV is on the order of  $1 \mu\text{T}$  for a 1 s measurement. In order to avoid this effect, pulsed-wave schemes can be applied such as Ramsey, spin echo, and other dynamical decoupling sequences. In these cases, the field sensitivity is limited by the NV's coherence time of  $T_2^*$  or  $T_2$  which are typically in the range of a few microseconds to a few milliseconds [144, 145]. For instance, the Ramsey measurement can probe DC magnetic fields with a sensitivity as high as  $\sim 10 \text{ nT/Hz}^{1/2}$ . For a better sensitive detection of the static field around

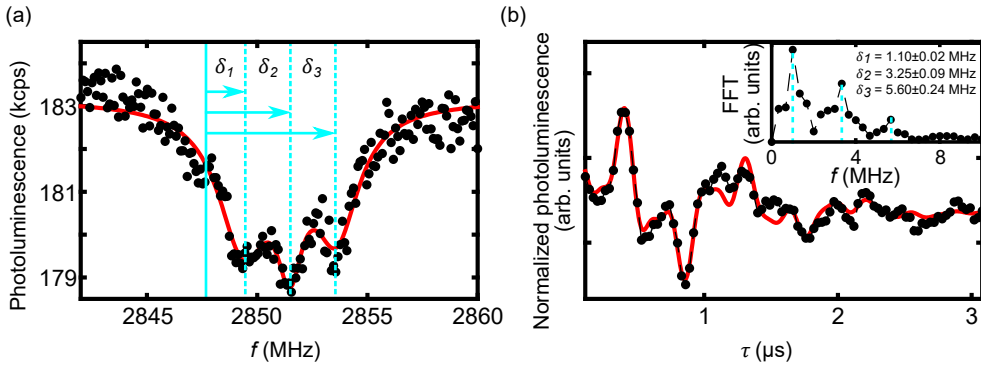


Figure 4.4: Ramsey sequences for sensitive DC measurement. (a) There are three hyperfine resonances in the ODMR spectrum resulting from the coupling between the NV electron spin and  $^{14}\text{N}$  nuclear spin ( $I = 1$ ). Microwave pulses used in the Ramsey sequence are detuned from the resonances by  $\delta_1$ ,  $\delta_2$ , and  $\delta_3$ . (b) Obtained Ramsey signal displays beating patterns of three oscillations at the detunings. The FFT of the signal shows three peaks at the detuning of  $\delta_1$ ,  $\delta_2$ , and  $\delta_3$  (inset). The locations of these peaks will be shifted in the presence of magnetic field from the nanowire.

the nanowire, we implement the Ramsey method.

The Ramsey method consists of the microwave pulse sequence  $\frac{\pi}{2} - \tau - \frac{\pi}{2}$  [95]. The NV spin is first initialized into  $|m_s = 0\rangle$  state with the optical pumping. A  $\frac{\pi}{2}$  microwave pulse is applied to create coherent superposition between  $|m_s = 0\rangle$  and  $|m_s = +1\rangle$  (or  $m_s = -1$ ) states. The spin then starts to evolve and decay during the free precession time,  $\tau$  until a second  $\frac{\pi}{2}$  microwave pulse is applied that brings the spin back to  $|m_s = 0\rangle$  state. Finally, the spin states can be read out through the subsequent laser pulses. When the microwave frequency is detuned from the resonance (e.g.  $|m_s = 0\rangle \leftrightarrow |m_s = -1\rangle$ ), the Ramsey signal exhibits oscillations at the frequency of the microwave detuning  $\delta_i$ . Since there are three hyperfine resonances due to  $^{14}\text{N}$  nuclear spin ( $I = 1$ ), three oscillations appear at the frequencies of three detunings  $\delta_1$ ,  $\delta_2$ , and  $\delta_3$  produce complicated beating patterns shown in Figure 4.4. The fast Fourier transform of the signal clearly shows three peaks separated in frequency by  $\sim 2.2$  MHz that equals to the hyperfine coupling strength. The fit function used for the

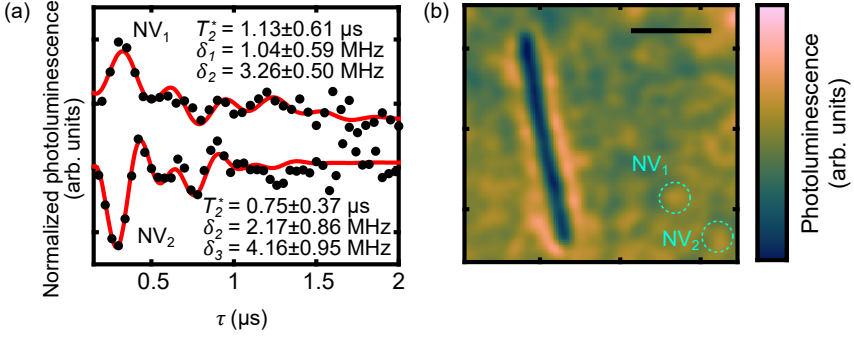


Figure 4.5: Comparison of the Ramsey measurement between two NV centers. (a) The Ramsey data obtained from the NV centers marked in the confocal image (b). For clarity, the plots are offset in  $y$ -axis. Due to detuning that was either too large (for  $\text{NV}_1$ ) or too small (for  $\text{NV}_2$ ), only two oscillations are observable in the measurement (see the text for further information). The fit results are written in the graph. From the fit results of  $\delta_2$ , we extract  $B_{\text{NV}}$  at each NV center:  $B_{\text{NV}} = 40(20) \mu\text{T}$  for  $\text{NV}_1$ , and  $B_{\text{NV}} = 0(30) \mu\text{T}$  for  $\text{NV}_2$ . (b) Confocal image shows locations of the two NV centers. Scale bar,  $5 \mu\text{m}$ .

Ramsey signal is

$$\text{norm.}\mathcal{I}(t) = \text{norm.}\mathcal{I}_0 + e^{-(t/T_2^*)^2} \left( p_0 + \sum_{i=1}^3 p_i \cos(2\pi\delta_i t + \varphi_i) \right), \quad (4.1)$$

where  $\delta_i$  are the three detunings. We add an overall decay term in  $y$ -offset,  $p_0$  and phase offsets in the oscillations,  $\varphi_i$ , which are necessary when the Rabi frequency is low.

In the presence of a magnetic field, the oscillation frequencies are changed due to the Zeeman shift which can be measured by the Ramsey sequence. We compared the Ramsey signals obtained from the two NV centers located at different distances from the nanowire, denoted as  $\text{NV}_1$  and  $\text{NV}_2$  in Figure 4.5. We choose these NVs since the differences in field strength at these locations are smaller than  $0.1 \text{ mT}$  which is too small to be detected by the continuous-wave ODMR measurement. Figure 4.5(a) shows the results and from the fit we obtain  $\delta_1 = 1.04(59) \text{ MHz}$ ,  $\delta_2 = 3.26(50) \text{ MHz}$ ,  $T_2^* = 1.13(61) \mu\text{s}$  for  $\text{NV}_1$ , and  $\delta_2 = 2.17(30) \text{ MHz}$ ,  $\delta_3 = 4.16(95) \text{ MHz}$ ,  $T_2^* = 0.75(37) \mu\text{s}$  for  $\text{NV}_2$ . Note that we fit the data

with only two detunings. For  $NV_1$ , the farthest hyperfine state at  $\delta_3 \sim 5.4$  MHz is barely affected by the Ramsey pulse at the Rabi frequency of 2.1 MHz used in the measurements. On the other hand, for  $NV_2$ , the closest hyperfine state at  $\delta_1 \sim 0.1$  MHz oscillates too slow to be detected within the dephasing time of  $T_2^*$ . For the comparison, therefore, we use the fit results of  $\delta_2$ . The obtained magnetic fields are  $B_{NV} = 40(20)$   $\mu$ T for  $NV_1$ , and  $B_{NV} = 0(30)$   $\mu$ T for  $NV_2$ . The magnetic field at  $NV_2$  is too small to be detected within the fit errors. Nonetheless, we are able to detect the change in magnetic field on the order of 10  $\mu$ T.

### 4.6 Conclusions

In summary, we present sensing and imaging of static magnetic field around a single ferromagnetic nanowire by using diamond atomic sensors. Sensitive DC measurement techniques are implemented using continuous-wave ODMR and Ramsey sequences. The obtained results are compared with numerical simulation yielding quantitative information of the magnetic field and we demonstrate a tens of Tesla level of DC field sensitivity. Though the measurements presented in this paper were performed under dry conditions, we expect that they can be improved further in several ways. The current experimental setup designed for dry nanowire samples can be extended to an optimized configuration for conducting experiment in liquid. For instance, microfluidic devices combined with wide field-of-view optics and total internal reflection fluorescence microscope can be implemented. With similar configurations, magnetic imaging of biological samples in aqueous solution has been successfully demonstrated in recent diamond NV experiments [56, 58, 138]. Moreover, AC magnetic fields induced by the dynamic motion of the nanowire can be measured using the NV center, which possesses an AC field sensitivity of  $\sim$  nT/Hz<sup>1/2</sup> and a detection bandwidth of  $\sim$  MHz [30, 34]. By characterizing the magnetic field around a single nanowire, this work marks an important step toward monitoring and tracking ferromagnetic nanowires in biomedical applications.

## Chapter 5

# Point-Contacted Graphene Devices

Understanding carrier dynamics has become of significant importance for the studies of graphene transport phenomena. Depending on the amount of interaction between carriers, distinct dynamical behaviors can be realized ranging from coherent ballistic transport to hydrodynamic flow of Dirac fluid [146–149]. The spatially resolved imaging technique can provide direct visualization of current distribution and thus yield complementary understanding of the carrier dynamics combined with the conventional transport measurement. For instance, a parabolic current profile in the graphene channel can be used to confirm the existence of viscous Poiseuille flow of Dirac fermions [150, 151]. In the ballistic regime, on the other hand, the ideas of “electron optics” have been proposed where the optics-like control of coherent electron paths can be achieved by diverging, focusing, or collimating the electron beam [152–155]. As the surprising features such as negative refraction in the graphene p–n junction [152] or specular Andreev reflection at the graphene/superconductor interface [156] often occur through narrow transport trajectories, spatially mapped local measurements are crucial for the studies.

In this regard, a scanning probe microscope (SPM) is a powerful tool due to its ability to image current flow with high sensitivity and spatial resolution. Over the last few years, several different types of SPM have been used in the study of graphene transport. For instance,

cyclotron orbital motion of the electron under the magnetic field is imaged by scanning gate microscopes [157]. Simultaneous mapping of voltage and current density is demonstrated by scanning single electron transistors [158]. Different current profiles between Ohmic and hydrodynamic regimes are illustrated from the measurement with single-spin scanning magnetometers [150, 151].

Here, we use a single-spin scanning magnetometer to image current profiles in point-contacted graphene devices. A point contact (PC) is a point-like source or drain of current in graphene transport devices, which provides a well-defined current path for various “electron optics” experiments such as Veselago lensing, magnetic focusing, and collimation of electron beams [152–155]. Small PCs (e.g.,  $\sim 100$  nm in diameter) have been fabricated in graphene devices and characterized by the multi-terminal transport measurement combined with the electrostatic model calculation [159], but the relevant current profile has not been directly imaged. In this article, we demonstrate imaging of the magnetic field due to current distribution in graphene, by using a single-spin scanning magnetometer based on a nitrogen-vacancy (NV) center in diamond. From the stray field data, we reconstruct the current density map, which is consistent with the expected pattern of diffusive electron flow.

### 5.1 Point contacted graphene

As shown in Figure 5.1, we developed two types of point-contacted graphene structures: device #1: narrow channels of patterned graphene and device #2: inner metal contacts with electrodes. The former design is beneficial in terms of scanning experiment as the contacts are located at the same plane as the graphene and are well separated from taller electrodes, thus providing a relatively flat scanned area around the contacts. On the other hand, the latter design is more suitable in conventional transport experiment as the electrodes are directly connected to graphene via the contacts. For both devices, mono layer graphene is encapsulated in atomically flat hexagonal boron nitride (hBN) crystals (top and bottom of

## 5.1. Point contacted graphene

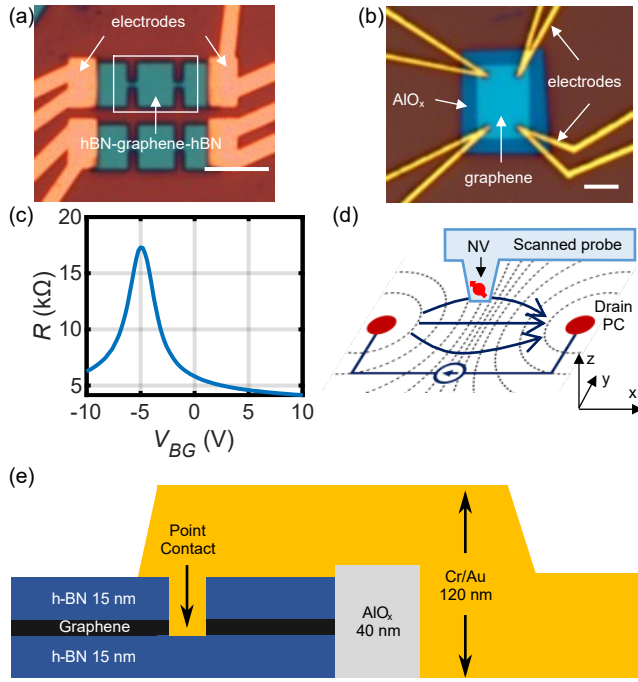


Figure 5.1: Graphene point contact devices. (a) Optical image of device #1. A rectangular shape of hBN-encapsulated graphene is patterned to have two narrow channels in the middle (channel width is  $\sim 500$  nm and their separation is  $\sim 2$   $\mu\text{m}$ ). (b) Optical image of device #2. There are four point contacts at the corners of a rectangular hBN-encapsulated graphene and their relative separations are  $3$   $\mu\text{m}$ ,  $5$   $\mu\text{m}$ , and  $5.8$   $\mu\text{m}$ . The electrodes are electrically connected to the graphene through holes in the top-hBN. The hole diameter is  $\sim 500$  nm. Scale bars  $3$   $\mu\text{m}$ . (c) Graphene resistance vs back gate voltage. To prevent the device from significant Joule heating, we maintain the resistance below  $5$   $\text{k}\Omega$  by applying  $+5$  V gate voltage. (d) Schematic of imaging the current profile between two point contacts. We define  $(x; y; z)$  Cartesian coordinate such that the  $z$  axis is perpendicular to the graphene surface located in the  $(x; y)$  plane and the  $x$  axis is along the direction of two PCs. The dashed lines are equipotential contours and the solid line arrows indicate the direction of current. (e) Cross-section of the device #2.

the graphene). The dry-transfer technique is used to ensure a high-quality transport channel by avoiding any contamination on graphene [160]. For the device in Figure 5.1(a), we define the device geometry by electron beam lithography and reactive ion etching (RIE) with  $\text{CF}_4$  and  $\text{O}_2$  plasma. The channel width (i.e., size of contacts) is about 500 nm. For the device in Figure 5.1(b), on the other hand, we define a circular pattern of 500 nm diameter on PMMA [poly(methyl methacrylate)] mask by electron beam lithography followed by RIE to expose graphene for contact. Then, Au/Cr is deposited by electron beam evaporation using the same PMMA mask for RIE that prevents contamination of the exposed graphene edge. We cap the edges of graphene mesa with aluminum oxide to prevent extra current paths except for the contacts. Note that the contact in this paper is relatively large compared with typical PCs (e.g., 100 nm). Nevertheless, it is much smaller than the graphene device, thus acting as an effective point contact.

Figure 5.1(c) shows a resistance measurement of the device as a function of back gate voltage. For the entire experiment in this paper, we applied a back gate voltage of +5 V to avoid the sample resistance larger than  $\sim 5 \text{ k}\Omega$ , where we observed a substantial increase in the resistance due to Joule heating after  $\sim 20 - 30 \text{ h}$  of continuous experiments. A DC of  $\sim 100 - 200 \mu\text{A}$  is supplied to the graphene devices via PCs. Note that the power dissipated by the DC ( $< 0.2 \text{ mW}$ ) is less than the overall dissipation in the NV measurement itself ( $\sim \text{mW}$ ) and does not result in noticeable heating issues in our experiment at room temperature and ambient conditions.

When current flows in graphene, its magnitude and spatial distribution can be determined by measuring the current-induced stray field with the help of the scanning probe technique depicted in Figure 5.1(d). We used a commercial diamond scanned probe that hosts a single NV center at the end of the tip apex [112]. It is combined with a home-built scanning system and confocal optics for the NV's photoluminescence measurement. The NV center is an atomic-size spin qubit that is highly sensitive to the magnetic field [55, 60, 161]. The ground state of NV's electron spin (i.e.,  $S = 1$ ) is described by the spin Hamiltonian,

## 5.2. Magnetic imaging using scanning NV microscope

$\hat{H}/h = D_0\hat{S}_{\text{NV}}^2 + \gamma_e B_{\text{NV}}\hat{S}_{\text{NV}}$ , where the zero field splitting is  $D_0 = 2.87$  GHz, the electron gyromagnetic ratio is  $\gamma_e = 28$  MHz/mT, and  $B_{\text{NV}}$  is the external magnetic field projected along the NV's quantization axis. The nonzero spin levels are subjected to be shifted in the presence of magnetic field and the Zeeman splitting is measured by optically detected electron spin resonance (ESR) spectrum shown in Figure 5.2(a). For more precise determination of the amount of splitting, we implemented the differential measurement with the lock-in technique, where we modulate the frequency of the microwave and find the location of ESR resonance from the  $x$ -intercept of the modulated signal shown in Figures 5.2(b,c). With a permanent magnet, we apply 0.6 mT of static magnetic field along the NV axis. An additional shift in ESR resonance is recorded as the field from the device itself. In our experiment, we estimate that the magnetic field sensitivity of the scanned probe is  $\sim 7 \mu\text{T}/\text{Hz}^{1/2}$ , Figure 5.2(d) which corresponds to the current density sensitivity of  $\sim 9 \text{ A}/(\text{m Hz}^{1/2})$ .

As the current-induced Oersted field decreases inversely proportional to the distance from the sample, we position the scanning tip close to the sample and scan it over the surface at a constant height. This is done by approaching the tip to touch the surface, retracting it to a constant height from the surface, and performing the ESR measurement for 1 s. We repeat the procedure over at every pixel in the scanned area. After considering thermal drift during the ESR measurement and uncertainties in the NV depth and the angle between the tip and sample, we estimate the NV-sample distance to be  $\sim 70 - 90$  nm.

## 5.2 Magnetic imaging using scanning NV microscope

Figure 5.3 shows the experimental results of device #1; the dashed rectangle in Figure 5.1(a). Similar designs of the graphene transport channel are used in recent experiments [150, 151], but it is much narrower in our device (i.e., channel width  $\sim 500$  nm) making it as an effective PC. For the experiment, we supply a DC of  $100 \mu\text{A}$  from the left PC to the right PC. By using the Biot–Savart law based on the current profile in Figure 5.3(a), we compute

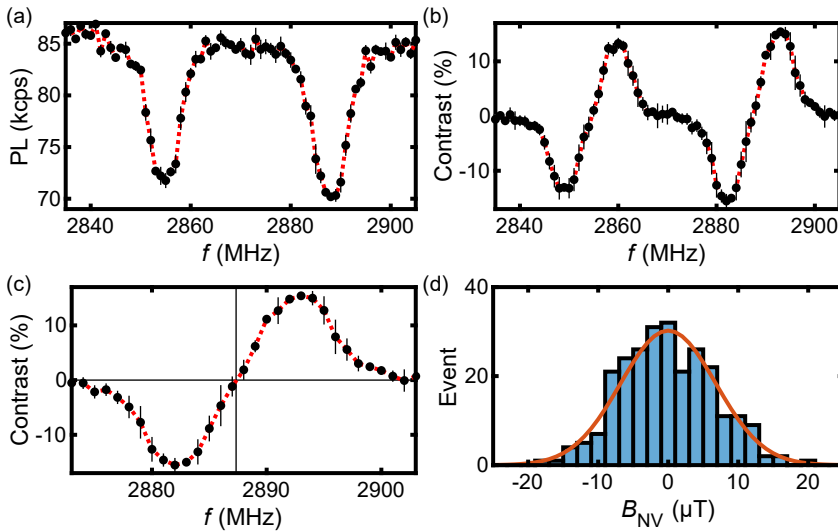


Figure 5.2: Probing magnetic field via ESR. (a) Optically measured ESR spectroscopy of the diamond NV center. The difference in the resonance frequencies corresponds to the amount of Zeeman splitting that is proportional to the magnetic field along the NV axis. (b) ESR data measured by frequency modulated lock-in methods. (c) The resonance frequency is determined from the  $x$  intercept of the frequency modulated data. (d) The histogram of the magnetic field measurements shows that the minimum detectable magnetic field for 1 s measurement is  $\sim 6.8 \mu\text{T}$ .

## 5.2. Magnetic imaging using scanning NV microscope

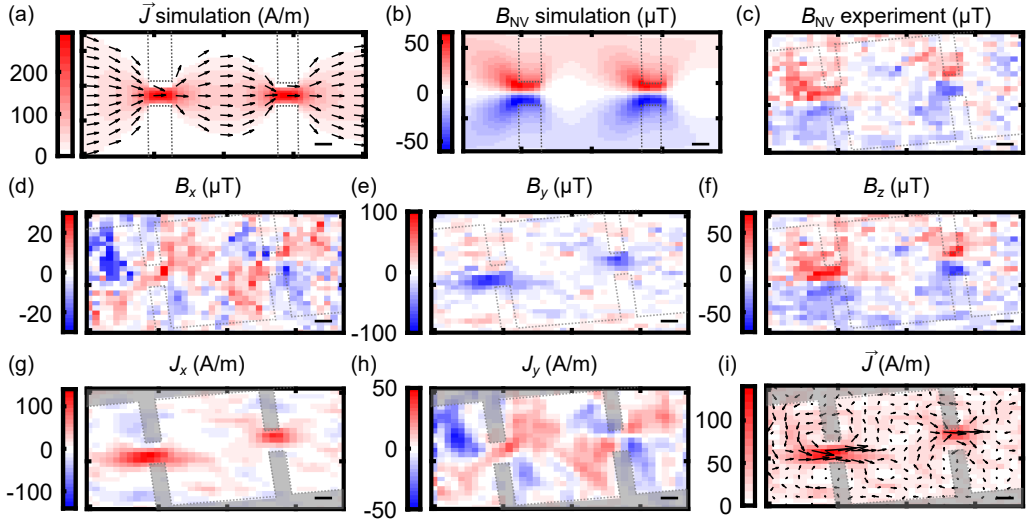


Figure 5.3: Reconstruction of current density in device #1. (a) Simulated current density with the supplied current of  $100 \mu\text{A}$ . (b) Simulation of magnetic field along the NV axis,  $B_{\text{NV}}$  based on the current density in (a). (c) Measured  $B_{\text{NV}}$  with the scanning magnetometer described in Figure 5.1(d). The pixel size of the image is  $50 \text{ nm}$  and it takes  $1 \text{ s}$  of the measurement for each pixel. (d)–(f) From the data in (c), we obtain the magnetic images of  $(B_x, B_y, B_z)$ . (g)–(i) We reconstruct the current density of  $J_x, J_y$  and  $\vec{J}(x, y) = (J_x, J_y)$  with the help of the reconstruction method described in the main text. Note the color and arrows in (i) indicate the magnitude and direction of  $\vec{J}$ . The dotted lines in all images are guidelines of the graphene. Note that the non-zero current density in the shaded areas is an artifact from the reconstruction process. All scale bars  $500 \text{ nm}$ .

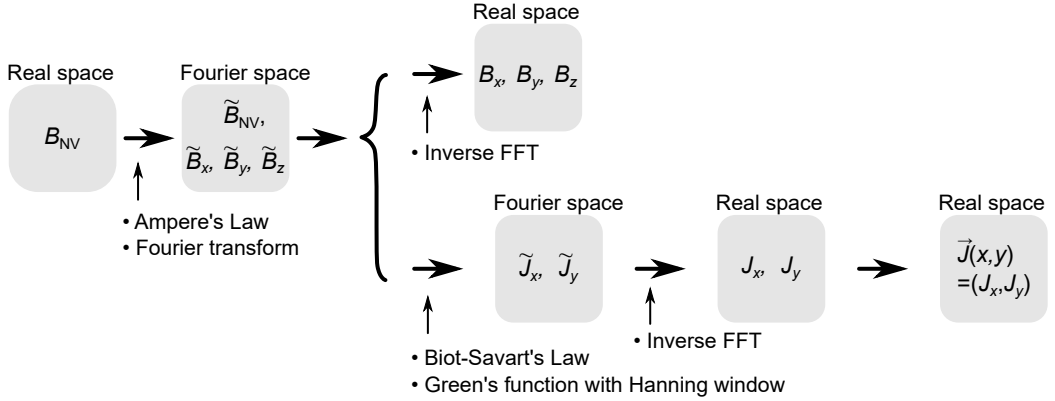


Figure 5.4: Flow diagram of the reconstruction process. Using Ampere's law and Fourier transform, we first convert the real space data of  $B_{NV}$  into Fourier space counterparts of  $\tilde{B}_{NV}$ ,  $\tilde{B}_x$ ,  $\tilde{B}_y$ , and  $\tilde{B}_z$ . Using inverse Fourier transform, we obtain the real space images of  $B_x$ ,  $B_y$ , and  $B_z$ . Or using Biot-Savart's law and the model Green's function with Hanning Window, we calculate Fourier space current density,  $\tilde{J}_x$  and  $\tilde{J}_y$ . With inverse Fourier transform, we convert these into real space values of  $J_x$  and  $J_y$ . Finally we reconstruct the current density,  $\vec{J}(x, y) = (J_x, J_y)$ .

the field distribution of  $B_{NV}$ . Note that the  $NV$ 's orientation angle is  $(\theta, \phi) = (54.7^\circ, 180^\circ)$ , where  $\theta$  is a polar angle and  $\phi$  is an azimuthal angle based on the coordinate in Figure 5.3(d). As seen in Figures 5.3(b) and 5.3(c), the simulated and measured images of  $B_{NV}$  agree with each other confirming the expected current flow in Figure 5.3(a).

### 5.3 Current profile reconstruction

The central question is whether one can do this in a reverse way, namely, reconstructing current density from the measured magnetic field. Since the current is confined in the  $xy$ -plane of two-dimensional (2D) graphene, we only need to consider the current density of  $J_x$  and  $J_y$ . It is also known that reconstruction of the 2D current density is feasible even from a single component of the magnetic field when it is spatially mapped over the surface at a

### 5.3. Current profile reconstruction

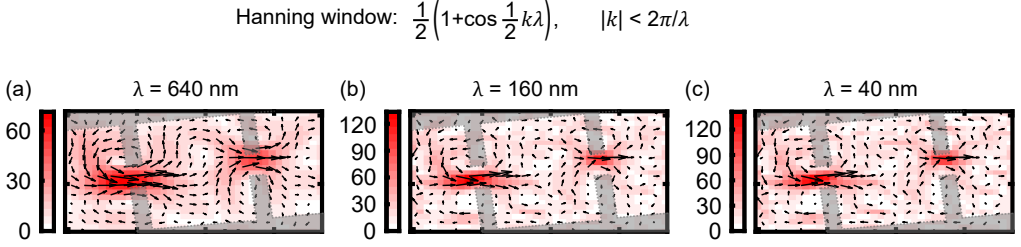


Figure 5.5: Effect of the Hanning Window in the reconstructed current density profile. The Hanning Window function used in the reconstruction process contains the cut-off wavelength,  $\lambda$ . If it is too big (e.g.  $\lambda = 640 \text{ nm}$ ), fine features of  $\vec{J}$  is not shown due to spatially averaged out. If it is too small (e.g.  $\lambda = 40 \text{ nm}$ ), higher frequency components of wave vector  $k$  are not effectively filtered out. For the figures in the main text, we used a value in between i.e.  $\lambda = 160 \text{ nm}$ .

fixed height from the sample [161–164]. For the simulation, we assume that the NV center’s height is kept to be constant at  $z = 80 \text{ nm}$  during the scanning process. With these conditions, we adopt the reconstruction methods used in Refs [161–164]. As shown in Figures 5.3(d–h), we are able to reconstruct both  $\vec{B}(x, y, z) = (B_x, B_y, B_z)$  and  $\vec{J}(x, y) = (J_x, J_y)$  from the  $B_{\text{NV}}(x, y, z = 80 \text{ nm})$  data with the help of the Biot–Savart law, Ampère’s law, and Fourier analysis (more information of the reconstruction process is discussed in Figure 5.4 and Appendix B). Finally, we obtain the image of the current density,  $\vec{J}$ , in Figure 5.3(i) showing the largest magnitudes,  $|\vec{J}|$ , around the PCs as expected from Figure 5.3(a). Note that the discrepancy in the magnitude between Figures 5.3(a) and 5.3(i) is mainly due to uncertainty in the NV-sample distance as well as the finite truncation and filtering effect of the signal during the Fourier analysis in the reconstruction process [161–165] (see Figure 5.5).

In Figure 5.6, we repeat the same measurement with the reversed direction of current. Figure 5.6 displays close-up images around one of the channels with opposite directions of current. As seen in Figs. 5.6(a) and 5.6(b), the sign of the magnetic field,  $B_{\text{NV}}$ , across the

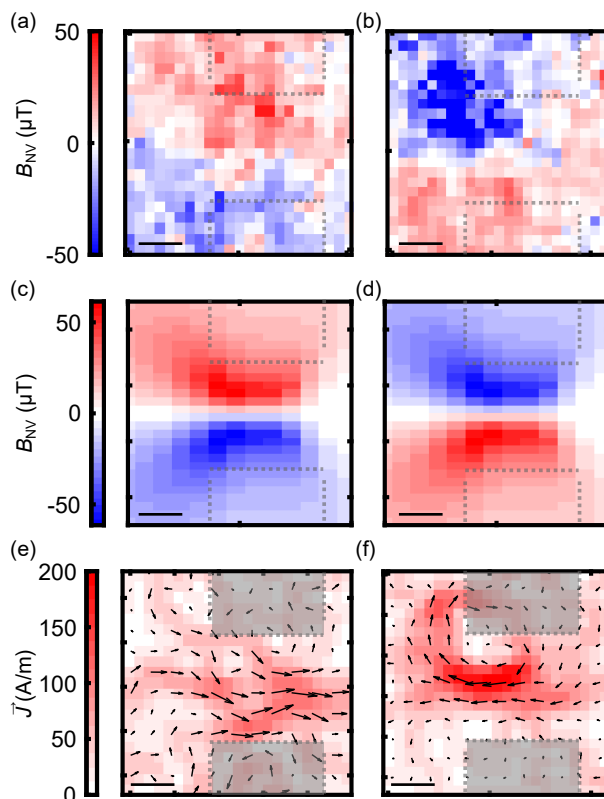


Figure 5.6: Measurement with the opposite directions of current flow. (a) and (b) Measured  $B_{NV}$  around a point contact in device #1 but with the reversed direction of current; from left to right in (a), and the opposite in (b). (c) and (d) Expected  $B_{NV}$  images according to the current direction in (a) and (b). (e) and (f) Reconstructed current density based on the measurement in (a) and (b). The dotted lines in all images are guidelines of the graphene channel. Note that the non-zero current density in the shaded areas is an artifact from the reconstruction process. All scale bars 200 nm.

channel width gets flipped as expected from the simulations in Figs. 5.6(c) and 5.6(d). With the same method used in Figure 5.3, we reconstruct the current density images in Figures 5.6(e) and 5.6(f). The arrows indicate the direction of reconstructed  $\vec{J}$  that matches with the direction of the injected current. Note that the results only confirm the overall flow pattern of  $\vec{J}$ . Understanding a detailed profile within the contact requires additional experiment with improved spatial resolution and sensitivity. Moreover, an artifact from the reconstruction process can happen particularly around the edges of the scanned image. In order to satisfy the continuity equation ( $\nabla \cdot \vec{J} = 0$ ) at the edges after the inversion of the Biot–Savart law, for instance, the reconstructed current density may produce unrealistic flowing patterns such as backflow or vortex.

As a next step, we move to the measurement of device #2 in Figure 5.1(b). Compared to device #1, this type of PC device is expected to be more practical in graphene applications but makes it harder to do scanning magnetometry experiment. For instance, the finite height of the top electrode can affect the scanning condition at a constant height and the current flowing through the electrode itself generates the Oersted field, making it difficult to selectively image the current only flowing in the graphene layer. Nonetheless, the spatially resolved field profile provides useful insights into the PCs' functionalities.

Figure 5.7(a) shows the scanned image of the magnetic field,  $B_{NV}$ , over the area in the inset. For the experiment, we use the two top PCs and supply DC of 200  $\mu\text{A}$  from the left (i.e., PC<sub>1</sub>) to the right (i.e., PC<sub>2</sub>). In this experiment, the NV's orientation angle is  $(\theta, \phi) = (54.7^\circ, 150^\circ)$ . We first characterize the distance dependence of the measured data from the contacts. Figure 5.7(a) shows the field data along the dashed line in Figure 5.7(a). The line cut profile can be understood by  $\sim 1/r$  dependence of the current density. Current from a point-like source isotropically spreads into 2D graphene, resulting in a current density of  $J(r) \sim \mathcal{I}/(2\pi|r - r_i|)$ , where  $\mathcal{I}$  is the current and  $|r - r_i|$  is the distance from a PC at  $r_i$  [159]. As the magnetic field on graphene is proportional to the current density,  $J(r)$  by the Biot–Savart law, the magnetic field component along the NV axis is also represented as

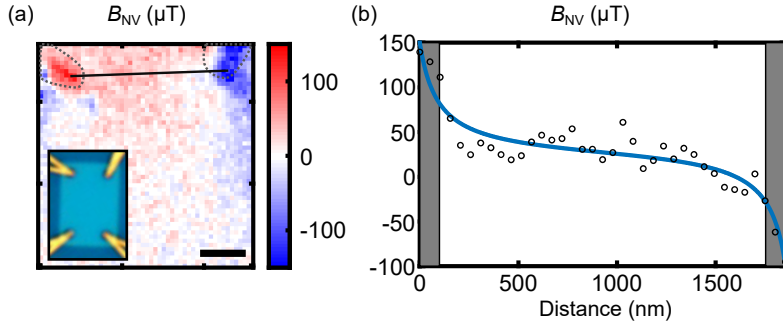


Figure 5.7: Magnetic field measurement on device #2. (a) Scanned image of  $B_{NV}$ . The two top point contacts in the inset are used for the experiment and DC of  $200 \mu\text{A}$  is supplied from the left to the right point contact. Scale bar 500 nm. (b) The line cut profile along the dashed line in (a) shows that the measured magnetic field is inversely proportional to the distance from the point contacts. The shade indicates where the top electrodes [dotted curves in (a)] are located over the point contacts.

$B(r) \sim 1/|r - r_i|$ . We fit the line cut data in Figure 5.7(b) with the equation:

$$B(r) = B_0 + B_1 (r_2 - r_1) \left( \frac{1}{r - r_1} + \frac{1}{r - r_2} \right) \quad (5.1)$$

where  $r_1$  and  $r_2$  are the position of each PC. The fit results are  $r_1 = -90(46)$  nm,  $r_2 = 1942(44)$  nm,  $B_1 = 5.7(24)$   $\mu\text{T}$ , and  $B_0 = 27.6(61)$   $\mu\text{T}$ .

Finally, we reconstruct the current density map of device #2 by using the same method in Figure 5.3. We assume the NV height at  $z = 80$  nm. Figure 5.8 shows the measured image of  $B_{NV}$  around the PC2 as well as the reconstructed images of magnetic field ( $B_x, B_y, B_z$ ) and current density ( $J_x, J_y, |\vec{J}|$ ). The reconstructed image of  $\vec{J}$  in Figure 5.8(g) indicates that the largest magnitude occurs around the contact and the direction is toward it (i.e., drain contact). Note that nonzero current flow along the edge of the device is also visible. However, the overall distribution is not as clear as the one with device #1, which is mainly due to the relative difficulties of scanning measurement on this type of device as discussed earlier.

### 5.3. Current profile reconstruction

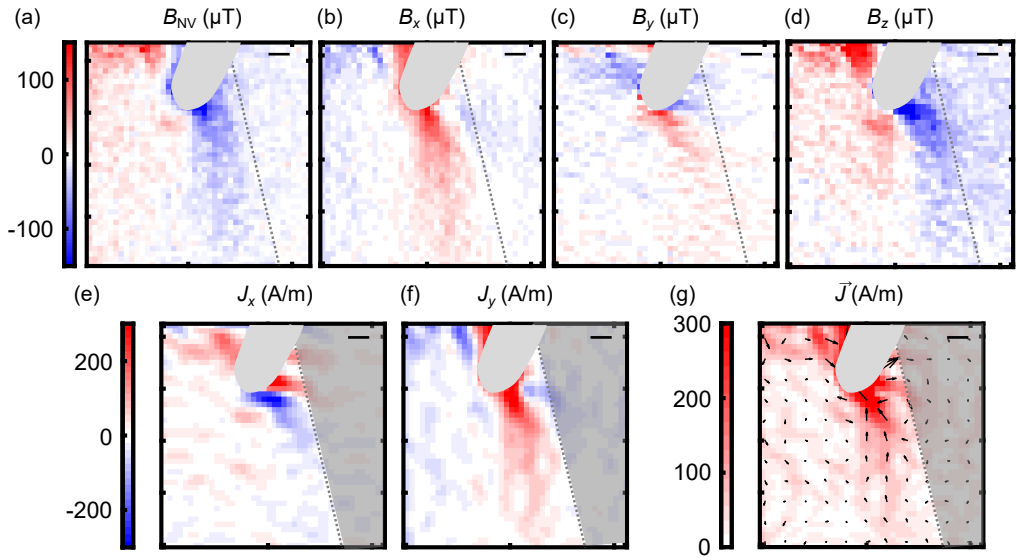


Figure 5.8: Reconstruction of current density in device #2. (a) Close-up measurement of  $B_{NV}$  around the drain point contact (the right one in Figure 5.7). (b) and (c) Magnetic images of  $(B_x, B_y, B_z)$  converted from the data in (a). (e)–(g) Reconstructed images of  $J_x$ ,  $J_y$  and  $\vec{J}(x, y) = (J_x, J_y)$ . The dotted lines in all images indicate a graphene edge. Note that the non-zero current density in the shaded areas is an artifact from the reconstruction process. All scale bars 200 nm.

## 5.4 Conclusions

In summary, we demonstrate the reconstruction of the current density in point-contacted graphene devices from the spatially resolved magnetic field measurement. For the experiments, we use a single-spin scanning magnetometer based on a diamond NV center that can probe a small stray field down to  $\sim 7 \mu\text{T}/\text{Hz}^{1/2}$  with a high spatial resolution of 80 nm. Using the current reconstruction method, we are able to convert the field data into the 2D current density map. The reconstructed results show diffusive current flow where the maximum current density occurs at PCs and the current spreads over the devices. Studying detailed profiles within the contact, however, requires improved spatial resolution and field sensitivity, which can be realized by applying advanced sensing methods such as spin Hahn echo or dynamical decoupling sequences [55, 150]. A point-like current source can be useful in a variety of graphene experiments in both ballistic and hydrodynamic transport regimes [146–156]. Therefore, the scanning magnetometry measurement described in this paper could provide useful insights into the studies of novel transport experiments based on the graphene PC devices.

## Chapter 6

# Dynamics in Permalloy

Magnetic imaging in thin films was studied by various methods such as optical Kerr effect microscopy (MOKE) [166–168], X-ray circular dichroism (XMCD) [169–171], magnetic force microscopy (MFM) [172], superconducting quantum interference devices microscopy (SQUID) [173, 174] and diamond nitrogen-vacancy center magnetometers [175, 176]. These methods are used complementary because the experimental requirements are different, such as high vacuums, cryogenics, or large synchrotrons. Also, these measurements touch different dimensions in length and time. The structure and dynamical properties of magnetic domains in a ferromagnetic film such as permalloy are studied using these techniques [177, 178]. The magnetic domain and vortex formation between domains have been reported, and the dynamics of magnetism have been studied with the Landau-Lifshitz-Gilbert equations [179, 180]. In previous work, magnetic films and materials have been studied using the NV center scanning probe microscope (SPM) [175, 176], and the dynamics and resonance of magnetic domains with quantum sensing with the NV center have been reported [177, 181–183].

In this work, we used NV SPM to investigate a static magnetic field map and a local excited microwave feature above the permalloy square. The static field is generated by magnetization in the permalloy. The electron spin resonance of NV centers has been shown for static magnetic field imaging. Also, this NV center could be coupled with a microwave. That

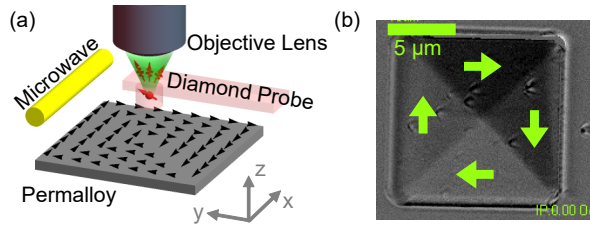


Figure 6.1: (a) Experimental Schematics. Diamond probes hosting single NV centers acquire static magnetic field and Rabi oscillation using ODMR on each position of Py. Microwave  $\sim 3$  GHz is used to excite magnetic resonance in NV centers. Gold wire is used to generate the microwave. (b) Magneto optical Kerr effect microscopy images. Each color shows direction of magnetization of domains. It shows four magnetic domain around vortex. Scale bar  $5 \mu\text{m}$ .

has been represented by Rabi oscillations of electron spin in NV centers.

The coupling between magnetic materials and spin qubits has received a lot of research attention as not only a qubit environment interaction but also magnonic quantum devices. Most stray field imaging studies have focused mainly on static magnetic field or measured magnetization in materials. The imaging near field microwave on magnetic materials could open the understanding of microwave field generated by magnetic materials.

This study shows that Rabi oscillations coupled with driven oscillations of permalloy and this coupling could be different in each position of magnetic materials. We show the enhanced and suppressed Rabi oscillation is measured directly and its effects on ESR contrast.

## 6.1 Experimental details

The experimental setup is shown in Figure 6.1(a). We used home-built confocal microscopy to address and detect a single NV center in a diamond probe [40, 110]. The electron spin resonance (ESR) of NV centers is acquired by confocal optics. The gold microwave wire is along the  $x$  direction on the samples. It generates microwave oscillating with  $y, z$  directions [184]. This  $\sim 3$  GHz microwave is used to generate a microwave for the NV ESR measurement. Magnetic field is measured from the spin resonance detection. Using home built atomic force microscopy (AFM), this magnetic field sensing is performed on each point of a

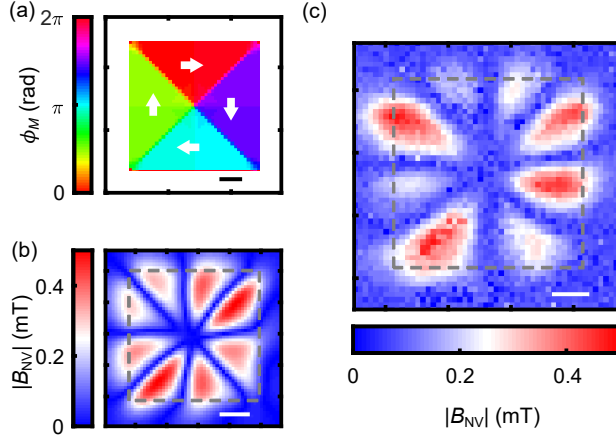


Figure 6.2: (a) Magnetic simulation of permalloy square. (b) Magnetic field simulation on permalloy square. (c) Magnetic field imaging using ESR measurement. All scale bars  $2 \mu\text{m}$ .

permalloy square with a tip-sample distance of  $\sim 1200 \text{ nm}$ . A microwave antenna is used to excite the microwave for spin resonance in NV and drive permalloy domain motion.

We simulated magnetization in the permalloy domain using object-oriented micro magnetic simulation [141, 180, 185]. Static magnetization on square magnetic permalloy with width of  $10 \mu\text{m}$  and thickness of  $160 \text{ nm}$  is simulated with cell size of  $5 \times 5 \times 20 \text{ nm}^3$ . For static simulation of the permalloy square, magnetization  $M_s = 8 \times 10^5 \text{ A/m}$ , gyromagnetic ratio  $\gamma_e = 28 \text{ MHz/mT}$  were used. Dynamics of magnetization was calculated using Landau-Lifshitz-Gilbert equation

$$\frac{\partial \vec{M}}{\partial t} = -\gamma_e \mu_0 \left( \vec{M} \times \vec{H}_{\text{eff}} \right) + \frac{\alpha}{|\vec{M}|} \left( \vec{M} \times \frac{\partial \vec{M}}{\partial t} \right) \quad (6.1)$$

, where  $\vec{M}$  is local magnetization,  $\vec{H}_{\text{eff}}$  is the effective magnetic field, and  $\alpha$  is the damping constant [177, 178]. The magnetic field projected on the orientation of the NV center was calculated from this result of simulation.

## 6.2 Static magnetic field imaging

We imaged a magnetic field from the permalloy square domain. As shown in Fig. 6.2(a), the result of simulation shows the lateral direction of magnetization in permalloy. There are 4 different directions on domains in square. These directions align counterclockwise around the vortex at the center of the square. We simulated this magnetic field using OOMMF. From the simulation result, the magnetic field generated by these magnetization is calculated shown in Fig. 6.2(b). The magnetic field is calculated with the sample to the imaging plane distance 1200 nm in each direction.

The magnetic field is projected in the NV center orientation, and the magnitude of the projected magnetic field is measured as shown in Figures 6.2(b,c). These images were taken where the sample-tip distance is 1200 nm and each pixel is separated 200 nm. This image shows eight radial leaflets in the permalloy domains. We measured these magnetic images with the magnitude of the magnetic field along the NV direction. As shown in Fig. 6.2(b,c). These magnetic images are compared and show that this permalloy square has a vortex in its center, not just the ferromagnet domains.

This magnetic field map was imaged with other methods. We aimed to compare these imaging methods. As shown in Figure 6.3(a), electron spin resonance signal is measured optically by photon counts rate as a function of the microwave frequency. The ESR signal has a valley at 2870 MHz without magnetic field shown in the blue plot in Figure 6.3(a). These valleys of the ESR signal are led by Lorentzian functions. The degenerate energy levels of the ground state of NV centers split by the Zeeman split. The frequency difference between ESR valleys shows magnitude of the magnetic field. The frequency difference is proportional to the magnetic field along the orientation of the NV center as  $\Delta f = 2\gamma_e B_{NV}$ , where  $\gamma_e = 28 \text{ MHz/mT}$  is the electron gyromagnetic ratio, and  $B_{NV}$  is the magnetic field along the NV centers. The magnetic field is measured from this frequency difference measurement. However, in full ESR spectrum, the photon counts measurement is repeated at each microwave frequency typically a few tens of times. We used different magnetic field sensing in Figure 6.3(c) to show its quantitative comparison with Full ESR images. This

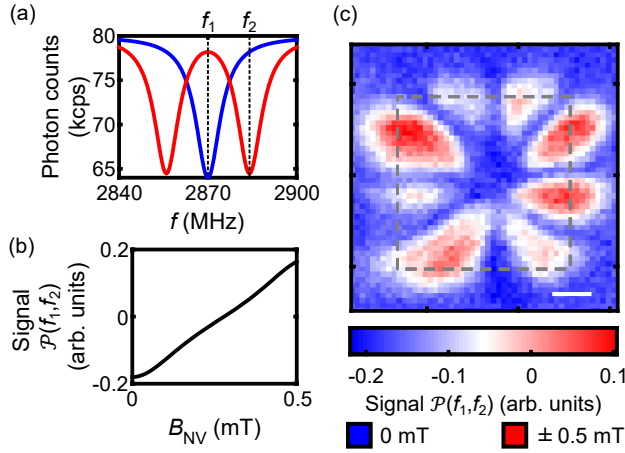


Figure 6.3: (a) ESR signal is acquired photoluminescence as a function of microwave frequency. Magnetic field is measured by the frequency difference of valleys in ESR. (b) Dual frequency measurement signal is proportional to magnetic field. (c) Magnetic field imaging using dual microwave frequency imaging. All scale bars  $2 \mu\text{m}$ .

measurement takes a fixed dual-iso-microwave frequency  $f_1 = 2870$  MHz,  $f_2 = 2878$  MHz in this imaging [186]. The first frequency  $f_1$  was chosen where the frequency position of the zero magnetic field valley and the second frequency  $f_2$  was chosen due to ESR valley where in magnetic field  $B_{NV} = 0.5$  mT.

This signal using dual frequency  $\mathcal{P}(f_1, f_2)$  is defined by  $\mathcal{P}(f_1, f_2) = \mathcal{P}(f_1) - \mathcal{P}(f_2)$  where  $\mathcal{P}(f_1, f_2)$  is the signal plotted in Figure 6.3(b) and  $\mathcal{P}(f)$  is the normalized ESR measurement measured at fixed frequency  $f$ . The dynamic range of the magnetic field and the profile of the signal are followed by the dual frequency  $f_1, f_2$  we picked and the line width of the ESR data. This dual frequency signal is plotted as a function of the external magnetic field in Figure 6.3(b). It shows that this signal is linear in the range from 0 mT to  $\pm 0.5$  mT determined by the two microwave frequencies used.

From these imaging techniques, we measured the magnitude of the magnetic field from the spin resonance spectrum as a function of microwave frequency. The magnetic images shown in Figure 6.3(c) was performed by the dual-iso microwave frequency measurement method where the geometric parameters in the scanning are the same as in Figure 6.2(c).

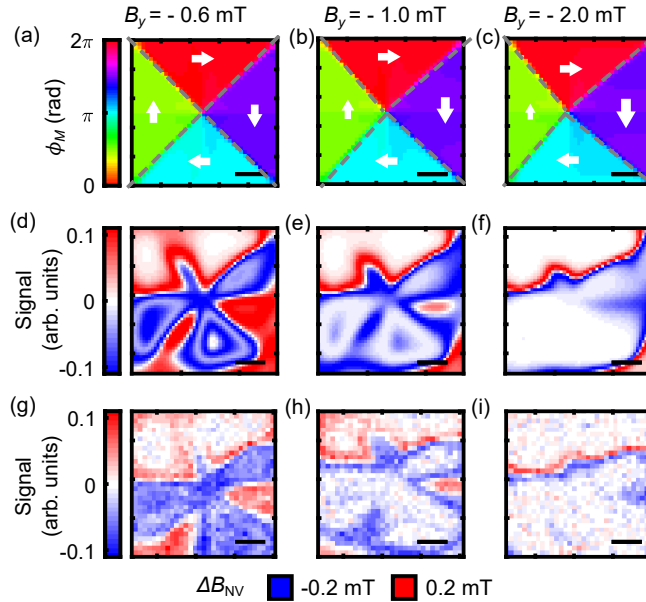


Figure 6.4: Magnetic domain evolution in different magnetic field. The domain of east side is parallel to external field with  $-y$  direction. Size of east side domain by applying external magnetic field. (a,b,c) Domain shows with varying external magnetic field for 0.6 mT, 1.0 mT, and 2.0 mT. The position of vortex moves to right side by external field  $-y$  direction. (d,e,f) Magnetic field simulation by dual-iso imaging method. (g,h,i) Scanning images. All scale bars  $2 \mu\text{m}$ .

### 6.3 Domain driven by external field

These domains evolve in the applied external magnetic field [179]. Scanning NV center magnetometry could be used in various magnetic fields. Shown in Figures 6.4(a-c), Magnetization is simulated with a varying magnetic field where the magnetic field is applied in  $-y$  direction with 0.6 mT, 1.0 mT, and 2.0 mT. When we applied the magnetic field along  $-y$  directions, the east side domain in permalloy where it is parallel to the external magnetic field grows for a larger area. It is qualitatively elucidated that the growth of parallel domain evolution leads to lower energy in magnetization. On the anti-parallel domain on the west side, the domain shrinks in evolution. Due to this mechanism, in Figures 6.4(a-c), the posi-

### 6.3. Domain driven by external field

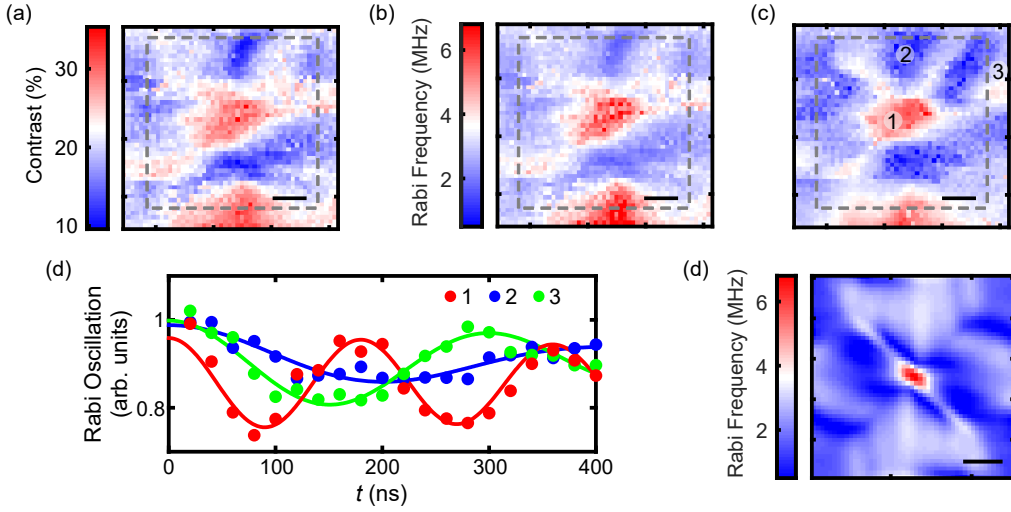


Figure 6.5: (a) Map of ESR contrast. (b) Rabi frequency is calculated from ESR contrast. (c) Image of Rabi frequency. (d) Data of Rabi oscillation of each point labeled in 1, 2, and 3. The frequency of oscillation is Rabi frequency. (e) Rabi frequency is calculated from the simulation of magnetization dynamics. All scale bars  $2 \mu\text{m}$ .

tion of magnetic vortex between parallel and anti-parallel to the external field moves to the left side. The magnetization simulation shows a positive correlation between the distance of the vortex evolution and the magnitude of magnetic field.

From these simulations of magnetic domain evolution, we calculated magnetic images generated on domain evolution. We used this magnetic field map to apply the ESR signals to calculate the image by the dual iso-B imaging method, as shown in Figures 6.4(d-f). The microwave frequencies that present the magnetic contour were selected to show a magnetic field  $\pm 0.2 \text{ mT}$  from the evolving magnetic domains of the external bias magnetic field. These magnetic simulations show the magnetic field variation  $\Delta B_{\text{NV}}$  from  $-0.2 \text{ mT}$  to  $0.2 \text{ mT}$  and the magnetic contour on the red and blue area leading the maximum and minimum magnetic field contour within the dual microwave frequency as shown in Figures 6.4(g-i). These dual-iso-B images show that the domains on the permalloy follow the external magnetic field to stable conditions.

From the static domain evolution example, we expanded the measurement method where the sinusoidal AC magnetic field excites the domains in permalloy. In these cases, we applied the microwave represented by an AC magnetic field oscillating along the  $y$  direction. The sinusoidal magnetic field leads to evolution of the domains on the east and west sides. This evolution is expressed for the vortex dynamics that makes sinusoidal magnetic field on vortex. We predicted that vortex motion is coherent to external microwave so the amplitude of microwave is enhanced on the vortex that is center of the permalloy domains. To confirm this intensity enhancement of microwave, First, We measured the contrast from the NV center ESR on the permalloy domains. As shown in Figure 6.5(a), From the ESR measurement result, the contrast map was obtained by fitting the Lorentzian valleys of ESR result in Figure 6.3(a). The typical contrast  $C$  of optically detected magnetic resonance is  $\sim 20\%$ . This ODMR contrast is positively correlated with the amplitude of the microwave. The contrast map in Figure 6.5(a) shows a position dependently enhanced on the permalloy domains. At the center of the permalloy square, on the vortex, the contrast increases with  $\sim 30\%$ . On the other hand, contrast is suppressed or not affected in typical domains  $< 20\%$ . From the contrast map, we could estimate that the Rabi frequency is amplified on the vortex. The Rabi frequency is the frequency of spin flip of the NV centers in the microwave. That is directly proportional to the amplitude of the microwave. The relation between ODMR contrast  $C$  and Rabi frequency  $\Omega_R$  is defined by

$$\Omega_R = \frac{s}{1+s} \sqrt{\frac{C\Gamma_p^\infty\Gamma_c^\infty}{C_{\text{norm.}} - C}} \quad (6.2)$$

, where  $C_{\text{norm.}}$  is overall normalization factor,  $\Gamma_p$  is optical polarization rate,  $\Gamma_c$  is optical cycle rate, and  $s$  is saturation parameters [187]. We calculated the Rabi frequency for each area using this relation as shown in Figure 6.5(b).

The Rabi frequency image was measured to check that the magnetic field of the microwave is enhanced on the vortex as shown in Figure 6.5(c). This measurement was made in two measurements. First, we measured the ESR signal as in Figure 6.3(a) to pick up the resonance frequency of the NV centers. A microwave frequency was used on resonance of the NV center

in the range of  $\sim 2.87 \text{ GHz} - 2.9 \text{ GHz}$ . This frequency is off resonant of the ferromagnetic resonance frequency  $< 100 \text{ MHz}$  of permalloy square where the width is  $10 \mu\text{m}$  and the thickness  $160 \text{ nm}$  [185]. In this dynamics, the drive by the magnetic field is more dominant than ferromagnet resonance. Second, to image Rabi frequency, the Rabi oscillation of NV center spin was performed where the microwave frequency from the ESR measurement is used. The Rabi frequency is acquired by fitting the oscillation data as shown in Figure 6.5(d). Shown in Figure 6.5(c), This Rabi image shows that the amplitude of microwave is magnified at the center of the domains, because the change of magnetization at the center is easier when we apply an external magnetic field as shown in Figures 6.4(a-c). The various Rabi oscillation data shown in Figure 6.5(d) are represented on the points noted on Figure 6.5(c). From the Rabi oscillation measurement, we confirmed that two physical quantities follow the arguments. The Rabi frequency and contrast are the largest in the center of the domains in Figure 6.5(c,1). At some points of the domains, the Rabi frequency and the contrast are suppressed by destructive interference of the magnetic field generated by the microwave and the motions of excited domains in Figure 6.5(c,2). On the outside of the permalloy square, that quantities were not affected by excited domain motions in Figure 6.5(c,3). Only driving microwave contributed to these Rabi oscillations on that. To compare this imaging with theoretical models, we simulated the magnetic domain dynamics of the permalloy square using Equation 6.1 in the driving microwave. From the magnetization dynamics simulation, the sinusoidal magnetic field generated by the dynamics is calculated and added with external microwave that we applied. The Rabi frequency was calculated from the added oscillating magnetic field. Shown in Figure 6.5(e), the simulated Rabi frequency is followed with its center enhanced profile.

## 6.4 Rabi frequency calculation

Rabi frequency was calculated to compare with the imaging by motion of magnetization in Permalloy. The calculation of motion of magnetization was calculated using OOMMF. We shined the microwave using a microwave wire in the  $x$  directions related to Figure 6.1(a). This microwave wire generates the oscillation of the magnetic field  $B_{\text{MW}}$  of the microwave

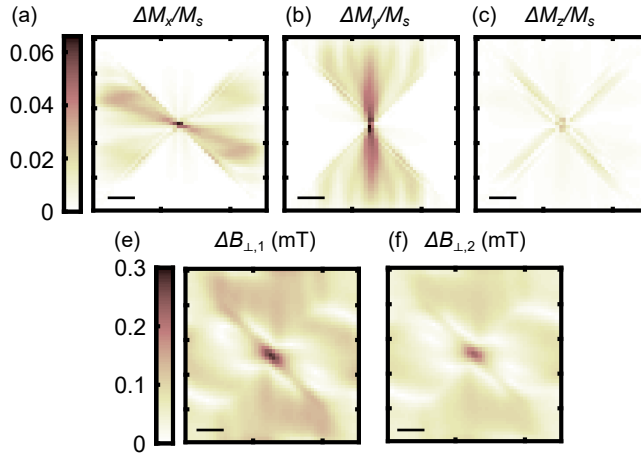


Figure 6.6: (a) The normalized amplitude of oscillating magnetization modulated with frequency  $\sim 3$  GHz for  $\Delta M_x$ , (b)  $\Delta M_y$  and (c)  $\Delta M_z$ . (d) The sinusoidal magnetic field generated by magnetization oscillation in the first direction of perpendicular with NV centers orientation. (e) The sinusoidal magnetic field in the second direction of perpendicular with NV centers. All scale bars  $2 \mu\text{m}$ .

in the  $y - z$  directions  $B_{\text{MW}} = B_0 \frac{(\hat{y} - \hat{z})}{\sqrt{2}} \cos(\omega_{\text{MW}} t)$  where  $B_0 = 0.1$  mT is the amplitude of the microwave and  $\omega_{\text{MW}} = 2\pi \times 3$  GHz is the frequency of the microwave. The oscillation of magnetic field drives magnetic domains in Permalloy vortex. This magnetization dynamics is calculated using the LLG equations presented in Equation 6.1. The amplitude of the magnetization oscillation is shown in Figures 6.6(a-c). These images present two behaviors. First, the left and right sides of the domains already polarized in the  $y$  directions are modulated in the  $x$  directions in Figure 6.6(a). And, the upper and lower sides of the domains are modulated in  $y$  directions. in Figure 6.6(b). They are modulated in perpendicular directions. It follows a typical description of LLG equations. Second, the oscillations domains of all components with  $M_x, M_y, M_z$  are strong in the center of the domains shown in Figures 6.6(a-c). This could be explained quantitatively with Figure 6.4. When the magnetic field was applied, the change of magnetic domains is dominant in the center of Permalloy. In dynamical conditions, the magnetization in the center is easily modulated.

From this simulation of driven magnetization, the magnetic field above the Permalloy

## 6.5. Driven imaging in external static field

square is calculated. Also, the applied microwave is added. To compare with Rabi frequency image, this oscillation of magnetic field is projected on NV centers coordinate. These magnetic field images in the NV center frame are shown in Figures 6.6(d-e). The first  $x$  direction of the magnetic field  $B_{\perp,\tilde{x}}$  represented in the NV frame is defined by the cross product between the  $y$  direction in Figure 6.1(a) and the orientation of the NV centers. The second  $y$  direction of the magnetic field  $B_{\perp,\tilde{y}}$  is defined by the cross product between the orientation of the NV centers and the first direction of  $B_{\perp,\tilde{x}}$ . From these magnetic fields, Rabi frequency is calculated. The Rabi frequency is described by

$$\Omega_{0 \rightarrow 1} = \frac{\gamma_e}{\sqrt{2}} \sqrt{(\Delta B_{\perp,\tilde{x},\cos} + \Delta B_{\perp,\tilde{y},\sin})^2 + (\Delta B_{\perp,\tilde{y},\cos} - \Delta B_{\perp,\tilde{x},\sin})^2}, \quad (6.3a)$$

$$\Omega_{0 \rightarrow -1} = \frac{\gamma_e}{\sqrt{2}} \sqrt{(\Delta B_{\perp,\tilde{x},\cos} - \Delta B_{\perp,\tilde{y},\sin})^2 + (\Delta B_{\perp,\tilde{y},\cos} + \Delta B_{\perp,\tilde{x},\sin})^2}, \quad (6.3b)$$

$$\Omega_{0 \rightarrow 1} \simeq \Omega_{0 \rightarrow -1} \simeq \Omega = \frac{\gamma_e}{\sqrt{2}} \sqrt{\Delta B_{\perp,\tilde{x}}^2 + \Delta B_{\perp,\tilde{y}}^2} \quad (6.3c)$$

, where  $\Omega_{0 \rightarrow 1}$  is Rabi frequency defined in transition between 0 and 1 states and  $\Omega_{0 \rightarrow -1}$  is Rabi frequency defined in transition between 0 and -1 states. In general,  $\Omega_{0 \rightarrow 1}$  described in Equation 6.3a and  $\Omega_{0 \rightarrow -1}$  described in Equation 6.3b could be different. However, the applied microwave is dominant in linear polarization and the microwave generated by domains is in phase with the applied microwave. In this case, the equations are simplified with  $\Omega$  in Equation 6.3c. This calculated Rabi frequency is shown in Figure 6.5(e). It is also similar to the magnetic field in perpendicular directions in Figures 6.6(d-e).

## 6.5 Driven imaging in external static field

The Rabi frequency imaging was confirmed where static bias magnetic field was applied in Figure 6.7. As shown in Figure 6.7(a), the static magnetic field map shows evolution of domains. The image is matched to Figures 6.4(a,d,g) where same bias field. Because of bias field, the magnetic field is not zero in the center of domains.

The contrast of ODMR shown in Figure 6.7(b) was measured simultaneously with Figure

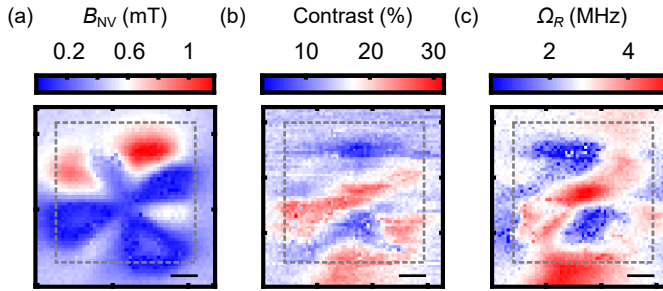


Figure 6.7: (a) Static magnetic field image in bias field  $B_y = -0.6$  mT. (b) Image of ODMR contrast. (c) Image of Rabi frequency. All scale bars  $2 \mu\text{m}$ .

6.7(a). The contrast is large in the center of domains related. As shown in 6.7(c), the Rabi frequency map was imaged to confirm the contrast map. The contrast map and the Rabi frequency are related. These images show that the oscillation of driven magnetization is strong at the center.

## 6.6 Conclusions

We used NV SPM to show magnetic field feature on permalloy domains. These magnetic fields were acquired by NV ESR full spectrum measurement and represented the magnetic field map. Otherwise taking whole time to acquire data from all frequency positions, Dual-Iso-B frequency method was used to measure quantitative field and magnetic contour on its dynamic range. The magnetic domain evolved in external magnetic field to make the parallel domain larger. This evolution is simulated and imaged by these methods. In the driven microwave, this magnetic domain acts like a concave mirror for enhanced microwave on its center by driven motion of domains. The microwave generated by permalloy was measured for Rabi oscillation. This coherent microwave enhancing or suppressing external driven microwave was confirmed by Rabi frequency and ESR contrast [162, 188–190]. Imaging microwave on materials could be a candidate for tools to understand magnetic antennas or magnon quantum devices [191–194].

## Chapter 7

# Conclusions

This dissertation has offered a detailed analysis of the fundamental structure and measurement of NV centers, outlining their importance in the context of nanoscale magnetic field imaging. The experimental equipment used in these studies, including confocal microscopes and scanning probe microscopes, have been thoroughly described, along with instructions on how to make and use them. Through a series of three experimental experiments, we have revealed the extraordinary potential of NV centers in a variety of applications, therefore increasing our understanding of nanoscale magnetic imaging.

The first experimental result demonstrated the capability of NV centers to image magnetic fields surrounding ferromagnetic nanowires. We are able to better understand the behavior of magnetic materials as a result of these results. In addition, these discoveries could pave the way for the creation of improved magnetic storage devices [120, 123], spintronic technologies, and drug delivery robots [125, 126].

In the second experiment, we focused on magnetic field imaging of a graphene point-contact device flowing a current. The capability to transform a magnetic field back into a current enabled a nanoscale analysis of the current distribution and local magnetic fields. This information is essential for understanding the electrical properties of graphene and other two-dimensional materials, which have received a lot of attention due to their distinct characteristics and potential to improve electronics, and emerging materials applications [152, 195].

## Chapter 7. Conclusions

By explaining the relationship between current flow and magnetic fields in these materials, scientists can probe their properties to develop electronic devices with efficiency [153, 157].

The third experimental result showed magnetization in a ferromagnetic film as well as its dynamic responses to microwaves. This study demonstrated the ability to adapt NV centers to characterize magnetic materials and their response to external magnetic fields. It is essential to be able to observe the dynamic behavior of ferromagnetic films under microwave exposure to understand their behavior in high-frequency applications [196], such as communications devices and radar systems [197, 198]. In addition, this information may lead to the creation of unique approaches for probing and adapting magnetic domains, which will allow novel features in future magnetic devices and the realization of long-range spin qubit coupling via a magnon mode [191–194, 199].

We highlighted throughout this dissertation the significance of NV centers in nanoscale magnetic field imaging and their diverse applications in a variety of situations. We have proved the power of NV centers in demonstrating the magnetic characteristics of various materials and systems by using the capabilities of single spin scanning probe microscopes. The experimental discoveries given in this paper have not only contributed to the current understanding of nanoscale magnetic phenomena but also have the potential to motivate further study of broadened magnetic and electrical devices.

Clearly, in the future, NV centers will continue to play an important role in the ongoing investigation of nanoscale magnetism. Certainly the resolution and sensitivity of these systems will improve, as researchers demonstrate the methodology for NV center measurements. This will enable the study of magnetic phenomena and improve our understanding across a broad spectrum of applications. This dissertation finally provides a demonstration of the potential of NV centers to discover nanoscale magnetic field imaging.

# Bibliography

- [1] D. Eigler, “There’s Plenty of Room Beyond The Horizon,” The Center for Quantum Nanoscience (Sept. 26, 2019), Youtube: [Youtu.be/mPJXOEJLXIM?t=9m4s](https://youtu.be/mPJXOEJLXIM?t=9m4s).
- [2] “Diamonds,” *Explained S2E10*, Netflix Series (2019).
- [3] D. M. Dirlam, J. E. Shigley, and S. D. Overlin, “The Ultimate Gemologist: A Tribute To Richard T. Liddicoat,” *Gems & Gemology* **38**, 2–13 (2002).
- [4] S. Eaton-Magana and C. M. Breeding, “An introduction to photoluminescence spectroscopy for diamond and its applications in gemology,” *Gems & Gemology* **52**, 2–17 (2016).
- [5] M.-S. Choi and T. H. Yoon, “Coherent manipulation of the spin in diamond color center,” *Physics and High Technology* **19**, 28 (2010).
- [6] D. Lee, S.-J. Kahng, and M.-S. Choi, “Solid-state-based qubit,” *Physics and High Technology* **27**, 26–28 (2018).
- [7] 최준석, “미세 자기장 측정 양자센서 만드는 이동현 고려대 교수,” *주간조선* **2709** (2022), ISSN: 1284-2709.
- [8] D. Lee, “양자 센서 연구 동향 및 활용 전망,” *IITP 정보통신기획평가원 주간기술 동향* **1960** (2020), ISSN: 1225-6447.
- [9] T. Choi and D. Lee, “Scanning probe microscopy based on diamond quantum defects,” *Physics and High Technology* **27**, 15–17 (2018).
- [10] “<특집 다큐> 꿈의 기술, 미래를 열다 - 양자정보과학,” *EBS*, (Dec. 25, 2022), Youtube: [Youtu.be/twNSzrbyiXM](https://youtu.be/twNSzrbyiXM).
- [11] “Quantum technology is beginning to come into its own,” *The Economist* (Mar. 11,

## Bibliography

- 2017).
- [12] M. Bogobowicz, S. Gao, M. Masiowski, N. Mohr, H. Soller, R. Zimmel, and M. Zesko, “Quantum technology monitor,” *McKinsey & Company* (Apr. 24, 2023).
- [13] National Academies of Sciences, Engineering, and Medicine, *Quantum Computing: Progress and Prospects* (The National Academies Press, Washington, DC, 2019) ISBN: 9780309479691.
- [14] R. P. Feynman, “Simulating physics with computers,” *International Journal of Theoretical Physics* **21**, 467–488 (1982).
- [15] J. Preskill, “Reliable quantum computers,” *Proceedings of the Royal Society of London A* **454**, 385–410 (1998).
- [16] T. D. Ladd, F. Jelezko, R. Laflamme, Y. Nakamura, C. Monroe, and J. L. O’Brien, “Quantum computers,” *Nature* **464**, 45–53 (2010).
- [17] F. Arute, K. Arya, R. Babbush, D. Bacon, J. C. Bardin, R. Barends, R. Biswas, S. Boixo, F. G. S. L. Brandao, D. A. Buell, B. Burkett, Y. Chen, Z. Chen, B. Chiaro, R. Collins, W. Courtney, A. Dunsworth, E. Farhi, B. Foxen, A. Fowler, C. Gidney, M. Giustina, R. Graff, K. Guerin, S. Habegger, M. P. Harrigan, M. J. Hartmann, A. Ho, M. Hoffmann, T. Huang, T. S. Humble, S. V. Isakov, E. Jeffrey, Z. Jiang, D. Kafri, K. Kechedzhi, J. Kelly, P. V. Klimov, S. Knysh, A. Korotkov, F. Kostritsa, D. Landhuis, M. Lindmark, E. Lucero, D. Lyakh, S. Mandrà, J. R. McClean, M. McEwen, A. Megrant, X. Mi, K. Michielsen, M. Mohseni, J. Mutus, O. Naaman, M. Neeley, C. Neill, M. Y. Niu, E. Ostby, A. Petukhov, J. C. Platt, C. Quintana, E. G. Rieffel, P. Roushan, N. C. Rubin, D. Sank, K. J. Satzinger, V. Smelyanskiy, K. J. Sung, M. D. Trevithick, A. Vainsencher, B. Villalonga, T. White, Z. J. Yao, P. Yeh, A. Zalcman, H. Neven, and J. M. Martinis, “Quantum supremacy using a programmable superconducting processor,” *Nature* **574**, 505–510 (2019).
- [18] H. J. Kimble, “The quantum internet,” *Nature* **453**, 1023–1030 (2008).
- [19] T. Schmitt-Manderbach, H. Weier, M. Fürst, R. Ursin, F. Tiefenbacher, T. Scheidl, J. Perdigues, Z. Sodnik, C. Kurtsiefer, J. G. Rarity, A. Zeilinger, and H. Weinfurter, “Experimental demonstration of free-space decoy-state quantum key distribution over 144 km,” *Physics Review Letters* **98**, 010504 (2007).
- [20] B. Hensen, H. Bernien, A. E. Dréau, A. Reiserer, N. Kalb, M. S. Blok, J. Ruitenberg, R. F. L. Vermeulen, R. N. Schouten, C. Abellán, W. Amaya, V. Pruneri, M. W. Mitchell, M. Markham, D. J. Twitchen, D. Elkouss, S. Wehner, T. H. Taminiu, and R. Hanson, “Loophole-free bell inequality violation using electron spins separated by

- 1.3 kilometres,” *Nature* **526**, 682–686 (2015).
- [21] T. Schaetz, C. R. Monroe, and T. Esslinger, “Focus on quantum simulation,” *New Journal of Physics* **15**, 085009 (2013).
- [22] H. Ma, M. Govoni, and G. Galli, “Quantum simulations of materials on near-term quantum computers,” *npj Computational Materials* **6**, 85 (2020).
- [23] C. L. Degen, F. Reinhard, and P. Cappellaro, “Quantum sensing,” *Reviews of Modern Physics* **89**, 035002 (2017).
- [24] V. Giovannetti, S. Lloyd, and L. Maccone, “Advances in quantum metrology,” *Nature Photonics* **5**, 222–229 (2011).
- [25] D. Carney, G. Krnjaic, D. C. Moore, C. A. Regal, G. Afek, S. Bhave, B. Brubaker, T. Corbitt, J. Cripe, N. Crisosto, A. Geraci, S. Ghosh, J. G. E. Harris, A. Hook, E. W. Kolb, J. Kunjummen, R. F. Lang, T. Li, T. Lin, Z. Liu, J. Lykken, L. Magrini, J. Manley, N. Matsumoto, A. Monte, F. Monteiro, T. Purdy, C. J. Riedel, R. Singh, S. Singh, K. Sinha, J. M. Taylor, J. Qin, D. J. Wilson, and Y. Zhao, “Mechanical quantum sensing in the search for dark matter,” *Quantum Science and Technology* **6**, 024002 (2021).
- [26] European Quantum Flagship, “Quantum technologies flagship final report,” (2023), ISBN: 9789276588290.
- [27] 양자 컴퓨팅 기술개발사업, 양자 컴퓨팅 기술 백서 (한양대학교, 2021).
- [28] 한국정보기술통신협회, 2023 ICT 표준화전략맵 양자정보통신 (2022) ISBN: 9791189545420.
- [29] 과학기술정보통신부, 한국지능정보사회진흥원, 2022 양자정보기술백서 (2022) ISBN: 9788984837379.
- [30] R. Schirhagl, K. Chang, M. Loretz, and C. L. Degen, “Nitrogen-vacancy centers in diamond: nanoscale sensors for physics and biology,” *Annual Review of Physical Chemistry* **65**, 83–105 (2014).
- [31] M. S. Grinolds, *Nanoscale Magnetic Resonance Imaging and Magnetic Sensing Using Atomic Defects in Diamond*, Ph.D. thesis, Harvard University (2014).
- [32] M. Steiner, P. Neumann, J. Beck, F. Jelezko, and J. Wrachtrup, “Universal enhancement of the optical readout fidelity of single electron spins at nitrogen-vacancy centers in diamond,” *Physical Review B* **81**, 035205 (2010).
- [33] L. Childress, R. Walsworth, and M. Lukin, “Atom-like crystal defects,” *Physics Today* **67**, 38 (2014).

## Bibliography

- [34] J. Taylor, P. Cappellaro, L. Childress, L. Jiang, D. Budker, P. Hemmer, A. Yacoby, R. Walsworth, and M. Lukin, “High-sensitivity diamond magnetometer with nanoscale resolution,” *Nature Physics* **4**, 810–816 (2008).
- [35] M. S. Grinolds, S. Hong, P. Maletinsky, L. Luan, M. D. Lukin, R. L. Walsworth, and A. Yacoby, “Nanoscale magnetic imaging of a single electron spin under ambient conditions,” *Nature Physics* **9**, 215–219 (2013).
- [36] K. Bian, W. Zheng, X. Zeng, X. Chen, R. Stöhr, A. Denisenko, S. Yang, J. Wrachtrup, and Y. Jiang, “Nanoscale electric-field imaging based on a quantum sensor and its charge-state control under ambient condition,” *Nature Communications* **12**, 2457 (2021).
- [37] J.-P. Tetienne, A. Lombard, D. A. Simpson, C. Ritchie, J. Lu, P. Mulvaney, and L. C. Hollenberg, “Scanning nanospin ensemble microscope for nanoscale magnetic and thermal imaging,” *Nano Letters* **16**, 326–333 (2016).
- [38] S. Choe, J. Yoon, M. Lee, J. Oh, D. Lee, H. Kang, C.-H. Lee, and D. Lee, “Precise temperature sensing with nanoscale thermal sensors based on diamond NV centers,” *Current Applied Physics* **18**, 1066–1070 (2018).
- [39] K. W. Lee, D. Lee, P. Ouartchaiyapong, J. Minguzzi, J. R. Maze, and A. C. B. Jayich, “Strain coupling of a mechanical resonator to a single quantum emitter in diamond,” *Physical Review Applied* **6**, 034005 (2016).
- [40] M. Pelliccione, A. Jenkins, P. Ouartchaiyapong, C. Reetz, E. Emmanouilidou, N. Ni, and A. C. Bleszynski Jayich, “Scanned probe imaging of nanoscale magnetism at cryogenic temperatures with a single-spin quantum sensor,” *Nature Nanotechnology* **11**, 700–705 (2016).
- [41] L. Thiel, D. Rohner, M. Ganzhorn, P. Appel, E. Neu, B. Müller, R. Kleiner, D. Koelle, and P. Maletinsky, “Quantitative nanoscale vortex imaging using a cryogenic quantum magnetometer,” *Nature Nanotechnology* **11**, 677–681 (2016).
- [42] P. J. Scheidegger, S. Diesch, M. L. Palm, and C. Degen, “Scanning nitrogen-vacancy magnetometry down to 350 mK,” *Applied Physics Letters* **120**, 224001 (2022).
- [43] T. Wolf, P. Neumann, K. Nakamura, H. Sumiya, T. Ohshima, J. Isoya, and J. Wrachtrup, “Subpicotesla diamond magnetometry,” *Physical Review X* **5**, 041001 (2015).
- [44] K. K. Chang, *Scanning Magnetometry with NV Centers in Diamond*, Ph.D. dissertation, ETH Zurich (2016).

- [45] M. W. Mitchell and S. Palacios Alvarez, “Colloquium: Quantum limits to the energy resolution of magnetic field sensors,” *Review of Modern Physics* **92**, 021001 (2020).
- [46] P. Maletinsky, S. Hong, M. S. Grinolds, B. Hausmann, M. D. Lukin, R. L. Walsworth, M. Loncar, and A. Yacoby, “A robust scanning diamond sensor for nanoscale imaging with single nitrogen-vacancy centres,” *Nature Nanotechnology* **7**, 320–324 (2012).
- [47] A. Edmonds, U. D’Haenens-Johansson, R. Cruddace, M. Newton, K.-M. Fu, C. Santori, R. Beausoleil, D. Twitchen, and M. Markham, “Production of oriented nitrogen-vacancy color centers in synthetic diamond,” *Physical Review B* **86**, 035201 (2012).
- [48] J. Riedrich-Möller, S. Pezzagna, J. Meijer, C. Pauly, F. Mücklich, M. Markham, A. M. Edmonds, and C. Becher, “Nanoimplantation and purcell enhancement of single nitrogen-vacancy centers in photonic crystal cavities in diamond,” *Applied Physics Letters* **106**, 221103 (2015).
- [49] P. Appel, E. Neu, M. Ganzhorn, A. Barfuss, M. Batzer, M. Gratz, A. Tschöpe, and P. Maletinsky, “Fabrication of all diamond scanning probes for nanoscale magnetometry,” *Review of Scientific Instruments* **87**, 063703 (2016).
- [50] P. Ovarthaiyapong, *Strain-coupled Hybrid Devices Based on Single-Crystal Diamond Mechanical Resonators and Nitrogen-Vacancy Center Qubits*, Ph.D. dissertation, University of California, Santa Barbara (2016).
- [51] G.-Q. Liu, X. Feng, N. Wang, Q. Li, and R.-B. Liu, “Coherent quantum control of nitrogen-vacancy center spins near 1000 kelvin,” *Nature Communications* **10**, 1–8 (2019).
- [52] M. W. Doherty, V. V. Struzhkin, D. A. Simpson, L. P. McGuinness, Y. Meng, A. Stacey, T. J. Karle, R. J. Hemley, N. B. Manson, L. C. L. Hollenberg, and S. Praver, “Electronic properties and metrology applications of the diamond NV<sup>-</sup> center under pressure,” *Physical Review Letters* **112**, 047601 (2014).
- [53] T. Rosskopf, A. Dussaux, K. Ohashi, M. Loretz, R. Schirhagl, H. Watanabe, S. Shikata, K. M. Itoh, and C. Degen, “Investigation of surface magnetic noise by shallow spins in diamond,” *Physical Review Letters* **112**, 147602 (2014).
- [54] J. Tisler, G. Balasubramanian, B. Naydenov, R. Kolesov, B. Grotz, R. Reuter, J.-P. Boudou, P. A. Curmi, M. Sennour, A. Thorel, M. Börsch, K. Aulenbacher, R. Erdmann, P. R. Hemmer, F. Jelezko, and J. Wrachtrup, “Fluorescence and spin properties of defects in single digit nanodiamonds,” *ACS Nano* **3**, 1959–1965 (2009).
- [55] F. Casola, T. van der Sar, and A. Yacoby, “Probing condensed matter physics with

## Bibliography

- magnetometry based on nitrogen-vacancy centres in diamond,” *Nature Reviews Materials* **3**, 1–13 (2018).
- [56] D. Le Sage, K. Arai, D. R. Glenn, S. J. DeVience, L. M. Pham, L. Rahn-Lee, M. D. Lukin, A. Yacoby, A. Komeili, and R. L. Walsworth, “Optical magnetic imaging of living cells,” *Nature* **496**, 486–489 (2013).
- [57] D. R. Glenn, R. R. Fu, P. Kehayias, D. Le Sage, E. A. Lima, B. P. Weiss, and R. L. Walsworth, “Micrometer-scale magnetic imaging of geological samples using a quantum diamond microscope,” *Geochemistry, Geophysics, Geosystems* **18**, 3254–3267 (2017).
- [58] J. F. Barry, M. J. Turner, J. M. Schloss, D. R. Glenn, Y. Song, M. D. Lukin, H. Park, and R. L. Walsworth, “Optical magnetic detection of single-neuron action potentials using quantum defects in diamond,” *Proceedings of the National Academy of Sciences* **113**, 14133–14138 (2016).
- [59] K. Arai, A. Kuwahata, D. Nishitani, I. Fujisaki, R. Matsuki, Y. Nishio, Z. Xin, X. Cao, Y. Hatano, S. Onoda, C. Shinei, M. Miyakawa, T. Taniguchi, M. Yamazaki, T. Teraji, T. Ohshima, M. Hatano, M. Sekino, and T. Iwasaki, “Millimetre-scale magnetocardiography of living rats with thoracotomy,” *Communications Physics* **5**, 200 (2022).
- [60] C. Degen, “Scanning magnetic field microscope with a diamond single-spin sensor,” *Applied Physics Letters* **92**, 243111 (2008).
- [61] D. Lee and J. A. Gupta, “Perspectives on deterministic control of quantum point defects by scanned probes,” *Nanophotonics* **8**, 2033–2040 (2019).
- [62] T. Astner, J. Gugler, A. Angerer, S. Wald, S. Putz, N. J. Mauser, M. Trupke, H. Sumiya, S. Onoda, J. Isoya, J. Schmiedmayer, P. Mohn, and J. Majer, “Solid-state electron spin lifetime limited by phononic vacuum modes,” *Nature Materials* **17**, 313–317 (2018).
- [63] D. Loss and D. P. DiVincenzo, “Quantum computation with quantum dots,” *Physical Review A* **57**, 120 (1998).
- [64] K. W. Lee, *Coherent dynamics of a hybrid quantum spin-mechanical oscillator system*, Ph.D. dissertation, University of California Santa Barbara (2017).
- [65] R. Farrer, “On the substitutional nitrogen donor in diamond,” *Solid State Communications* **7**, 685–688 (1969).
- [66] G. Davies, “Dynamic Jahn-Teller distortions at trigonal optical centres in diamond,” *Journal of Physics C: Solid State Physics* **12**, 2551 (1979).
- [67] B. Grotz, M. V. Hauf, M. Dankerl, B. Naydenov, S. Pezzagna, J. Meijer, F. Jelezko,

- J. Wrachtrup, M. Stutzmann, F. Reinhard, and J. A. Garrido, “Charge state manipulation of qubits in diamond,” *Nature Communications* **3**, 1–6 (2012).
- [68] S. D. Subedi, V. V. Fedorov, J. Peppers, D. V. Martyshkin, S. B. Mirov, L. Shao, and M. Loncar, “Laser spectroscopic characterization of negatively charged nitrogen-vacancy (nv-) centers in diamond,” *Optical Materials Express* **9**, 2076–2087 (2019).
- [69] J. Steeds, S. Charles, J. Davies, and I. Griffin, “Photoluminescence microscopy of TEM irradiated diamond,” *Diamond and Related Materials* **9**, 397–403 (2000).
- [70] Á. Gali, “Ab initio theory of the nitrogen-vacancy center in diamond,” *Nanophotonics* **8**, 1907–1943 (2019).
- [71] C. J. Meara, M. J. Rayson, P. R. Briddon, and J. P. Goss, “Density functional theory study on magnetically detecting positively charged nitrogen-vacancy center in diamond,” *Physical Review B* **100**, 104108 (2019).
- [72] M. W. Doherty, N. B. Manson, P. Delaney, F. Jelezko, J. Wrachtrup, and L. C. Hollenberg, “The nitrogen-vacancy colour centre in diamond,” *Physics Reports* **528**, 1–45 (2013).
- [73] M. W. Doherty, N. B. Manson, P. Delaney, and L. C. Hollenberg, “The negatively charged nitrogen-vacancy centre in diamond: the electronic solution,” *New Journal of Physics* **13**, 025019 (2011).
- [74] J.-P. Chou, Z. Bodrog, and A. Gali, “First-principles study of charge diffusion between proximate solid-state qubits and its implications on sensor applications,” *Physical Review Letters* **120**, 136401 (2018).
- [75] J. R. Maze, A. Gali, E. Togan, Y. Chu, A. Trifonov, E. Kaxiras, and M. D. Lukin, “Properties of nitrogen-vacancy centers in diamond: the group theoretic approach,” *New Journal of Physics* **13**, 025025 (2011).
- [76] L. I. Childress, *Coherent manipulation of single quantum systems in the solid state*, Ph.D. dissertation, Harvard University (2007).
- [77] G. Davies and M. Hamer, “Optical studies of the 1.945 eV vibronic band in diamond,” *Proceedings of the Royal Society of London A* **348**, 285–298 (1976).
- [78] M. Lesik, *Engineering of NV color centers in diamond for their applications in quantum information and magnetometry*, Ph.D. dissertation, L’École normale supérieure (ENS) de Cachan (2015).
- [79] V. Acosta, A. Jarmola, E. Bauch, and D. Budker, “Optical properties of the nitrogen-vacancy singlet levels in diamond,” *Physical Review B* **82**, 201202 (2010).

## Bibliography

- [80] M. L. Goldman, A. Sipahigil, M. Doherty, N. Y. Yao, S. Bennett, M. Markham, D. Twitchen, N. Manson, A. Kubanek, and M. D. Lukin, “Phonon-induced population dynamics and intersystem crossing in nitrogen-vacancy centers,” *Physical Review Letters* **114**, 145502 (2015).
- [81] G. Fuchs, V. Dobrovitski, D. Toyli, F. Heremans, C. Weis, T. Schenkel, and D. Awschalom, “Excited-state spin coherence of a single nitrogen–vacancy centre in diamond,” *Nature Physics* **6**, 668–672 (2010).
- [82] L. Robledo, H. Bernien, T. Van Der Sar, and R. Hanson, “Spin dynamics in the optical cycle of single nitrogen-vacancy centres in diamond,” *New Journal of Physics* **13**, 025013 (2011).
- [83] J. Tetienne, L. Rondin, P. Spinicelli, M. Chipaux, T. Debuisschert, J. Roch, and V. Jacques, “Magnetic-field-dependent photodynamics of single NV defects in diamond: an application to qualitative all-optical magnetic imaging,” *New Journal of Physics* **14**, 103033 (2012).
- [84] M. L. Goldman, M. Doherty, A. Sipahigil, N. Y. Yao, S. Bennett, N. Manson, A. Kubanek, and M. D. Lukin, “State-selective intersystem crossing in nitrogen-vacancy centers,” *Physical Review B* **91**, 165201 (2015).
- [85] E. Janitz, K. Herb, L. A. Völker, W. S. Huxter, C. L. Degen, and J. M. Abendroth, “Diamond surface engineering for molecular sensing with nitrogen-vacancy centers,” *Journal of Materials Chemistry C* **10**, 13533–13569 (2022).
- [86] A. Ariyaratne, D. Bluvstein, B. A. Myers, and A. C. B. Jayich, “Nanoscale electrical conductivity imaging using a nitrogen-vacancy center in diamond,” *Nature Communications* **9**, 1–7 (2018).
- [87] 김갑진, *마법에서 과학으로 : 자석과 스핀트로닉스* (이음, 2021) ISBN: 9791190944311.
- [88] M. Lee, J. Yoon, and D. Lee, *Atomic Scale Magnetic Sensing and Imaging Based on Diamond NV Centers* (Magnetometers - Fundamentals and Applications of Magnetism, 2019, ISBN: 9781839690969).
- [89] D. M. Louzon, *Implementation of control sequences for robust quantum sensing with a solid state qubit*, Ph.D. dissertation, Ulm University (2021).
- [90] H. Clevenson, M. E. Trusheim, C. Teale, T. Schröder, D. Braje, and D. Englund, “Broadband magnetometry and temperature sensing with a light-trapping diamond waveguide,” *Nature Physics* **11**, 393–397 (2015).

- [91] H. Zhou, J. Choi, S. Choi, R. Landig, A. M. Douglas, J. Isoya, F. Jelezko, S. Onoda, H. Sumiya, P. Cappellaro, H. S. Knowles, H. Park, and M. D. Lukin, “Quantum metrology with strongly interacting spin systems,” *Physical Review X* **10**, 031003 (2020).
- [92] M. A. Nielsen and I. Chuang, *Quantum computation and quantum information* (Cambridge University Press, 2010) ISBN: 9781107002173.
- [93] M.-S. Choi, *A Quantum Computation Workbook* (Springer, GitHub: [QuantumWorkbook](#), 2022) ISBN: 9783030912130.
- [94] S. Felton, A. Edmonds, M. Newton, P. Martineau, D. Fisher, D. Twitchen, and J. Baker, “Hyperfine interaction in the ground state of the negatively charged nitrogen vacancy center in diamond,” *Physical Review B* **79**, 075203 (2009).
- [95] L. Childress, M. G. Dutt, J. Taylor, A. Zibrov, F. Jelezko, J. Wrachtrup, P. Hemmer, and M. Lukin, “Coherent dynamics of coupled electron and nuclear spin qubits in diamond,” *Science* **314**, 281–285 (2006).
- [96] D. Paone, *Nanoscale magnetic resonance spectroscopy with Nitrogen-Vacancy centers in diamond*, Ph.D. dissertation, University of Stuttgart (2021).
- [97] B. A. Myers, *Quantum Decoherence of Near-Surface Nitrogen-Vacancy Centers in Diamond and Implications for Nanoscale Imaging*, Ph.D. dissertation, University of California Santa Barbara (2016), issue: September.
- [98] A. Gruber, A. Drabenstedt, C. Tietz, L. Fleury, J. Wrachtrup, and C. Von Borczyskowski, “Scanning confocal optical microscopy and magnetic resonance on single defect centers,” *Science* **276**, 2012–2014 (1997).
- [99] T. X. Zhou, R. J. Stöhr, and A. Yacoby, “Scanning diamond nv center probes compatible with conventional afm technology,” *Applied Physics Letters* **111**, 163106 (2017).
- [100] M. Lee, B. Jang, J. Yoon, M. C. Mathpal, Y. Lee, C. Kim, S. Pane, B. J. Nelson, and D. Lee, “Magnetic imaging of a single ferromagnetic nanowire using diamond atomic sensors,” *Nanotechnology* **29**, 405502 (2018).
- [101] L.-A. T. Nguyen, K. P. Dhakal, Y. Lee, W. Choi, T. D. Nguyen, C. Hong, D. H. Luong, Y.-M. Kim, J. Kim, M. Lee, T. Choi, A. J. Heinrich, J.-H. Kim, D. Lee, D. L. Duong, and Y. H. Lee, “Spin-selective hole–exciton coupling in a V-doped WSe<sub>2</sub> ferromagnetic semiconductor at room temperature,” *ACS Nano* **15**, 20267–20277 (2021).
- [102] J. M. McCoe, R. W. de Gille, B. Nasr, J.-P. Tetienne, L. T. Hall, D. A. Simpson, and L. C. Hollenberg, “Rapid, high-resolution magnetic microscopy of single magnetic

## Bibliography

- microbeads,” *Small* **15**, 1805159 (2019).
- [103] J. Yoon, J. H. Moon, J. Chung, Y. J. Kim, K. Kim, H. S. Kang, Y. S. Jeon, E. Oh, S. H. Lee, K. Han, D. Lee, C.-H. Lee, Y. K. Kim, and D. Lee, “Exploring the magnetic properties of individual barcode nanowires using wide-field diamond microscopy,” *Small* **19**, 2304129 (2023).
- [104] M. Lee, S. Jang, W. Jung, Y. Lee, T. Taniguchi, K. Watanabe, H.-R. Kim, H.-G. Park, G.-H. Lee, and D. Lee, “Mapping current profiles of point-contacted graphene devices using single-spin scanning magnetometer,” *Applied Physics Letters* **118**, 033101 (2021).
- [105] L. Rondin, J.-P. Tetienne, P. Spinicelli, C. Dal Savio, K. Karrai, G. Dantelle, A. Thiaville, S. Rohart, J.-F. Roch, and V. Jacques, “Nanoscale magnetic field mapping with a single spin scanning probe magnetometer,” *Applied Physics Letters* **100**, 153118 (2012).
- [106] Y. Lee, M. Lee, J. Jo, S. Lee, J.-W. Yoo, T. Choi, A. Heinrich, and D. Lee, “Imaging oersted field around current flowing wire based on a diamond scanning magnetometer,” *Current Applied Physics* **34**, 59–63 (2022).
- [107] M. Pelliccione, B. A. Myers, L. Pascal, A. Das, and A. B. Jayich, “Two-dimensional nanoscale imaging of gadolinium spins via scanning probe relaxometry with a single spin in diamond,” *Physical Review Applied* **2**, 054014 (2014).
- [108] M. Pelliccione, *Local Imaging of High Mobility Two-Dimensional Electron Systems With Virtual Scanning Tunneling Microscopy*, Ph.D. dissertation, Stanford University (2013).
- [109] D. Lee, *Atomic Scale Gate Electrode Formed by a Charged Defect: Scanning Tunneling Microscopy of Single Impurities in GaAs Semiconductors*, Ph.D. dissertation, The Ohio State University (2010).
- [110] A. Jenkins, *Probing Condensed Matter Order with Nitrogen-Vacancy Center Scanning Magnetometry*, Ph.D. dissertation, University of California Santa Barbara (2019).
- [111] Qnami, (Switzerland), [Qnami.ch](https://qnami.ch).
- [112] QZabre, (Switzerland), [QZabre.com](https://qzabre.com).
- [113] J. Dargan, “Experts in Nitrogen Vacancy are Enabling Breakthroughs in High Res & Passive Magnetic Analysis,” *The Quantum Insider* (2021).
- [114] K. Karrai and R. D. Grober, “Piezoelectric tip-sample distance control for near field optical microscopes,” *Applied Physics Letters* **66**, 1842–1844 (1995).

- [115] Y. Qin, *Interaction force microscopy based on quartz tuning fork force sensor*, Ph.D. dissertation, Purdue University (2007).
- [116] J. Liu, A. Callegari, M. Stark, and M. Chergui, “A simple and accurate method for calibrating the oscillation amplitude of tuning-fork based afm sensors,” *Ultramicroscopy* **109**, 81–84 (2008).
- [117] *CAS - CERN Accelerator School : Vacuum Technology* (1999).
- [118] B. Baudouy, “Heat transfer and cooling techniques at low temperature,” *CAS - CERN Accelerator School: Superconductivity for Accelerators*, 329–352 (2015).
- [119] M. S. Salem, P. Sergelius, R. M. Corona, J. Escrig, D. Görlitz, and K. Nielsch, “Magnetic properties of cylindrical diameter modulated Ni<sub>80</sub>Fe<sub>20</sub> nanowires: interaction and coercive fields,” *Nanoscale* **5**, 3941–3947 (2013).
- [120] D. A. Allwood, G. Xiong, C. Faulkner, D. Atkinson, D. Petit, and R. Cowburn, “Magnetic domain-wall logic,” *Science* **309**, 1688–1692 (2005).
- [121] R. L. Stamps, S. Breitkreutz, J. Åkerman, A. V. Chumak, Y. Otani, G. E. W. Bauer, J.-U. Thiele, M. Bowen, S. A. Majetich, M. Kläui, I. L. Prejbeanu, B. Dieny, N. M. Dempsey, and B. Hillebrands, “The 2014 magnetism roadmap,” *Journal of Physics D: Applied Physics* **47**, 333001 (2014).
- [122] V. Nguyen, O. Fruchart, S. Pizzini, J. Vogel, J.-C. Toussaint, and N. Rougemaille, “Third type of domain wall in soft magnetic nanostrips,” *Scientific Reports* **5**, 1–7 (2015).
- [123] D. J. Lee, E. Kim, D. Kim, J. Park, and S. Hong, “Nano-storage wires,” *ACS nano* **7**, 6906–6913 (2013).
- [124] B. Jang, E. Gutman, N. Stucki, B. F. Seitz, P. D. Wendel-García, T. Newton, J. Pokki, O. Ergeneman, S. Pané, Y. Or, and B. J. Nelson, “Undulatory locomotion of magnetic multilink nanoswimmers,” *Nano Letters* **15**, 4829–4833 (2015).
- [125] C. Hu, S. Pané, and B. J. Nelson, “Soft micro-and nanorobotics,” *Annual Review of Control, Robotics, and Autonomous Systems* **1**, 53–75 (2018).
- [126] X.-Z. Chen, M. Hoop, F. Mushtaq, E. Siringil, C. Hu, B. J. Nelson, and S. Pané, “Recent developments in magnetically driven micro-and nanorobots,” *Applied Materials Today* **9**, 37–48 (2017).
- [127] X.-Z. Chen, B. Jang, D. Ahmed, C. Hu, C. De Marco, M. Hoop, F. Mushtaq, B. J. Nelson, and S. Pané, “Small-scale machines driven by external power sources,” *Advanced Materials* **30**, 1705061 (2018).

## Bibliography

- [128] R. Hertel and J. Kirschner, “Magnetization reversal dynamics in nickel nanowires,” *Physica B: Condensed Matter* **343**, 206–210 (2004).
- [129] R. Wieser, E. Vedmedenko, P. Weinberger, and R. Wiesendanger, “Current-driven domain wall motion in cylindrical nanowires,” *Physical Review B* **82**, 144430 (2010).
- [130] C. Bran, J. A. Fernandez-Roldan, E. M. Palmero, E. Berganza, J. Guzman, R. P. del Real, A. Asenjo, A. Fraile Rodríguez, M. Foerster, L. Aballe, O. Chubykalo-Fesenko, and M. Vazquez, “Direct observation of transverse and vortex metastable magnetic domains in cylindrical nanowires,” *Physical Review B* **96**, 125415 (2017).
- [131] M. Yan, A. Kákay, S. Gliga, and R. Hertel, “Beating the walker limit with massless domain walls in cylindrical nanowires,” *Physical Review Letters* **104**, 057201 (2010).
- [132] D. Petit, A.-V. Jausovec, H. T. Zeng, E. Lewis, L. O’Brien, D. Read, and R. P. Cowburn, “Mechanism for domain wall pinning and potential landscape modification by artificially patterned traps in ferromagnetic nanowires,” *Physical Review B* **79**, 214405 (2009).
- [133] D. Chiba, M. Kawaguchi, S. Fukami, N. Ishiwata, K. Shimamura, K. Kobayashi, and T. Ono, “Electric-field control of magnetic domain-wall velocity in ultrathin cobalt with perpendicular magnetization,” *Nature Communications* **3**, 1–7 (2012).
- [134] W. Jiang, P. Upadhyaya, W. Zhang, G. Yu, M. B. Jungfleisch, F. Y. Fradin, J. E. Pearson, Y. Tserkovnyak, K. L. Wang, O. Heinonen, S. G. E. te Velthuis, and A. Hoffmann, “Blowing magnetic skyrmion bubbles,” *Science* **349**, 283–286 (2015).
- [135] J. Garcia, A. Thiaville, and J. Miltat, “MFM imaging of nanowires and elongated patterned elements,” *Journal of Magnetism and Magnetic Materials* **249**, 163–169 (2002).
- [136] J. Gartside, D. Burn, L. Cohen, and W. Branford, “A novel method for the injection and manipulation of magnetic charge states in nanostructures,” *Scientific Reports* **6**, 1–9 (2016).
- [137] Y. P. Ivanov, A. Alfadhel, M. Alnassar, J. E. Perez, M. Vazquez, A. Chuvilin, and J. Kosel, “Tunable magnetic nanowires for biomedical and harsh environment applications,” *Scientific Reports* **6**, 1–10 (2016).
- [138] L. P. McGuinness, Y. Yan, A. Stacey, D. A. Simpson, L. T. Hall, D. Maclaurin, S. Praver, P. Mulvaney, J. Wrachtrup, F. Caruso, R. E. Scholten, and L. C. L. Hollenberg, “Quantum measurement and orientation tracking of fluorescent nanodiamonds inside living cells,” *Nature Nanotechnology* **6**, 358–363 (2011).
- [139] L. M. Pham, D. L. Sage, P. L. Stanwix, T. K. Yeung, D. Glenn, A. Trifonov, P. Cap-

- pellaro, P. R. Hemmer, M. D. Lukin, H. Park, A. Yacoby, and R. L. Walsworth, “Magnetic field imaging with nitrogen-vacancy ensembles,” *New Journal of Physics* **13**, 045021 (2011).
- [140] I. Lovchinsky, A. O. Sushkov, E. Urbach, N. P. de Leon, S. Choi, K. D. Greve, R. Evans, R. Gertner, E. Bersin, C. Müller, L. McGuinness, F. Jelezko, R. L. Walsworth, H. Park, and M. D. Lukin, “Nuclear magnetic resonance detection and spectroscopy of single proteins using quantum logic,” *Science* **351**, 836–841 (2016).
- [141] M. J. Donahue and D. G. Porter, *OOMMF User’s Guide, Version 1.0* (Interagency Report NISTIR 6376, National Institute of Standards and Technology Gaithersburg, MD, 1999).
- [142] E. Völkl, L. F. Allard, and D. C. Joy, *Introduction to electron holography* (Springer US, 1999) ISBN: 9780306449208.
- [143] J. Cantu-Valle, I. Betancourt, J. E. Sanchez, F. Ruiz-Zepeda, M. M. Maqableh, F. Mendoza-Santoyo, B. J. Stadler, and A. Ponce, “Mapping the magnetic and crystal structure in cobalt nanowires,” *Journal of Applied Physics* **118**, 024302 (2015).
- [144] P. C. Maurer, G. Kucsko, C. Latta, L. Jiang, N. Y. Yao, S. D. Bennett, F. Pastawski, D. Hunger, N. Chisholm, M. Markham, D. J. Twitchen, J. I. Cirac, and M. D. Lukin, “Room-temperature quantum bit memory exceeding one second,” *Science* **336**, 1283–1286 (2012).
- [145] N. Bar-Gill, L. M. Pham, A. Jarmola, D. Budker, and R. L. Walsworth, “Solid-state electronic spin coherence time approaching one second,” *Nature Communications* **4**, 1–6 (2013).
- [146] T. Taychatanapat, K. Watanabe, T. Taniguchi, and P. Jarillo-Herrero, “Electrically tunable transverse magnetic focusing in graphene,” *Nature Physics* **9**, 225–229 (2013).
- [147] G.-H. Lee, G.-H. Park, and H.-J. Lee, “Observation of negative refraction of dirac fermions in graphene,” *Nature Physics* **11**, 925–929 (2015).
- [148] R. Krishna Kumar, D. A. Bandurin, F. M. D. Pellegrino, Y. Cao, A. Principi, H. Guo, G. H. Auton, M. Ben Shalom, L. A. Ponomarenko, G. Falkovich, K. Watanabe, T. Taniguchi, I. V. Grigorieva, L. S. Levitov, M. Polini, and A. K. Geim, “Superballistic flow of viscous electron fluid through graphene constrictions,” *Nature Physics* **13**, 1182–1185 (2017).
- [149] L. Levitov and G. Falkovich, “Electron viscosity, current vortices and negative non-local resistance in graphene,” *Nature Physics* **12**, 672–676 (2016).

## Bibliography

- [150] M. J. H. Ku, T. X. Zhou, Q. Li, Y. J. Shin, J. K. Shi, C. Burch, L. E. Anderson, A. T. Pierce, Y. Xie, A. Hamo, U. Vool, H. Zhang, F. Casola, T. Taniguchi, K. Watanabe, M. M. Fogler, P. Kim, A. Yacoby, and R. L. Walsworth, “Imaging viscous flow of the dirac fluid in graphene,” *Nature* **583**, 537–541 (2020).
- [151] A. Jenkins, S. Baumann, H. Zhou, S. A. Meynell, Y. Daipeng, K. Watanabe, T. Taniguchi, A. Lucas, A. F. Young, and A. C. B. Jayich, “Imaging the breakdown of ohmic transport in graphene,” *Physical Review Letters* **129**, 087701 (2022).
- [152] V. V. Cheianov, V. Fal’ko, and B. Altshuler, “The focusing of electron flow and a veselago lens in graphene p-n junctions,” *Science* **315**, 1252–1255 (2007).
- [153] P. Rickhaus, P. Makk, M.-H. Liu, E. Tóvári, M. Weiss, R. Maurand, K. Richter, and C. Schönberger, “Snake trajectories in ultraclean graphene p–n junctions,” *Nature Communications* **6**, 1–6 (2015).
- [154] M.-H. Liu, C. Gorini, and K. Richter, “Creating and steering highly directional electron beams in graphene,” *Physical Review Letters* **118**, 066801 (2017).
- [155] P. Bøggild, J. M. Caridad, C. Stampfer, G. Calogero, N. R. Papior, and M. Brandbyge, “A two-dimensional dirac fermion microscope,” *Nature Communications* **8**, 1–12 (2017).
- [156] C. W. J. Beenakker, “Specular andreev reflection in graphene,” *Physical Review Letters* **97**, 067007 (2006).
- [157] S. Bhandari, G.-H. Lee, A. Klales, K. Watanabe, T. Taniguchi, E. Heller, P. Kim, and R. M. Westervelt, “Imaging cyclotron orbits of electrons in graphene,” *Nano Letters* **16**, 1690–1694 (2016).
- [158] L. Ella, A. Rozen, J. Birkbeck, M. Ben-Shalom, D. Perello, J. Zultak, T. Taniguchi, K. Watanabe, A. K. Geim, S. Ilani, and J. A. Sulpizio, “Simultaneous voltage and current density imaging of flowing electrons in two dimensions,” *Nature Nanotechnology* **14**, 480–487 (2019).
- [159] C. Handschin, B. Fülöp, P. Makk, S. Blanter, M. Weiss, K. Watanabe, T. Taniguchi, S. Csonka, and C. Schönberger, “Point contacts in encapsulated graphene,” *Applied Physics Letters* **107**, 183108 (2015).
- [160] L. Wang, I. Meric, P. Y. Huang, Q. Gao, Y. Gao, H. Tran, T. Taniguchi, K. Watanabe, L. M. Campos, D. A. Muller, J. Guo, P. Kim, J. Hone, K. L. Shepard, and C. R. Dean, “One-dimensional electrical contact to a two-dimensional material,” *Science* **342**, 614–617 (2013).

- [161] J.-P. Tetienne, N. Dontschuk, D. A. Broadway, A. Stacey, D. A. Simpson, and L. C. Hollenberg, “Quantum imaging of current flow in graphene,” *Science Advances* **3**, e1602429 (2017).
- [162] K. Chang, A. Eichler, J. Rhensius, L. Lorenzelli, and C. L. Degen, “Nanoscale imaging of current density with a single-spin magnetometer,” *Nano Letters* **17**, 2367–2373 (2017).
- [163] L. Thiel, *Nanoscale Magnetometry with a Single Spin in Diamond at Cryogenic Temperatures*, Ph.D. dissertation, Universität Basel (2019).
- [164] D. Broadway, S. Lillie, S. C. Scholten, D. Rohner, N. Dontschuk, P. Maletinsky, J.-P. Tetienne, and L. Hollenberg, “Improved current density and magnetization reconstruction through vector magnetic field measurements,” *Physical Review Applied* **14**, 024076 (2020).
- [165] B. J. Roth, N. G. Sepulveda, and J. P. Wikswo Jr, “Using a magnetometer to image a two-dimensional current distribution,” *Journal of applied physics* **65**, 361–372 (1989).
- [166] S.-i. Tanaka, “Longitudinal kerr magneto-optic effect in permalloy film,” *Japanese Journal of Applied Physics* **2**, 548 (1963).
- [167] R. Badea, J. A. Frey, and J. Berezovsky, “Magneto-optical imaging of vortex domain deformation in pinning sites,” *Journal of Magnetism and Magnetic Materials* **381**, 463–469 (2015).
- [168] D. Allwood, G. Xiong, M. Cooke, and R. Cowburn, “Magneto-optical Kerr effect analysis of magnetic nanostructures,” *Journal of Physics D: Applied Physics* **36**, 2175 (2003).
- [169] J. Raabe, C. Quitmann, C. Back, F. Nolting, S. Johnson, and C. Buehler, “Quantitative analysis of magnetic excitations in Landau flux-closure structures using synchrotron-radiation microscopy,” *Physical Review Letters* **94**, 217204 (2005).
- [170] M. Bolte, G. Meier, B. Krüger, A. Drews, R. Eiselt, L. Bocklage, S. Bohlens, T. Tylizszczak, A. Vansteenkiste, B. Van Waeyenberge, K. W. Chou, A. Puzic, and H. Stoll, “Time-resolved X-ray microscopy of spin-torque-induced magnetic vortex gyration,” *Physical Review Letters* **100**, 176601 (2008).
- [171] L. Ramasubramanian, A. Kákay, C. Fowley, O. Yildirim, P. Matthes, S. Sorokin, A. Titova, D. Hilliard, R. Böttger, R. Hübner, S. Gemming, S. E. Schulz, F. Kronast, D. Makarov, J. Fassbender, and A. Deac, “Tunable magnetic vortex dynamics in ion-implanted permalloy disks,” *ACS Applied Materials & Interfaces* **12**, 27812–27818

## Bibliography

- (2020).
- [172] T. Okuno, K. Shigeto, T. Ono, K. Mibu, and T. Shinjo, “MFM study of magnetic vortex cores in circular permalloy dots: behavior in external field,” *Journal of Magnetism and Magnetic Materials* **240**, 1–6 (2002).
- [173] T. Morooka, S. Nakayama, A. Odawara, M. Ikeda, S. Tanaka, and K. Chinone, “Micro-imaging system using scanning DC-SQUID microscope,” *IEEE Transactions on Applied Superconductivity* **9**, 3491–3494 (1999).
- [174] M. Ketchen, “Integrated thin-film dc SQUID sensors,” *IEEE Transactions on Magnetism* **23**, 1650–1657 (1987).
- [175] L. Rondin, J.-P. Tetienne, S. Rohart, A. Thiaville, T. Hingant, P. Spinicelli, J.-F. Roch, and V. Jacques, “Stray-field imaging of magnetic vortices with a single diamond spin,” *Nature Communications* **4**, 1–5 (2013).
- [176] J.-P. Tetienne, T. Hingant, L. Rondin, S. Rohart, A. Thiaville, J.-F. Roch, and V. Jacques, “Quantitative stray field imaging of a magnetic vortex core,” *Physical Review B* **88**, 214408 (2013).
- [177] T. Van der Sar, F. Casola, R. Walsworth, and A. Yacoby, “Nanometre-scale probing of spin waves using single electron spins,” *Nature Communications* **6**, 1–8 (2015).
- [178] M.-Y. Im, H.-S. Han, M.-S. Jung, Y.-S. Yu, S. Lee, S. Yoon, W. Chao, P. Fischer, J.-I. Hong, and K.-S. Lee, “Dynamics of the Bloch point in an asymmetric permalloy disk,” *Nature Communications* **10**, 1–8 (2019).
- [179] A. A. Thiele, “Steady-state motion of magnetic domains,” *Physical Review Letters* **30**, 230 (1973).
- [180] D. Kumar and A. Adeyeye, “Techniques in micromagnetic simulation and analysis,” *Journal of Physics D: Applied Physics* **50**, 343001 (2017).
- [181] M. S. Wolf, R. Badea, and J. Berezovsky, “Fast nanoscale addressability of nitrogen-vacancy spins via coupling to a dynamic ferromagnetic vortex,” *Nature Communications* **7**, 1–7 (2016).
- [182] C. Purser, V. Bhallamudi, C. Wolfe, H. Yusuf, B. McCullian, C. Jayaprakash, M. Flatté, and P. Hammel, “Broadband electron paramagnetic resonance spectroscopy in diverse field conditions using optically detected nitrogen-vacancy centers in diamond,” *Journal of Physics D: Applied Physics* **52**, 305004 (2019).
- [183] M. R. Page, B. A. McCullian, C. M. Purser, J. G. Schulze, T. M. Nakatani, C. S. Wolfe, J. R. Childress, M. E. McConney, B. M. Howe, P. C. Hammel, and V. P. Bhallamudi,

- “Optically detected ferromagnetic resonance in diverse ferromagnets via nitrogen vacancy centers in diamond,” *Journal of Applied Physics* **126**, 124902 (2019).
- [184] P. Wang, Z. Yuan, P. Huang, X. Rong, M. Wang, X. Xu, C. Duan, C. Ju, F. Shi, and J. Du, “High-resolution vector microwave magnetometry based on solid-state spins in diamond,” *Nature Communications* **6**, 1–5 (2015).
- [185] C. Mu, J. Jing, J. Dong, W. Wang, J. Xu, A. Nie, J. Xiang, F. Wen, and Z. Liu, “Static and dynamic characteristics of magnetism in permalloy oval nanoring by micromagnetic simulation,” *Journal of Magnetism and Magnetic Materials* **474**, 301–304 (2019).
- [186] I. Gross, W. Akhtar, V. Garcia, L. J. Martínez, S. Chouaieb, K. Garcia, C. Carretéro, A. Barthélémy, P. Appel, P. Maletinsky, J.-V. Kim, J. Y. Chauleau, N. Jaouen, M. Viret, M. Bibes, S. Fusil, and V. Jacques, “Real-space imaging of non-collinear antiferromagnetic order with a single-spin magnetometer,” *Nature* **549**, 252–256 (2017).
- [187] A. Dréau, M. Lesik, L. Rondin, P. Spinicelli, O. Arcizet, J.-F. Roch, and V. Jacques, “Avoiding power broadening in optically detected magnetic resonance of single NV defects for enhanced dc magnetic field sensitivity,” *Physical Review B* **84**, 195204 (2011).
- [188] Y. Xu, Y. Yu, Y. Y. Hui, Y. Su, J. Cheng, H.-C. Chang, Y. Zhang, Y. R. Shen, and C. Tian, “Mapping dynamical magnetic responses of ultrathin micron-size superconducting films using nitrogen-vacancy centers in diamond,” *Nano Letters* **19**, 5697–5702 (2019).
- [189] D. R. Candido, G. D. Fuchs, E. Johnston-Halperin, and M. E. Flatté, “Predicted strong coupling of solid-state spins via a single magnon mode,” *Materials for Quantum Technology* **1**, 011001 (2020).
- [190] P. Appel, M. Ganzhorn, E. Neu, and P. Maletinsky, “Nanoscale microwave imaging with a single electron spin in diamond,” *New Journal of Physics* **17**, 112001 (2015).
- [191] D. Kikuchi, D. Prananto, K. Hayashi, A. Laraoui, N. Mizuochi, M. Hatano, E. Saitoh, Y. Kim, C. A. Meriles, and T. An, “Long-distance excitation of nitrogen-vacancy centers in diamond via surface spin waves,” *Applied Physics Express* **10**, 103004 (2017).
- [192] M. Fukami, D. R. Candido, D. D. Awschalom, and M. E. Flatté, “Opportunities for long-range magnon-mediated entanglement of spin qubits via on-and off-resonant coupling,” *PRX Quantum* **2**, 040314 (2021).
- [193] E. Lee-Wong, R. Xue, F. Ye, A. Kreisel, T. van Der Sar, A. Yacoby, and C. R.

## Bibliography

- Du, “Nanoscale detection of magnon excitations with variable wavevectors through a quantum spin sensor,” *Nano Letters* **20**, 3284–3290 (2020).
- [194] T. X. Zhou, J. J. Carmiggelt, L. M. Gächter, I. Esterlis, D. Sels, R. J. Stöhr, C. Du, D. Fernandez, J. F. Rodriguez-Nieva, F. Büttner, *et al.*, “A magnon scattering platform,” *Proceedings of the National Academy of Sciences* **118**, e2019473118 (2021).
- [195] U. Vool, A. Hamo, G. Varnavides, Y. Wang, T. X. Zhou, N. Kumar, Y. Dovzhenko, Z. Qiu, C. A. C. Garcia, A. T. Pierce, J. Gooth, P. Anikeeva, C. Felser, P. Narang, and A. Yacoby, “Imaging phonon-mediated hydrodynamic flow in WTe<sub>2</sub>,” *Nature Physics* **17**, 1216–1220 (2021).
- [196] D. Ghodgaonkar, V. Varadan, and V. K. Varadan, “Free-space measurement of complex permittivity and complex permeability of magnetic materials at microwave frequencies,” *IEEE Transactions on Instrumentation and Measurement* **39**, 387–394 (1990).
- [197] V. Korenivski and R. Van Dover, “Magnetic film inductors for radio frequency applications,” *Journal of Applied Physics* **82**, 5247–5254 (1997).
- [198] P. Saville, *Review of radar absorbing materials*, Tech. Rep. (Defence Research and Development Atlantic Dartmouth (Canada), 2005).
- [199] D. Lee, K. W. Lee, J. V. Cady, P. Ovarthaiyapong, and A. C. B. Jayich, “Topical review: spins and mechanics in diamond,” *Journal of Optics* **19**, 033001 (2017).

# Appendix A

## Spin Operator Calculation

In this appendix, spin operators are defined and how to calculate time evolution of spin in rotation frame (interaction picture) is discussed. In particular, we focus on the spin triplet, which is the NV center ground state discussed in Section 2.2.

### A.1 Spin operator definitions

For spin  $\frac{1}{2}$ , spin operator are defined by

$$\begin{aligned} S_x &= \frac{1}{2} \begin{pmatrix} 0 & 1 \\ 1 & 0 \end{pmatrix}, S_y = \frac{1}{2} \begin{pmatrix} 0 & 1 \\ -1 & 0 \end{pmatrix}, S_z = \frac{1}{2} \begin{pmatrix} 1 & 0 \\ 0 & 1 \end{pmatrix}, \\ S_+ &= \begin{pmatrix} 0 & 1 \\ 0 & 0 \end{pmatrix}, S_- = \begin{pmatrix} 0 & 0 \\ 1 & 0 \end{pmatrix}. \end{aligned} \tag{A.1}$$

## Appendix A. Spin Operator Calculation

For spin 1, spin operators are defined by

$$\begin{aligned}
 S_x &= \frac{1}{\sqrt{2}} \begin{pmatrix} 0 & 1 & 0 \\ 1 & 0 & 1 \\ 0 & 1 & 0 \end{pmatrix}, \quad S_y = \frac{1}{\sqrt{2}} \begin{pmatrix} 0 & -i & 0 \\ i & 0 & -i \\ 0 & i & 0 \end{pmatrix}, \quad S_z = \begin{pmatrix} 1 & 0 & 0 \\ 0 & 0 & 0 \\ 0 & 0 & -1 \end{pmatrix}, \\
 S_+ &= \begin{pmatrix} 0 & \sqrt{2} & 0 \\ 0 & 0 & \sqrt{2} \\ 0 & 0 & 0 \end{pmatrix}, \quad S_- = \begin{pmatrix} 0 & 0 & 0 \\ \sqrt{2} & 0 & 0 \\ 0 & \sqrt{2} & 0 \end{pmatrix}.
 \end{aligned} \tag{A.2}$$

### A.2 Rotating frame calculation

We can simply pick two level for matching microwave frequency to one on NV ground state energy level with

$$\begin{aligned}
 \hat{H}/h &= D_0 \hat{S}_z^2 + \gamma_e B_z \hat{S}_z + \gamma_e B_x \hat{S}_x \cos(\omega t + \varphi) \\
 &= D_0 \left( \begin{array}{c|c} 1 & \\ \hline 0 & \\ \hline & 1 \end{array} \right) + \gamma_e B_z \left( \begin{array}{c|c} 1 & \\ \hline 0 & \\ \hline & -1 \end{array} \right) + \gamma_e B_x \frac{1}{\sqrt{2}} \left( \begin{array}{c|c} 1 & \\ \hline 1 & 1 \\ \hline & 1 \end{array} \right) \cos(\omega t + \varphi)
 \end{aligned} \tag{A.3}$$

, when  $\omega \simeq D_0 + \gamma_e B_z$ ,  $2 \times 2$  block matrix can be used. So, this Hamiltonian can be written with

$$\begin{aligned}
 \hat{H}/h &= D_0 \begin{pmatrix} 1 & \\ & 0 \end{pmatrix} + \gamma_e B_z \begin{pmatrix} 1 & \\ & 0 \end{pmatrix} + \frac{\gamma_e B_x}{\sqrt{2}} \begin{pmatrix} & 1 \\ 1 & \end{pmatrix} \cos(\omega t + \varphi) \\
 &= \frac{D_0 + \gamma_e B_z}{2} \sigma_0 + \frac{D_0 + \gamma_e B_z}{2} \sigma_z + \frac{\gamma_e B_x}{\sqrt{2}} \sigma_x \cos(\omega t + \varphi)
 \end{aligned} \tag{A.4}$$

, where the identity matrix  $\sigma_0$  of the first term can be ignored, and the other terms are similar form with Equation 2.8. In this appendix section, it will be described how to change this with

the interaction picture. We can choose  $H_0/\hbar = \omega\hat{S}_z^2$  in Equation A.3. So, we can take

$$\begin{aligned}
\hat{H}/\hbar &= \begin{pmatrix} 2\pi D_0 + \gamma_e B_z - \omega & & \\ & 0 & \\ & & 2\pi D_0 - \gamma_e B_z - \omega \end{pmatrix} + 2\pi\gamma_e B_x \hat{S}_x \cos(\omega + \varphi) \\
&= \underbrace{\begin{pmatrix} \omega & & \\ & 0 & \\ & & \omega \end{pmatrix}}_{\hat{H}_0/\hbar} + \underbrace{\begin{pmatrix} \omega_1 - \omega & & \\ & 0 & \\ & & \omega_{-1} - \omega \end{pmatrix}}_{\hat{H}_1/\hbar} + 2\pi\gamma_e B_x \hat{S}_x \cos(\omega + \varphi), \\
\hat{U} = e^{-i\hat{H}_0 t/\hbar} &= \begin{pmatrix} e^{-i\omega t} & & \\ & 1 & \\ & & e^{-i\omega t} \end{pmatrix}
\end{aligned} \tag{A.5}$$

, where  $\omega_1 = 2\pi(D_0 + \gamma_e B_z)$ , and  $\omega_{-1} = 2\pi(D_0 - \gamma_e B_z)$ . Using this equation, interaction Hamiltonian described by

$$\begin{aligned}
\hat{H}_I/\hbar &= \hat{U}^\dagger \hat{H}_1 \hat{U}/\hbar \\
&= \begin{pmatrix} \omega_1 - \omega & & \\ & 0 & \\ & & \omega_{-1} - \omega \end{pmatrix} + 2\pi\gamma_e B_x \frac{1}{\sqrt{2}} \begin{pmatrix} e^{+i\omega t} & & \\ e^{-i\omega t} & & e^{-i\omega t} \\ & e^{+i\omega t} & \end{pmatrix} \cos(\omega t + \varphi).
\end{aligned} \tag{A.6}$$

Sinusoidal terms are simplified by

$$\begin{aligned}
e^{\pm i\omega t} \cos(\omega t + \varphi) &= (\cos \omega t \pm i \sin \omega t)(\cos \omega t \cos \varphi - \sin \omega t \sin \varphi) \\
&= \cos \varphi \underbrace{\cos^2 \omega t}_{\frac{1}{2} + \frac{1}{2} \cos 2\omega t} \mp i \sin \varphi \underbrace{\sin^2 \omega t}_{\frac{1}{2} - \frac{1}{2} \cos 2\omega t} + (\pm i \cos \varphi - \sin \varphi) \underbrace{\cos \omega t \sin \omega t}_{\frac{1}{2} \sin 2\omega t} \\
&= \frac{1}{2}(\cos \varphi \mp i \sin \varphi) = \frac{1}{2}e^{-i\varphi}
\end{aligned} \tag{A.7}$$

## Appendix A. Spin Operator Calculation

, where trigonometric function with  $2\omega t$  terms are ignored in rotating wave approximation regime  $2\omega \gg \omega_1 - \omega$ , and the transition between 1 and 0 is dominant in  $\omega_1 - \omega \ll \omega_{-1} - \omega$ . The interaction Hamiltonian is simplified by

$$\hat{H}_I/\hbar = \begin{pmatrix} \omega_1 - \omega & & \\ & 0 & \\ & & \omega_{-1} - \omega \end{pmatrix} + 2\pi\gamma_e B_x \frac{1}{2\sqrt{2}} \begin{pmatrix} & e^{-i\varphi} & \\ e^{+i\varphi} & & \\ & e^{-i\varphi} & \end{pmatrix}. \quad (\text{A.8})$$

From that, we can choose  $2 \times 2$  matrix describe in Equation [A.3](#).

## Appendix B

# Magnetic Field Decomposition and Current Reconstruction

This appendix describes how to reconstruct in backward a 2D current distribution image from a magnetic field map with arbitrary direction components in Section 5.3.

### B.1 Magnetic field decomposition

The magnetic field of a component parallel to a dimensionless unit vector  $\hat{n}$  is described as follows

$$B_{\text{NV}} = n_x B_x + n_y B_y + n_z B_z \quad (\text{B.1})$$

, where  $\hat{n} = (n_x, n_y, n_z)$  is unit vector parallel to NV axis, and  $B_{\text{NV}}$  is magnetic field along NV axis, and  $\vec{B} = (B_x, B_y, B_z)$  is magnetic field. The beginning of this explanation is the Maxwell equation. The Maxwell equations are as follow

$$\nabla \cdot \vec{D} = \rho_{\text{free}}, \quad \nabla \cdot \vec{B} = 0, \quad \nabla \times \vec{E} = -\frac{\partial \vec{B}}{\partial t}, \quad \nabla \times \vec{H} = \vec{j}_{\text{free}} + \frac{\partial \vec{D}}{\partial t} \quad (\text{B.2})$$

## Appendix B. Magnetic Field Decomposition and Current Reconstruction

, in matter, and

$$\nabla \cdot \vec{E} = \frac{\rho}{\epsilon_0}, \quad \nabla \cdot \vec{B} = 0, \quad \nabla \times \vec{E} = -\frac{\partial \vec{B}}{\partial t}, \quad \nabla \times \vec{B} = \mu_0 \left( \vec{j} + \epsilon_0 \frac{\partial \vec{E}}{\partial t} \right) \quad (\text{B.3})$$

, in vacuum, where  $\vec{E}$  is electric field,  $\vec{D}$  is electric displacement field,  $\vec{B}$  is magnetic field,  $\vec{H}$  is magnetic field strength,  $\rho$  is electric charge density,  $\vec{j}$  is current density,  $\epsilon_0$  is vacuum permittivity, and  $\mu_0$  is vacuum permeability. Since the source-free region above the sample surface is considered, the expressions for magnetic field  $\vec{B}$  are

$$\nabla \cdot \vec{B} = 0, \quad \nabla \times \vec{B} = 0. \quad (\text{B.4})$$

These relations are transformed in Fourier space. The differential operators follow

$$\frac{\partial}{\partial x} \rightarrow ik_x, \quad \frac{\partial}{\partial y} \rightarrow ik_y, \quad \frac{\partial}{\partial z} \rightarrow -k \quad (\text{B.5})$$

, where  $k_x, k_y$  are Fourier space momentum vectors, and  $k$  is defined by  $k = \sqrt{k_x^2 + k_y^2}$ . The differentiation of  $x$  and  $y$  can be derived by using the definition of the Fourier transform. If the source is known, the  $z$  differentiation can be derived, and it is discussed later when the Green's function is introduced. Using these Equations B.1, B.4, and B.5, the system of equations for  $\vec{B}$  is derived as follows

$$\begin{aligned} B_{\text{NV}} &= n_x B_x + n_y B_y + n_z B_z \longrightarrow \tilde{B}_{\text{NV}} = n_x \tilde{B}_x + n_y \tilde{B}_y + n_z \tilde{B}_z, \\ \nabla \cdot \vec{B} &= \frac{\partial B_x}{\partial x} + \frac{\partial B_y}{\partial y} + \frac{\partial B_z}{\partial z} = 0 \longrightarrow ik_x \tilde{B}_x + ik_y \tilde{B}_y - k \tilde{B}_z = 0, \\ \left( \nabla \times \vec{B} \right)_z &= \frac{\partial B_x}{\partial y} - \frac{\partial B_y}{\partial x} = 0 \longrightarrow ik_y \tilde{B}_x - ik_x \tilde{B}_y = 0 \end{aligned} \quad (\text{B.6})$$

, where  $\tilde{\mathbf{B}}$  are magnetic fields defined in Fourier space. These system of equations are rewritten as

$$\begin{aligned}\tilde{B}_x &= \frac{ik_x}{in_x k_x + in_y k_y - n_z k} \tilde{\mathbf{B}}_{\text{NV}}, \\ \tilde{B}_y &= \frac{ik_y}{in_x k_x + in_y k_y - n_z k} \tilde{\mathbf{B}}_{\text{NV}}, \\ \tilde{B}_z &= \frac{-k}{in_x k_x + in_y k_y - n_z k} \tilde{\mathbf{B}}_{\text{NV}}.\end{aligned}\tag{B.7}$$

By imaging a magnetic field map in one direction parallel to the NV center and utilizing boundary conditions and source conditions, magnetic field maps in all component can be calculated.

## B.2 Current reconstruction

Biot-Savart law of 2D current density is defined by

$$\vec{\mathbf{B}}(\vec{r}) = \frac{\mu_0}{4\pi} \iint \frac{\vec{\mathbf{J}}(\vec{r}') \times (\vec{r} - \vec{r}')}{|\vec{r} - \vec{r}'|^3} dx dy.\tag{B.8}$$

In Fourier space, the relationship between the current density at height 0 and the magnetic field at height  $z$  is calculated. For Fourier space, this Biot-Savart law can be rewritten as

$$\vec{\mathbf{B}}(k_x, k_y, z) = \mathbf{g}(k_x, k_y, z) \vec{\mathbf{J}}(k_x, k_y, 0)\tag{B.9}$$

, where  $\mathbf{g}(k_x, k_y, z)$  is Green's functions of Biot-Savart law in Equation B.8. This Green's function is calculated with

$$\mathbf{g}(k_x, k_y, z) = \frac{\mu_0}{2} e^{-kz} \begin{pmatrix} 0 & 1 \\ -1 & 0 \\ ik_y/k & -ik_x/k \end{pmatrix}.\tag{B.10}$$

## Appendix B. Magnetic Field Decomposition and Current Reconstruction

The differentiation  $z$  in Equation B.5 is derived using this. Finally, the relationship between current and magnetic field is determined by

$$\begin{pmatrix} \tilde{B}_x \\ \tilde{B}_y \\ \tilde{B}_z \end{pmatrix} = \frac{\mu_0}{2} e^{-kz} \begin{pmatrix} 0 & 1 \\ -1 & 0 \\ ik_y/k & -ik_x/k \end{pmatrix} \begin{pmatrix} \tilde{J}_x \\ \tilde{J}_y \end{pmatrix}. \quad (\text{B.11})$$

By combining these equations,  $\vec{J}(x, y) = (J_x, J_y)$  can be calculated from the NV direction magnetic field  $B_{\text{NV}}$  map by

$$\begin{aligned} \tilde{J}_x &= \frac{1}{2} \left( 1 + \cos\left(\frac{k\lambda}{2}\right) \right) \frac{-1}{\frac{\mu_0}{2} e^{-kz}} \frac{ik_y}{in_x k_x + in_y k_y - n_z k} \tilde{B}_{\text{NV}}, \\ \tilde{J}_y &= \frac{1}{2} \underbrace{\left( 1 + \cos\left(\frac{k\lambda}{2}\right) \right)}_{\text{Hanning window}} \frac{1}{\frac{\mu_0}{2} e^{-kz}} \frac{ik_x}{in_x k_x + in_y k_y - n_z k} \tilde{B}_{\text{NV}}. \end{aligned} \quad (\text{B.12})$$

In practice, this relationship is multiplied by a Hanning window to filter out noise.

# Index

$T_1$ , 33

$T_2$ , 31

$T_2^*$ , 30, 79

Bloch

    sphere, 24

    vector, 24

Current reconstruction, 91

Diamond lattice, 7

Dual frequency ESR, 63, 101

FM Lock-in ESR, 64, 87

Hanning window, 91, 136

Hyperfine interaction, 27

Intersystem crossing, 12

Ion implantation, 74

IQ modulation, 24, 48

Landau-Lifshitz-Gilbert, 99

Mulliken notation, 10

Nanowires, 74

NV<sup>+,0,-</sup> center, 9

OOMMF, 75

Optical dipoles, 7

Partition function, 33

Point-contacted graphene, 84

Rabi oscillation, 23, 103

Ramsey measurement, 26, 79

Zeeman energy, 20

Zero field split, 12



Zero phonon line, 10

This page intentionally left blank.

# Curriculum Vitae

Myeongwon Lee

## Education

- Mar. 2017 Ph.D. in Department of Physics, Korea University, Seoul
- Aug. 2023 Advisor: Prof. Donghun Lee  
- Dissertation: *Quantum sensing and nanoscale imaging using scanning magnetometry with Nitrogen-Vacancy centers in diamond*
- Mar. 2011 B.S. in Department of Physics, Korea University, Seoul
- Feb. 2017 (Great Honor)

## Publications

1. Myeongwon Lee, Yuhan Lee, Taekhyeon Lee, Alec Jenkins, Min-Wook Han, Soogil Lee, Ha-Reem Kim, Hong-Gyu Park, Byong-Guk Park, Ania C. Bleszynski Jayich, Kab-Jin Kim, and Donghun Lee, “Imaging static field and driven microwave of Permalloy domain using single spin magnetometer” (*in preparation*)
2. Yuhan Lee\*, Myeongwon Lee\*, Junhyeon Jo, Seokmin Lee, Jungwoo Yoo, Andreas Heinrich, Taeyoung Choi, and Donghun Lee, “Imaging Oersted field around current flowing wire based on diamond scanning magnetometer,” *Current Applied Physics* **34** 59 (2022)
3. Lan-Anh T. Nguyen\*, Krishna P. Dhakal\*, Yuhan Lee\*, Wonseon Choi, Tuan Dung Nguyen, Chengyun Hong, Dinh Hoa Luong, Young-Min Kim, Jeongyong Kim, Myeongwon Lee, Taeyoung Choi, Andreas J. Heinrich, Donghun Lee, Dinh Loc Duong, and Young Hee Lee, “Probing room-temperature spin-polarized bands via circular-polarized photoluminescence in V-doped WSe<sub>2</sub> monolayer,” *ACS Nano* **15** 12 20267 (2021)

4. Myeongwon Lee, Seong Jang, Woochan Jung, Yuhan Lee, Takashi Taniguchi, Kenji Watanabe, Ha-Reem Kim, Hong-Gyu Park, Gil-Ho Lee, and Donghun Lee, “Mapping current profiles of point-contacted graphene devices using single-spin scanning magnetometer,” *Applied Physics Letters* **118** 033101 (2021).
5. Myeongwon Lee, Bumjin Jang, Jungbae Yoon, Mohan C. Mathpal, Yuhan Lee, Chulki Kim, Salvador Pane, Bradley J. Nelson and Donghun Lee, “Magnetic imaging of a single ferromagnetic nanowire using diamond atomic sensors,” *Nanotechnology* **29** 405502 (2018).
6. Sunuk Choe, Jungbae Yoon, Myeongwon Lee, Jooeon Oh, Dongkwon Lee, Heeseong Kang, Chul-Ho Lee, and Donghun Lee, “Precise temperature sensing with nanoscale thermal sensors based on diamond NV centers,” *Current Applied Physics* **18** 1066 (2018).

\* Equal contribution

## Book Chapters

1. Myeongwon Lee, Jungbae Yoon, and Donghun Lee. “Atomic Scale Magnetic Sensing and Imaging Based on Diamond NV Centers,” (*Magnetometers - Fundamentals and Applications of Magnetism*, 2019, ISBN: 9781839690969)

## Honor and Awards

- Grand prize, IonQ & QCenter,<sup>i</sup> **Quantum Challenge** (2021)
- Outstanding Teaching Assistant in Department of Physics, Korea University (2019)
- Great Honors in B.S., Korea University (2017)

---

<sup>i</sup> QCenter (양자정보연구지원센터): Quantum Information Research Support Center, South Korea

## Scholarship

- Research Encouragement Scholarship in Graduate School (2020, 2021)
- Baekwoon Scholarship in Department of Physics (2019)
- General Scholarships in Graduate School (2017 - 2018)
- Brain Korea 21 Plus Scholarship during Ph.D. (2017 - 2019)
- National Science and Engineering Scholarship during B.S. (2011, 2014 - 2016)

## Experience

- 제3회 대학원생을 위한 <연구역량 강화 워크숍> 발표, 고려대 교양교육원 (2022)  
“대학원생이 활용할 수 있는 자원은 무엇일까?”
- 양자정보경진대회, QCenter, Team: KoKoPos (2022)  
“Error mitigation for reliable quantum computation,” Mentor: Yosep Kim
- Quantum Challenge, IonQ & QCenter, Team: Kim&Lee (2021)
- Teaching Assistant, Korea University (2017 - 2019)  
General physics, and laboratory, Modern physics and experiments, Solid state physics
- Creative Challenger Program, 고려대 교수학습개발원, Team: 교학상장 (2016)  
“Teaching *Mathematica*<sup>®</sup> Quantum Mechanics,”<sup>ii</sup> Advisor: Prof. Mahn-Soo Choi
- Military Service, Honorable discharge from Army as Sergeant (Mar. 2012 - Dec. 2013)

---

<sup>ii</sup> Studying project for early stage of ‘M.-S. Choi, *A Quantum Computation Workbook*, 1st ed. (Springer, 2022)’

## Presentation

- Oral talk, APS March Meeting, “Imaging spin dynamics in ferromagnets using a single spin scanning magnetometer” (Mar. 2022)
- Oral talk, 양자정보과학겨울학교, “IonQ & QCenter Quantum Challenge” (Jan. 2022)
- Oral talk, The 2nd International Workshop on Scanning Probe Microscopy, “Mapping current profiles of point-contacted graphene devices using scanning diamond nitrogen-vacancy center magnetometer” (Aug. 2021)
- Oral talk, 양자센서겨울학교 & 워크샵, “Quantum sensing and nanoscale imaging with defects in solid-state” (Feb. 2021)
- Poster, Virtual Workshop on Scanning Probe Microscopy, “Current imaging of graphene point contacts using single spin magnetometer” (June 2020)
- Poster, IBS Conference on Quantum Nanoscience, “Quantum sensing and nano-scale imaging based on diamond NV centers with atomic force microscope” (Sept. 2019)
- Poster, Gordon Research Conference on Quantum Sensing, “Construction of novel scanning probe magnetometer based on NV Center in diamond” (June 2019)
- Oral talk, KPS Spring Meeting, “Nano-scale stray field imaging of magnetic structure with a single spin magnetometer” (Apr. 2019)
- Poster, International School on Spintronics and Korea-Japan Spintronics Workshop: Topological Phenomena in Magnetism, “Construction of novel scanning probe magnetometer based on diamond NV centers” (Jan. 2019)
- Poster, Symposium on Quantum and Nano Device, “Magnetometer based on NV centers in diamond” (Nov. 2018)
- Oral talk, KPS Fall Meeting, “Construction of novel scanning magnetometer based on NV centers” (Oct. 2018)
- Poster, Spin-based quantum information processing (Spin Qubit 4), “Construction of novel scanning probe magnetometer based on diamond NV center” (Sept. 2018)
- Oral talk, The 5th International Conference of Asian Union of Magnetism Societies, “Novel scanning magnetometry based on quantum defects in diamond” (June 2018)
- Poster, KPS Spring Meeting, “Nanoscale magnetic imaging based on diamond NV centers” (Apr. 2018)
- Poster, The 9th BK21+ Young Physicists Workshop, “Quantum magnetic sensing and imaging based on diamond NV centers” (Feb. 2017)

Figure 3.5, 3.9, 3.13, and 3.18 appear as animated images supported in Acrobat reader in Windows environment.

